Colloidal liquid crystals:

phase behavior, sedimentation, and percolation of rods, boomerangs, and cuboids

ISBN: 978-90-393-7021-6

A catalogue record is available from the Utrecht University Library.

Art design: Sander Kloppenburg

Colloidal liquid crystals:

phase behavior, sedimentation, and percolation of rods, boomerangs, and cuboids

Colloïdale vloeibare kristallen: fasegedrag, sedimentatie en percolatie van staven, boemerangs en balken

(met een samenvatting in het Nederlands)

Proefschrift

ter verkrijging van de graad van doctor aan de Universiteit Utrecht op gezag van de rector magnificus, prof. dr. H.R.B.M. Kummeling, ingevolge het besluit van het college voor promoties in het openbaar te verdedigen op maandag 10 september 2018 des middags te 12.45 uur

door

Tara Marie Drwenski

geboren op 6 maart 1990
te Rockwall, Texas, Verenigde Staten van Amerika

Promotor: Prof. Dr. R. H. H. G. van Roij

This research was supported by an NWO-VICI grant.

Contents

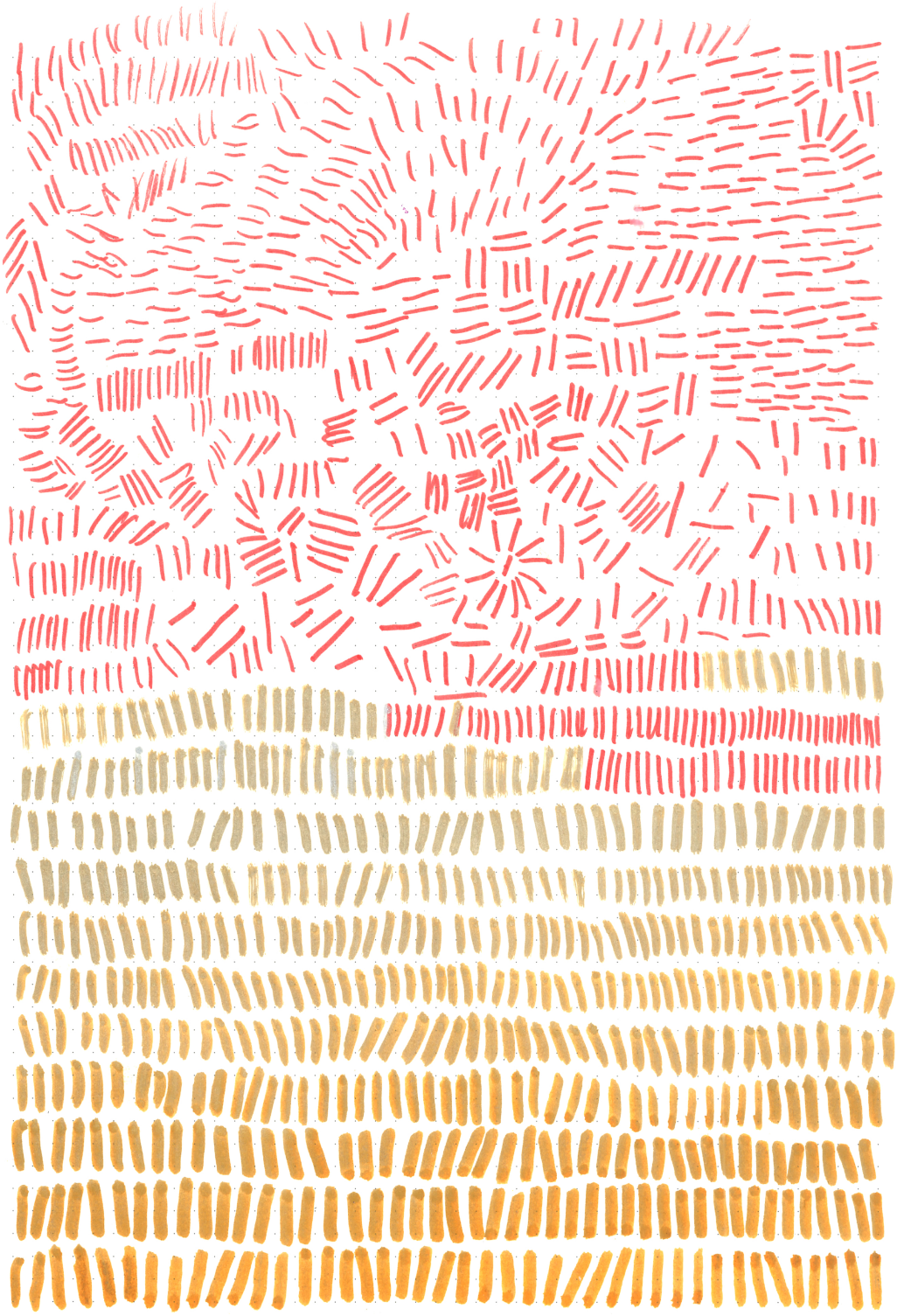

Chapter 1.

Introduction

1.1. Liquid crystal phases

Roughly spherical molecules (e.g. H_2O) commonly form three types of phases, namely gas, liquid, and crystal phases, distinguished by the degree of ordering of their positions. While the dilute gas and denser liquid phase are homogeneous in space, the crystal phase has periodic order on a three-dimensional lattice. Less symmetric molecules can form additional phases that have more spatial or orientational order than the liquid, but are not completely ordered in three dimensions like the crystal phase. These are known as *liquid crystal phases*, some examples of which are shown in Fig. 1.1 for rodlike molecules. The simplest of these, the *nematic* phase has long-range orientational order but no positional order. In addition to orientational order, *smectic* phases have positional order in one direction but are liquid-like in the other two. On the other hand, so-called *plastic crystal* phases have long-ranged positional order, but no orientational order. Besides the nematic, smectic, and plastic crystal, many other types of liquid phases can be formed depending on the symmetries and properties of the individual constituents [1].

Colloidal particles (or colloids) are roughly defined as solute particles with dimensions in the range from several nanometers to a micrometer, such that they experience Brownian motion due to collisions with the solvent particles (molecules) at room temperature. This is important as this means that colloidal particles explore their phase space, and so the concepts of statistical physics apply to them. For the purposes of this thesis, the colloidal particles are treated as classical objects. Due to the large length and time scale differences between solvent particles and the colloidal particles, a full description of a colloidal suspension is difficult. The problem is typically simplified by integrating out the degrees of freedom of the solvent, and so only considering colloid-colloid effective interactions.

Colloids in a solvent can form liquid crystal phases, analogously to the molecular systems and so Fig. 1.1 also describes the phases of suspensions of rodlike colloids such as tobacco mosaic viruses, fd viruses [2], or silica rods [3]. In fact, colloidal particles can be seen as a model system for atomic or molecular systems since they form similar phases, but are large enough to see under an optical microscope. Furthermore, colloids can be synthesized in many shapes and with many tunable interactions, and so are an ideal fundamental tool for studying phase transitions.

The phase transitions of molecular systems are mostly driven by attractive interactions, and so the sequence shown in Fig. 1.1 could describe the phases of elongated molecules from high temperatures (left) to low temperatures (right). On the other hand, short range repulsive interactions ("hard" interactions) of colloids in a suspension are sufficient to cause the formation of the phases in Fig. 1.1, where the number density is the driver of the transitions, from low density (left) to high density (right).[1] These hard interactions are the result of the particles not being able to overlap, and so they are dependent on particle shape.

The fact that shape and so entropy alone drives the isotropic-nematic transition in rodlike colloids was shown by Onsager in 1949 [5], who explained this transition with a simple theory that only includes two-particle correlations. While the orientational entropy is maximized in the isotropic fluid phase, the particles gain free volume by aligning along a so-called nematic director in the nematic phase. More recently, computer simulations have shown that other liquid crystal phases such as the smectic can be formed by systems with only hard interactions. Onsager's theory, which is the basis for this thesis, is introduced in the following section, within the more general framework of density functional theory.

1.2. Density functional theory

We consider a suspension (in the absence of external fields) of N colloidal particles with total volume V at temperature T. In density functional theory (DFT), we express the free energy F as a functional of the single-particle density $\rho(\mathbf{r}, \Omega)$, where the particle position is given by $\mathbf{r}$. The orientation of a rigid, biaxial particle can be given by three Euler angles $\Omega = (\alpha, \beta, \gamma)$ (see also Appendix A). The single-particle density must be normalized according

[1] For hard colloidal rods this phase sequence is seen for rods with a length-to-diameter ratio of approximately five or higher [4].

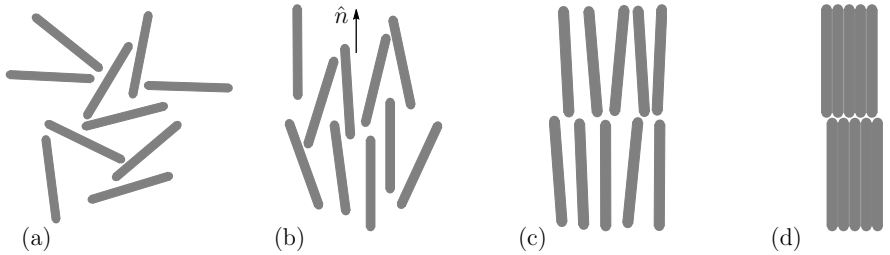

Figure 1.1.: Schematic illustration of the liquid crystal phases of (sufficiently long) rodlike colloids, from least ordered to most ordered: (a) isotropic (liquid), (b) nematic with nematic director $\hat{n}$, (c) smectic, and (d) crystal.

to

$$\int d\mathbf{r} \int d\Omega \, \rho(\mathbf{r}, \Omega) = N. \tag{1.1}$$

We can introduce a Lagrange multiplier μ to account for the normalization of $\rho(\mathbf{r}, \Omega)$, i.e., we can write a new functional $F[\rho] - \mu N$.

It can be shown that there exists a functional $F[\rho] - \mu N$ that is minimized by the equilibrium single-particle distribution ρ_{eq} and in addition the equilibrium value of the free energy is given by $F[\rho_{\text{eq}}]$ [6]. This implies that given that we know the appropriate form of the functional $F[\rho]$, the full equilibrium thermodynamics can be determined through a variational principle.

It is convenient to write the free energy as the sum of an ideal and an excess part, i.e.,

$$F\left[\rho\right] = F_{\text{id}}\left[\rho\right] + F_{\text{ex}}\left[\rho\right], \tag{1.2}$$

where the ideal contribution is

$$\beta F_{\text{id}}\left[\rho\right] = \int d\mathbf{r} \int d\Omega \, \rho(\mathbf{r}, \Omega) \left\{ \ln\left[\mathcal{V}\rho(\mathbf{r}, \Omega)\right] - 1 \right\}, \tag{1.3}$$

where $\beta = 1/(k_B T)$ is the inverse thermal energy with k_B being Boltzmann's constant, $\mathcal{V}$ is an irrelevant thermal volume factor, and the integration measure is $\int d\Omega = \int_0^{2\pi} d\alpha \int_0^{\pi} \sin\beta d\beta \int_0^{2\pi} d\gamma = 8\pi^2$. In general, we have to make some approximation for the excess part $F_{\text{ex}}\left[\rho\right]$ which is zero for non-

interacting systems. Formally at least, we can write this exactly in terms of the virial series as

$$\beta F_{\text{ex}}[\rho] = -\frac{1}{2}\int d\mathbf{r_1}\int d\mathbf{r_2}\int d\Omega_1\int d\Omega_2\, f(\mathbf{r}_1,\Omega_1;\mathbf{r}_2,\Omega_2)\rho(\mathbf{r_1},\Omega_1)\rho(\mathbf{r_2},\Omega_2) + \mathcal{O}(\rho^3), \tag{1.4}$$

where $f(\mathbf{r}_1,\Omega_1;\mathbf{r}_2,\Omega_2)$ is the Mayer function, given by

$$f(\mathbf{r}_1,\Omega_1;\mathbf{r}_2,\Omega_2) = e^{-\beta U(\mathbf{r}_1,\Omega_1;\mathbf{r}_2,\Omega_2)} - 1, \tag{1.5}$$

where $U(\mathbf{r}_1,\Omega_1;\mathbf{r}_2,\Omega_2)$ is the pair potential. For all systems studied in this thesis, we assume global translational and global rotational invariance, i.e., the pair potential (and so the Mayer function) only depends on $\mathbf{r}_{12} = \mathbf{r}_2 - \mathbf{r}_1$ the vector connecting the centers of the two particles and the relative orientation between two particles Ω_{12}.

In order to find the equilibrium ρ_{eq} and thus the equilibrium $F[\rho_{\text{eq}}]$, we minimize $F[\rho] - \mu N$ with respect to ρ. This yields the following Euler-Lagrange equation

$$\left.\frac{\delta F[\rho]}{\delta\rho(\mathbf{r}_1,\Omega_1)}\right|_{\rho=\rho_{\text{eq}}} = \mu. \tag{1.6}$$

For the second-virial approximation [ignoring terms of $\mathcal{O}(\rho^3)$ and higher in Eq. (1.4)], this gives the so-called self-consistent equation

$$\rho(\mathbf{r}_1,\Omega_1) = \frac{1}{Z}\exp\left[\int d\mathbf{r_2}\int d\Omega_2\, f(\mathbf{r}_{12},\Omega_{12})\rho(\mathbf{r_2},\Omega_2)\right], \tag{1.7}$$

where we drop the subscript "eq" for convenience and where

$$Z = \int d\mathbf{r_1}\int d\Omega_1 \exp\left[\int d\mathbf{r_2}\int d\Omega_2\, f(\mathbf{r}_{12},\Omega_{12})\rho(\mathbf{r_2},\Omega_2)\right], \tag{1.8}$$

explicitly takes care of the normalization of ρ.

Homogeneous phases

We now assume that the single-particle density has no spatial dependence as is the case for the isotropic and nematic liquid crystals phases, i.e., we assume $\rho(\mathbf{r},\Omega) = \rho\psi(\Omega)$, where $\rho = N/V$ is the average density. The

orientation distribution function $\psi(\Omega)$ is defined so that the probability to find a particle with an orientation in the interval $d\Omega$ is given by $\psi(\Omega)d\Omega$, with the normalization constraint that

$$\int d\Omega\, \psi(\Omega) = 1. \tag{1.9}$$

The free energy density can be written as

$$\begin{aligned}\frac{\beta F\left[\psi(\Omega)\right]}{V} &= \rho(\ln \mathcal{V}\rho - 1) + \rho \int d\Omega\, \psi(\Omega) \ln \psi(\Omega) \\ &\quad + \rho^2 B_2 + \frac{\rho^3}{2} B_3 + \ldots,\end{aligned} \tag{1.10}$$

where the first line is the ideal part and the second line the excess part in the virial expansion, with B_n the nth virial coefficient. In the second-virial approximation, we truncate the excess free energy at B_2 and similarly in the third-virial theory we truncate at B_3. The second-virial term is

$$B_2 = \frac{1}{2} \int d\Omega_1 \int d\Omega_2 E(\Omega_{12}) \psi(\Omega_1) \psi(\Omega_2), \tag{1.11}$$

where Ω_{12} is the relative orientation between two particles with orientations Ω_1 and Ω_2. The spatial integral over the Mayer function in Eq. (1.11), $E(\Omega)$, is defined as

$$E(\Omega_{12}) = -\int d\mathbf{r}_{12}\, f(\mathbf{r}_{12}, \Omega_{12}), \tag{1.12}$$

where $f(\mathbf{r}_{12}, \Omega_{12})$ is the Mayer function [Eq.(1.5)].

The third-virial term is

$$B_3 = \frac{1}{3} \int d\Omega_1 \int d\Omega_2 \int d\Omega_3 \hat{E}(\Omega_{12}, \Omega_{13}) \psi(\Omega_1) \psi(\Omega_2) \psi(\Omega_3), \tag{1.13}$$

with

$$\begin{aligned}\hat{E}(\Omega_{12}, \Omega_{13}) = -\int d\mathbf{r}_{12} \int d\mathbf{r}_{13} \big[& f(\mathbf{r}_{12}, \Omega_{12}) f(\mathbf{r}_{13}, \Omega_{13}) \\ & \times f(\mathbf{r}_{13} - \mathbf{r}_{12}, \Omega_{12}^{-1} \Omega_{13}) \big].\end{aligned} \tag{1.14}$$

Excluded volume

In this thesis, we mostly study *hard* particles, meaning particles with the pair potential

$$\beta U(\mathbf{r}_{12}, \Omega_{12}) = \begin{cases} \infty, & 1 \text{ and } 2 \text{ overlap;} \\ 0, & \text{otherwise.} \end{cases} \tag{1.15}$$

In this case, the Mayer function is

$$f(\mathbf{r}_{12}, \Omega_{12}) = \begin{cases} -1, & 1 \text{ and } 2 \text{ overlap;} \\ 0, & \text{otherwise,} \end{cases} \tag{1.16}$$

and $E(\Omega_{12})$ [Eq. 1.12] is known as the *excluded volume*, since it gives the volume one particle with orientation Ω_1 excludes to a second particle with orientation Ω_2.

Hard spherocylinders, i.e., cylinders capped at both ends by a hemisphere, only need a unit vector $\hat{\omega}$ (or two angles) to specify their orientations (see Appendix A), so their relative orientation is given by the $\beta_{12} = \arccos(\hat{\omega}_1 \cdot \hat{\omega}_2)$. Onsager showed that the excluded volume for spherocylinders of length L and diameter D is [5]

$$E(\beta_{12}) = 2L^2 D |\sin \beta_{12}| + 2\pi L D^2 + \frac{4}{3}\pi D^3, \tag{1.17}$$

as shown in Fig. 1.2. Onsager's second-virial theory for hard spherocylinders describes the isotropic-nematic transition as due to a competition between orientational entropy [integral term in Eq. (1.10)] which favors the isotropic phase, and the excluded volume [Eq. (1.17)], which is reduced for aligned particles (with small β_{12}) in the nematic phase. In the needle limit of $L/D \to \infty$ the second and third terms of Eq. (1.17) can be neglected and second-virial theory becomes exact [5, 7–10].

The excluded volume can be calculated analytically for convex particles that are centrally symmetric, known as zonotopes [11]. Some examples of zonotopes are parallelepipeds, rectangular solids, and hexagonal solids as well as the "sphero-zonotope" analogue of these, that is, the same bodies but padded by a certain radius. However, for many other shapes the excluded volume is not known analytically.

One simple method for evaluating the integral Eq. (1.12), which is especially useful for hard particles [with the Mayer function Eq. (1.16)] is *Monte*

Carlo integration. Given an algorithm for checking for two particle overlaps, one particle is fixed at the center of a box with a fixed orientation and a second one is thrown in with a random position within the box and a random orientation. For a certain number of Monte Carlo steps, new configurations are generated and the number of overlaps for each orientation is recorded. Finally, the fraction of times the particles overlapped for each orientation is multiplied by the integration volume to obtain the final result for the excluded volume as a function of orientation.

Calculating the orientation distribution function

To obtain the equilibrium orientation distribution function for a homogeneous phase, we minimize the free energy with respect to $\psi(\Omega)$, at a given ρ, with a normalization constraint [Eq. (1.9)]. This gives

$$\psi(\Omega_1) = \frac{1}{Z} \exp\left[-\rho \int d\Omega_2 E(\Omega_{12})\psi(\Omega_2)\right], \tag{1.18}$$

where $Z = \int d\Omega_1 \exp\left[-\rho \int d\Omega_2 E(\Omega_{12})\psi(\Omega_2)\right]$ ensures the normalization. Equation (1.18) is a nonlinear integral equation, often called a "self-consistent" equation as the unknown quantity $\psi(\Omega)$ is written in terms of itself. While one solution of Eq. (1.18) is known analytically, namely a constant $\psi(\Omega) = 1/(8\pi^2)$ corresponding to the isotropic distribution, other solutions have to be determined numerically.

In Chapters 2, 3 and 6, we solve for the equilibrium orientation distribution function numerically on an angular grid. There we use the uniaxiality of the rods (or in the case of Chapter 3 the uniaxiality of the segments) to write the single particle orientation in terms of a unit vector $\hat{\omega}$ or equivalently, two angles, θ, ϕ. However, describing the orientation of an arbitrarily shaped (rigid) particle requires three Euler angles. In this case, the equilibrium orientation distribution function $\psi(\Omega)$ could also in principle be computed on a grid of three angles.

Another method is to expand both the excluded volume $E(\Omega_{12})$ and the orientation distribution function $\psi(\Omega)$ in complete bases and to solve for the expansion coefficients of $\psi(\Omega)$. This method has the advantage of being amenable to simplification using the symmetries of the particle and phase. We use this expansion method in Chapters 4-5.

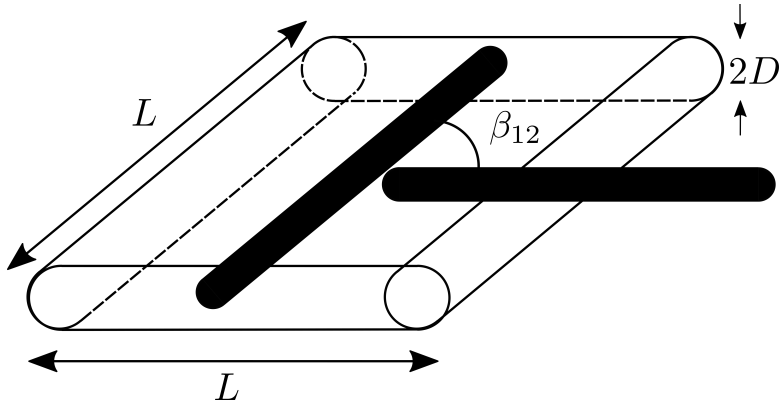

Figure 1.2.: Illustration of the excluded volume of two spherocylinders of length L, diameter D, and relative orientation β_{12}. The center of the right spherocylinder cannot enter the outlined region without overlapping with the left spherocylinder.

Bifurcation analysis

One tool for studying solutions to the self-consistent equation [Eq. (1.7) or Eq. (1.18)] is a so-called bifurcation analysis [12], introduced in the context of liquid crystals by Kayser and Raveché [13] and extended by Mulder [14]. Liquid crystal phase transitions often are *symmetry breaking* transitions. Close to such a transition, there are two solutions to the Euler-Lagrange equation [Eq. (1.7)]. As some parameter (here the number density) is changed, the second "new" solution branches from the original solution, either in such a way that it is immediately the global minimum of the free energy or else initially metastable (a local but not a global minimum of the free energy). The bifurcation analysis simply requires a known stable solution. Then, we expand in density and we expand around the known solutions to look for the new, less symmetric solutions.

As discussed above, the isotropic solution is one solution to Eq. (1.18). The solution of the Euler-Lagrange equation is an extremum of the free energy, and not necessarily a minimum. The bifurcation analysis performed in Ref. [13] shows the bifurcating density is an upper limit to the stability of the isotropic solution, and the branching solution corresponds to the less symmetric nematic phase. The bifurcation analysis can also be applied to the nematic-smectic transition for rods [14–16] or other particle shapes like we do in Chapter 4.

1.3. Sedimentation

Just as diffuse (ideal) gases in a gravitational field have a barometric law, dilute suspensions of colloids have an exponential density profile as a function of height of the test tube. That is, the density profile of the colloids is $\rho(z) = \rho(0)\exp(-z/l)$, where z is the height with $z = 0$ the bottom of the test tube and $l = k_BT/mg$ is the so-called gravitational length, with m the buoyant mass of a colloid and g the acceleration due to gravity. This so-called sedimentation-diffusion equilibrium is a consequence of the competition between entropy, which favors a homogeneous distribution of the colloids, and gravitational energy, which favors a high density at the bottom of the test tube.

Historically, Perrin used colloids with a known buoyant mass to determine Boltzmann's constant k_B from the barometric profile [17]. Measuring the gravitational length of a colloidal suspension at a known temperature can also be used to determine the buoyant masses of the colloids. Furthermore, a single sedimentation density profile of a one-component system can be used to determine the full equation of state, and so is useful for gaining information about thermodynamic properties [18–21].

In Chapter 6, we study the sedimentation density and composition profiles of a two-component system of thick and thin rods. This is done using a method which relates the bulk phase behavior in the absence of gravity to the sedimentation "stacking sequences" of phases that can occur in a test tube.

1.4. Percolation

Percolation was originally a term referring to fluid flow through a porous material. This can be modeled as a lattice where each bond between lattice sites (channel) has a probability p to be "open." The system is percolating if a system-spanning open path exists (fluid can flow through the material). The non-percolating ($p < p_c$) to percolating ($p > p_c$) phase transition occurs at a critical probability p_c.

Continuum percolation theory is the extension of the discrete lattice percolation theory to real space. The "sites" are now particles distributed in three-dimensional space, and two particles are defined as connected if they have a surface-to-surface distance less than some cutoff Δ. Particles that are connected are considered to be part of the same cluster. The system

percolates above a critical density of particles known as the percolation threshold, when there is a system-spanning cluster of particles.

Continuum percolation theory can be used to model nanocomposite materials composed of, for example, carbon nanotubes dispersed in plastics. Given that two nanotubes are close enough (surface-to-surface distance less than some Δ), the electrons can hop or tunnel between them, and so clusters of connected nanotubes are conducting. Above the critical density of particles, there is a system-spanning conductive network and so the composite material can conduct.

In Chapters 7 and 8, we use continuum percolation theory in the second-virial approximation to determine how particle shape affects the percolation threshold for hard particles in the isotropic phase.

1.5. Outline of this thesis

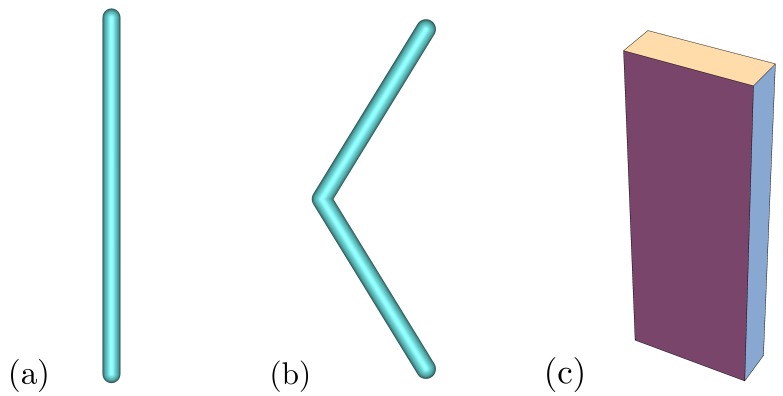

Figure 1.3.: Illustration of three of the colloidal particle shapes studied in this thesis: (a) rod (or spherocylinder), (b) boomerang, and (c) cuboid.

The rest of the thesis proceeds as follows. In Chapter 2, we study weakly and strongly charged rodlike colloids using second-virial theory. Additionally, we investigate the stability of the nematic phase with respect to twist deformations, in order to see if charge can spontaneously break chiral symmetry. We then shift our focus to hard particles of various shapes less symmetric than spherocylinders. In Chapter 3, we study flexible "boomerangs," i.e., two spherocylinders joined at one end that can fluctuate around a certain preferred interarm angle. Here our focus is on biaxial nematic phases and how

flexibility affects their stability. In Chapter 4, we investigate the homogeneous phases of rigid boomerangs as well as their limit of stability with respect to smectic phases by performing a bifurcation analysis. In Chapter 5, we study the nematic phases of cuboids within second and third-virial theory, and compare our results to recent simulations. Then, in Chapter 6 we consider the sedimentation of a binary mixture of thick and thin rods, and build "stacking diagrams," which describe the sequences of phases that appear due to gravity. Finally, in Chapters 7 and 8, we study the percolation transitions of various shapes of colloidal particles in the isotropic phase. Specifically, in Chapter 7 we investigate the effect of kink and bend deformations on the percolation threshold of rodlike particles and in Chapter 8 we calculate the percolation thresholds of polygonal rods and platelets. Examples of three of the particle models studied in this thesis, namely rods, boomerangs, and cuboids, are shown in Fig. 1.3.

Chapter 2.

Charged rods

2.1. Introduction

The isotropic-nematic phase transition in dispersions of rigid, rodlike colloids occurs at sufficiently high concentration of rods. For uncharged rods, this phase transition is purely the result of a competition between orientational entropy, which is maximized in the isotropic phase, and the translational entropy, which favors the nematic phase, where rods tend to align along a nematic director $\hat{n}$. For long, rigid, needle-like rods, this phase transition is accurately described by Onsager's second-virial theory [5].

Many experimental systems do not form ordinary nematic phases, but instead form a cholesteric (chiral nematic) phase, where the nematic director field has a helical arrangement with a pitch much larger than the colloidal dimensions. Though the cholesteric phase is ubiquitous in experimental systems, the relationship between particle properties and macroscopic chirality remains unclear [22, 23]. An illustrative example of this involves suspensions of filamentous fd virus, which are semi-flexible charged needles with a chiral structure that form a cholesteric phase in a density regime that depends on the ionic strength. In Ref. [23], however, fd-virus particles sterically stabilized by a coating with the neutral polymer polyethylene glycol (PEG) exhibited a phase diagram and a nematic order parameter independent of the ionic strength, but surprisingly, the fd-PEG continued to form a cholesteric phase with a pitch that did vary with the ionic strength.

Furthermore, molecular chirality does not guarantee macroscopic chirality. For example, the virus Pf1, with a chiral structure very similar to that of fd, does not form a cholesteric phase (or its pitch is too large to observe experimentally) [24]. Indeed, subtle alterations of the surface properties of fd that do not have a large effect on the phase diagram can have an appreciable effect on the cholesteric pitch [25]. Reversing the surface charge of fd from

negative to positive even prevented the observation of a cholesteric pitch, though the chemical modification of fd may have also introduced additional attractive forces [25]. The fact that the cholesteric pitch is very sensitive to particle surface properties was also shown in a study of M13, which is a charged, large-aspect ratio bacteriophage with a right-handed structure that is shown to form a left-handed macroscopic phase [26]. Though steric effects are shown to favor a right-handed phase, charges added along grooves of the coarse-grained representation of M13 caused the calculated pitch to become left-handed [26]. The microscopic origin of chirality in colloidal suspensions remains a mystery despite many interesting recent works [27–29], though charge seems to be one of the crucial ingredients [23, 25, 26, 30, 31].

A wide variety of experimental systems that display nematic or cholesteric phases involve electrostatic interactions [10], for example, filamentous viruses [2, 32, 33], actin filaments [34–36], cellulose derivatives [37, 38], and single-walled carbon nanotubes in superacids [39, 40]. For strong electrostatic interactions or short screening lengths, the isotropic-nematic phase transition is well understood. Onsager [5] was the first to note that the soft repulsion can be treated by renormalizing the diameter of the rods. Stroobants et al. [41] showed that there is a second effect for strong electrostatic interactions, namely a "twisting" due to the angular dependence of the electrostatic potential, which makes the rods resist aligning.

Weakly charged rods have also been studied extensively. In Refs. [42, 43], a scaling theory was used to give qualitative predictions for charged rods. Interestingly, in a certain region of low charge density and moderate screening they predict that a competition between steric and electrostatic effects leads to a coexistence between a nematic and a highly oriented nematic phase. Most predictions of Refs. [42, 43], including the existence of the nematic-nematic coexistence were confirmed in Ref. [44], using a Debye-Hückel-like theory that includes some many-rod correlations. Another interesting result is that the correlation electrostatic energy due to charge fluctuations in a many-body system of charged rods and counterions makes orientational order more favorable, stabilizes a weakly ordered nematic at small rod concentrations, and leads to the possibility of two nematic phases [45, 46].

The goal of this chapter is to quantitatively examine both weak and strong electrostatic interactions using second-virial theory and additionally to investigate how charge affects the stability of the nematic phase with respect to spontaneous twist deformations. In Sec. 2.2, we review second-virial theory for charged rods and extend previous results to weakly charged rods. We also determine for which parameters the twisting effect becomes important

for weakly charged rods. In Sec. 2.3, we construct the phase diagrams and identify the parameter regime where nematic-nematic coexistence can occur. We then briefly discuss the possibility of seeing the nematic-nematic coexistence experimentally in Sec. 2.4. In Sec. 2.5, we investigate if the twisting effect can stabilize a cholesteric phase. We do this by calculating the Frank elastic constants of the nematic phase and examining the relationship between the twisting effect and the twist elastic constant. We are especially interested whether the twist elastic constant (evaluated in the nematic state) can become negative, which would indicate the possibility of a cholesteric phase spontaneously forming. Finally, we examine the sign of the twist elastic constant for finite aspect-ratio rods in Sec. 2.6. We end with a summary and conclusions in Sec. 2.7.

2.2. Onsager theory

2.2.1. Second-virial term

We consider N charged colloidal rods of length L and diameter D suspended in an electrolytic solvent characterized by a salt concentration ρ_s and a dielectric permittivity ϵ. The system has a total volume V and a temperature T. The Bjerrum length is given by $\lambda_B = e^2/(4\pi\,\epsilon_0\,\epsilon\,k_BT)$, with e the elementary charge, k_B the Boltzmann constant, and ϵ_0 the vacuum permittivity, and the Debye screening length is defined as $\kappa^{-1} = 1/\sqrt{8\pi\lambda_B\rho_s}$ [47].

In addition to a hard-core repulsion between a pair of rods, there is also a screened electrostatic interaction, approximated by the interaction between two line charges with effective linear charge density $v_{\text{eff}} = Z/L$ with Z the number of elementary charges on a rod. The form of this electrostatic interaction for infinitely long cylinders in the Debye-Hückel approximation is well known [48–50]. The pair potential $U(x,\gamma)$ is given by

$$\beta U(x,\gamma) = \begin{cases} \infty, & x \le D \\ \dfrac{\mathcal{A}\,e^{-\kappa x}}{\kappa D|\sin\gamma|}, & x > D, \end{cases} \tag{2.1}$$

with $\beta = (k_BT)^{-1}$, x the minimum separation between the two rods, γ the angle between the uniaxial rods with orientations $\hat{\omega}$ and $\hat{\omega}'$ defined by $\cos\gamma = \hat{\omega}\cdot\hat{\omega}'$ (see Fig. 2.1), and where we have introduced the dimensionless

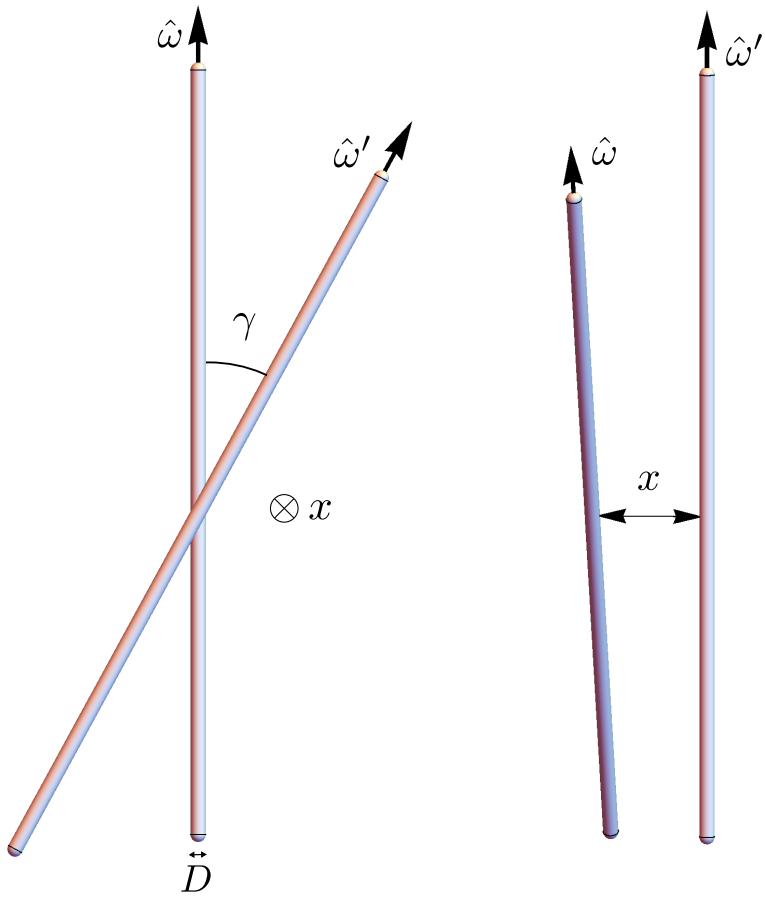

Figure 2.1.: Illustration of two charged spherocylinders with diameters D from two different viewpoints. The rods are oriented along unit vectors $\hat{\omega}$ and $\hat{\omega}'$, with $\gamma = \arccos(\hat{\omega} \cdot \hat{\omega}')$ the angle between the rods and x the shortest distance between them.

coupling parameter

$$\mathcal{A} = 2\pi\, v_{\text{eff}}^2\, \lambda_B\, D. \tag{2.2}$$

Eq. (2.1) is valid when $\kappa^{-1} \ll L$ and $x \ll L$.

Following Onsager [5], we study the phase behavior of this suspension of charged needles in terms of the single-rod orientation distribution function $\psi(\hat{\omega})$, which suffices for translationally invariant phases. The distribution $\psi(\hat{\omega})$ is normalized as

$$\int d\hat{\omega}\, \psi(\hat{\omega}) = 1. \tag{2.3}$$

Assuming $L \gg D$, we can write the Helmholtz free energy functional $F[\psi]$ of a suspension of rods in the second-virial approximation as

$$\begin{aligned}\frac{\beta F[\psi]}{V} &= \rho(\ln \mathcal{V}\rho - 1) + \rho \int d\hat{\omega}\, \psi(\hat{\omega}) \ln \psi(\hat{\omega}) \\ &\quad + \frac{1}{2}\rho^2 \int d\hat{\omega} \int d\hat{\omega}'\, E(\hat{\omega}, \hat{\omega}')\psi(\hat{\omega})\psi(\hat{\omega}') + \mathcal{O}(\rho^3),\end{aligned} \tag{2.4}$$

where $\rho = N/V$ is the number density and $\mathcal{V}$ is a thermal volume. In Eq. (2.4), the first term gives the translational entropy and the second gives the orientational entropy. The third term is the second-virial term, with the "excluded volume" term $E(\hat{\omega}, \hat{\omega}')$ defined as

$$\begin{aligned}E(\hat{\omega}_1, \hat{\omega}_2) &= -\frac{1}{V} \int d\mathbf{r}_1 \int d\mathbf{r}_2\, f(\mathbf{r}_1 - \mathbf{r}_2; \hat{\omega}_1, \hat{\omega}_2) \\ &= -\int d\mathbf{r}_{12}\, \left[e^{-\beta U(\mathbf{r}_{12}; \hat{\omega}_1, \hat{\omega}_2)} - 1\right],\end{aligned} \tag{2.5}$$

where we have used translational invariance, defined $\mathbf{r}_{12} = \mathbf{r}_1 - \mathbf{r}_2$, and introduced the Mayer function $f = e^{-\beta U} - 1$ which depends on $U(\mathbf{r}_{12}; \hat{\omega}_1, \hat{\omega}_2)$, the pair potential between a rod with orientation $\hat{\omega}_1$ and position $\mathbf{r}_1$ and a second rod with orientation $\hat{\omega}_2$ and position $\mathbf{r}_2$.

Now, performing the integration over the Mayer function in Eq. (2.5) with the potential given in Eq. (2.1) and using $d\mathbf{r}_{12} = L^2 |\sin\gamma|\, dx$, we can

write $E(\gamma) = E(\hat{\omega}, \hat{\omega}')$ as [48]

$$\begin{aligned} E(\gamma) = & -2L^2 \,|\sin\gamma| \int_0^\infty dx\, f(x,\gamma) \\ & = 2L^2 D \,|\sin\gamma| \left\{ 1 + \frac{1}{\kappa D} \left[\ln\left(\frac{A'}{|\sin\gamma|} \right) \right.\right. \\ & \left.\left. + \gamma_E - \mathrm{Ei}\left(-\frac{A'}{|\sin\gamma|} \right) \right] \right\}, \end{aligned} \tag{2.6}$$

where $\gamma_E \approx 0.5772$ is Euler's constant, the exponential integral Ei is defined as $\mathrm{Ei}(y) = -\int_{-y}^{\infty} \exp(-t)/t\, dt$, and $A' = \mathcal{A}\, e^{-\kappa D}/(\kappa D)$. The function $\mathrm{Ei}(-A')$ becomes negligible for $A' \gtrsim 2$, which is the approximation used in Ref. [41]. In the present work, we also consider $A' \lesssim 2$, and hence we keep the Ei term in Eq. (2.6) throughout.

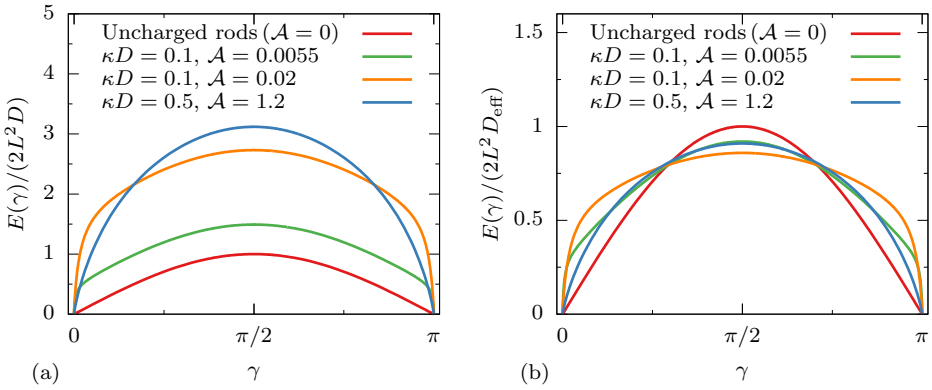

Figure 2.2.: Dependence of the "excluded volume" $E(\gamma)$ [Eq. (2.6)] on the angle γ between two rods [see Fig. 2.1] for uncharged rods ($\mathcal{A} = 0$) and charged rods for different values of screening parameter κD and Coulomb coupling $\mathcal{A}$. In (a), $E(\gamma)$ is scaled by the volume factor $2L^2D$. In (b), $E(\gamma)$ is scaled by effective volume factor $2L^2D_{\mathrm{eff}}$ [see Eq. (2.9)]. The value of twisting parameter H [Eq. (2.15)] is 0, 0.71, 1.1, and 0.54 for red, green, orange, and blue curves, respectively.

The function $E(\gamma)$ of Eq. (2.6) depends on the intrinsic excluded volume L^2D of the rods, the screening parameter κD, and the parameter A'. However, in order to be able to vary the charge density of the needles and the salt concentration independently, we prefer to use $\mathcal{A}$ rather than A' as an independent parameter, since $\mathcal{A}$ only depends on the charge of the rods (and the Bjerrum length) and not on κD. In Fig. 2.2(a), we plot $E(\gamma)$ as a function

of the angle γ between the rods for a few values of κD and $\mathcal{A}$, along with the hard-rod excluded volume for comparison. We observe essentially two effects compared to the hard-rod excluded volume, for which $E(\gamma)/(2L^2D)$ reduces to $|\sin\gamma|$. First, due to the charge there is an overall increase in the "excluded volume" for all parameters, and second, there is a change in the shape of $E(\gamma)$ from that of hard rods, in particular the γ-dependence is much stronger at small γ's, i.e., charged rods disfavor small angles much more than hard rods do. The former we describe by an increasing effective diameter D_{eff} and the latter we describe by a "twisting" parameter. These two effects will be discussed in Sec. 2.2.2 and Sec. 2.2.3, respectively.

The equilibrium orientation distribution function is obtained by minimizing $F[\psi]/V$ with respect to $\psi(\hat{\omega})$, at fixed ρ, T, κ^{-1}, and $\mathcal{A}$, which gives the integral equation [10]

$$\ln\psi(\hat{\omega}) + \rho\int d\hat{\omega}'\, E(\gamma(\hat{\omega},\hat{\omega}'))\psi(\hat{\omega}') = C, \tag{2.7}$$

with C a constant that ensures that the constraint of Eq. (2.3) is satisfied. There is an analytic solution to Eq. (2.7), namely $\psi_{\text{i}}(\hat{\omega}) = 1/(4\pi)$, describing the isotropic phase which is the only (stable) one at sufficiently low ρ [5, 13, 51].

At higher densities, $E(\gamma)$ becomes more important in Eq. (2.7) and the rods favor the nematic phase, where the orientation distribution function becomes peaked around a nematic director $\hat{n}$. We choose a coordinate system with the z-axis parallel to $\hat{n}$. The unit vector $\hat{\omega}$ can be written as $\hat{\omega} = (\sin\theta\,\cos\varphi, \sin\theta\,\sin\varphi, \cos\theta)$, where φ is the azimuthal angle and θ is the polar angle with respect to $\hat{z}$. The orientation distribution function is independent of the azimuthal angle φ, has up-down symmetry, and hence we can write $\psi(\hat{\omega}) = \psi(\hat{\omega}\cdot\hat{n}) = \psi(\hat{\omega}\cdot -\hat{n})$. To determine the orientation distribution function $\psi(\hat{\omega})$ for the nematic phase, we solve Eq. (2.7) using an iterative scheme on a discrete grid of polar angles $\theta \in [0, \pi/2)$ [52, 53].

2.2.2. Effective diameter

We introduce the double orientational average in the isotropic phase $\langle\langle\cdot\rangle\rangle_{\text{i}}$, as

$$\langle\langle g(\hat{\omega},\hat{\omega}')\rangle\rangle_{\text{i}} = \frac{1}{16\pi^2}\int d\hat{\omega}\int d\hat{\omega}'\, g(\hat{\omega},\hat{\omega}'), \tag{2.8}$$

for an arbitrary function $g(\hat{\omega}, \hat{\omega}')$. We now follow Ref. [41] and define [54]

$$D_{\text{eff}} = D + \alpha\kappa^{-1}, \tag{2.9}$$

with the effective double-layer thickness parameter

$$\alpha = \ln A' + \gamma_E + \ln 2 - \frac{1}{2} - \frac{4}{\pi}\langle\langle |\sin\gamma|\, \text{Ei}\left(-\frac{A'}{|\sin\gamma|}\right)\rangle\rangle_{\text{i}}. \tag{2.10}$$

One checks from Eq. (2.6) that the second-virial coefficient in the isotropic phase can be written as

$$\frac{1}{2}\langle\langle E(\hat{\omega}, \hat{\omega}')\rangle\rangle_{\text{i}} = \frac{\pi}{4}L^2 D_{\text{eff}}, \tag{2.11}$$

where we have used

$$\begin{aligned}\langle\langle |\sin\gamma|\rangle\rangle_{\text{i}} &= \frac{\pi}{4},\\ \langle\langle -|\sin\gamma|\, \ln|\sin\gamma|\rangle\rangle_{\text{i}} &= \frac{\pi}{4}\left(\ln 2 - \frac{1}{2}\right).\end{aligned} \tag{2.12}$$

Eq. (2.11) is precisely the second-virial coefficient of uncharged rods with a diameter D_{eff} (in the isotropic phase). This justifies the interpretation of D_{eff} as the effective diameter of the charged needles. The parameter α [Eq. (2.10)], which vanishes for $\mathcal{A} = 0$, is a result of the electrostatic repulsions, which effectively increase the diameter of the rods [5, 41]. The term in Eq. (2.10) involving the exponential integral has to be integrated numerically. In Fig. 2.2(b), we plot $E(\gamma)$ scaled by $2L^2 D_{\text{eff}}$ in order to emphasize the twisting effect, which is discussed in detail in the following section.

In Fig. 2.3, we present color plots as a function of κD and $\mathcal{A}$ indicating the value of (a) D_{eff} [defined in Eq. (2.9)] and (b) of effective double-layer thickness parameter α [defined in Eq. (2.10)]. We find that $D_{\text{eff}} \gg D$ (and so $\alpha > 0$) in a well-defined regime of sufficiently high $\mathcal{A}$ and low κD, whereas $D_{\text{eff}} \approx D$ (thus $\alpha \approx 0$) in the complementary region. For example, fd virus is strongly charged ($v_{\text{eff}} \geq 4\ e^-/\text{nm}$ i.e. $\mathcal{A} \geq 500$) with a diameter of $D = 6.6$ nm [55]. The effective diameter of fd virus varies from $D_{\text{eff}}/D \approx 1.0$ at high ionic strength $\kappa D = 10$ (and so $\alpha \approx 0$) to $D_{\text{eff}}/D \approx 15$ at low ionic strength $\kappa D = 0.1$ (and so $\alpha \approx 1.4$).

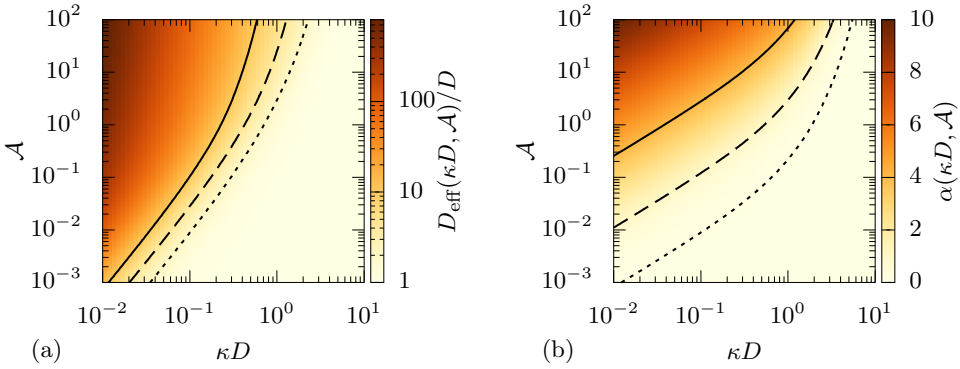

Figure 2.3.: Color plots indicating the value of (a) the scaled effective diameter $D_{\rm eff}/D$ [see Eq. (2.9)] with contours showing $D_{\rm eff}/D = 2, 4, 10$ (dotted, dashed, solid respectively) and (b) the effective double-layer thickness parameter α [see Eq. (2.10)] with contours showing $\alpha = 0.1, 1, 4$ (dotted, dashed, solid respectively) as a function of salt concentration κD and charge $\mathcal{A}$, on a log-log scale. Note that the color bar of (a) is in a log scale.

2.2.3. Twisting effect

In addition to an increase in the effective diameter, there is a second effect due to electrostatic interactions. This is a "twisting" effect that is a result of the $|\sin\gamma|^{-1}$ term in the electrostatic potential [Eq. (2.1)], first noted in Ref. [41]. While the increase in the effective diameter of the rods tends to stabilize the nematic phase, this twisting effect tends to destabilize the nematic phase, pushing the isotropic-nematic phase transition to higher concentrations. This can be qualitatively understood if we consider $E(\gamma)$ in units of $2L^2 D_{\rm eff}$ as plotted in Fig. 2.2(b), which reveals a strong γ dependence for small angles γ.

In order to describe the twisting effect quantitatively, we follow Ref. [41] and define the parameter

$$h = \frac{1}{\kappa D_{\rm eff}}, \tag{2.13}$$

such that Eq. (2.6) can be rewritten as

$$E(\gamma) = 2L^2 D_{\text{eff}} |\sin\gamma| \times \Big\{ 1 + h \Big[-\ln|\sin\gamma| - \ln 2 + \frac{1}{2} - \text{Ei}\left(-\frac{A'}{|\sin\gamma|}\right) + \frac{4}{\pi}\langle\langle |\sin\gamma| \,\text{Ei}\left(-\frac{A'}{|\sin\gamma|}\right)\rangle\rangle_{\text{i}} \Big] \Big\}. \tag{2.14}$$

In the regime where $A' \gtrsim 2$, both the Ei term and its double orientational average term in Eq. (2.14) essentially vanish. We see that in this regime only the parameter h controls the magnitude of the twisting effect, and hence $h(\kappa D, A')$ and $D_{\text{eff}}(\kappa D, A')$ completely determine the system's phase behavior. However, for weakly charged rods at a low salt concentration, A' can be small and the exponential integral terms in Eq. (2.14) can become important. In this case, the twisting effect not only depends on the combination $h(\kappa D, A')$, but also on A' separately. Nevertheless, also in this regime it would be convenient to have a single parameter that characterizes the deviation of Eq. (2.14) from an effective hard rod-like excluded volume, $2L^2 D_{\text{eff}}|\sin\gamma|$. Therefore, we define a new twisting parameter

$$\begin{aligned} H &= \frac{1}{hk}\int_0^\pi d\gamma \left[\frac{E(\gamma)}{2L^2 D_{\text{eff}}|\sin\gamma|} - 1\right]^2 \\ &= \frac{h}{k}\int_0^\pi d\gamma \times \Big[-\ln|\sin\gamma| - \ln 2 + \frac{1}{2} \\ &\quad -\text{Ei}\left(-\frac{A'}{|\sin\gamma|}\right) + \frac{4}{\pi}\langle\langle |\sin\gamma| \,\text{Ei}\left(-\frac{A'}{|\sin\gamma|}\right)\rangle\rangle_{\text{i}} \Big]^2, \end{aligned} \tag{2.15}$$

where k is a normalization factor, chosen to be

$$\begin{aligned} k &= \int_0^\pi d\gamma \left[-\ln|\sin\gamma| - \ln 2 + \frac{1}{2}\right]^2 \\ &= \frac{\pi}{12}(3+\pi^2), \end{aligned} \tag{2.16}$$

such that H reduces to h when $A' \gtrsim 2$.

In Fig. 2.4, we show the dependence of (a) the new twisting parameter H [defined in Eq. (2.15)] and (b) the old twisting parameter h [defined in Eq. (2.13)] on κD and $\mathcal{A}$. We see that the shapes of H and h differ but that they agree in the upper left corner where $A' = \mathcal{A}e^{-\kappa D}/(\kappa D) \gtrsim 2$. When $A' \lesssim 2$, h increases but in this parameter regime it is no longer physically

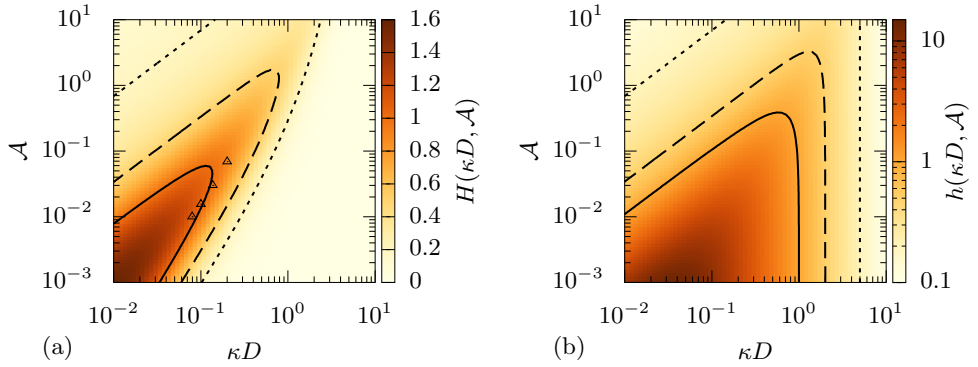

Figure 2.4.: Color plots indicating the value of (a) the new twisting parameter H [Eq. (2.15)] with contours showing $H = 0.2, 0.5, 1$ (dotted, dashed, solid respectively) and (b) the old twisting parameter h [Eq. (2.13)] with contours showing $h = 0.2, 0.5, 1$ (dotted, dashed, solid respectively) as a function of salt concentration κD and charge $\mathcal{A}$, on a log-log scale. The triangles in (a) indicate the locations of the isotropic-nematic-nematic triple points found in the phase diagrams discussed following section. Note that the color bar of (b) is in a log scale.

relevant; interestingly, Fig. 2.4(a) shows that at fixed $\kappa D \lesssim 1$, the new twist parameter H goes through a maximum as a function of $\mathcal{A}$ at some $\mathcal{A} \lesssim 10^{-1}$, which implies that a low (but non-zero) charge on the rods gives the strongest twisting effect.

In the following section we study the effect of twisting on the isotropic-nematic phase transition in charged rods. In Sec. 2.5, we compute the Frank elastic constants in order to see how they are influenced by the twisting effect.

2.3. Phase diagrams

The concentrations of the coexisting isotropic and nematic phase, c_i and c_n respectively, can be found using the condition that the osmotic pressures $P = -\left(\partial F/\partial V\right)_{N,T}$ and chemical potentials $\mu = \left(\partial F/\partial N\right)_{V,T}$ satisfy

$$P^{\text{iso}}(c_i) = P^{\text{nem}}(c_n) \tag{2.17}$$

$$\mu^{\text{iso}}(c_i) = \mu^{\text{nem}}(c_n). \tag{2.18}$$

We introduce the dimensionless effective concentration

$$c_{\text{eff}} = \frac{\pi}{4}\frac{N}{V}L^2 D_{\text{eff}}, \tag{2.19}$$

which we use rather than the usual dimensionless concentration $c = (\pi/4) \times (N/V)L^2 D$ in order to show how twisting affects the phase behavior of charged rods.

In Fig. 2.5, we show phase diagrams in the (c_{eff}, $\mathcal{A}$) plane for (a) $\kappa D = 0.3$, (b) $\kappa D = 0.2$, and (c) $\kappa D = 0.1$, where the horizontal tie-lines connect coexisting states and the color coding represents the nematic order parameter $S = \langle (3\cos^2\theta - 1)/2 \rangle$. A first glance reveals a very rich phase diagram with isotropic-nematic and nematic-nematic coexistence, including triple points and critical points. In all three phase diagrams, we see that at $\mathcal{A} = 0$ (zero charge) the expected phase transition for uncharged rods occurs, with the isotropic phase (I) existing at low concentrations, the nematic phase (N) at high concentrations, and phase coexistence between I and N in the region between $c_{\text{eff}} = 3.29$ and $c_{\text{eff}} = 4.19$. As we increase the charge, the twisting parameter increases and destabilizes the nematic phase, so that the I-N phase transition moves to higher effective concentrations c_{eff}. At this point, it is good to note that the definition of c_{eff} given in Eq. (2.19), involves the *effective* diameter, which, as shown in Fig. 2.3(a), increases with increasing $\mathcal{A}$. If we were to use the concentration c instead of the effective concentration, the I-N phase transition would move to *lower* concentrations. We will return to this point below.

We limit the phase diagrams of Fig. 2.5 to low charge, where the twisting effect is important. However, as $\mathcal{A} \to \infty$ (at fixed κD this corresponds to $h \to 0$), we also find a hard rod-like I-N transition, in agreement with Ref. [41]. Next to each phase diagram, we show the $\mathcal{A}$-dependence of the twisting parameter H, the scaled effective diameter D_{eff}/D (which is equal to the ratio c_{eff}/c), and the zeta-potential ζ, i.e., the electrostatic potential on the surface of the rod as obtained from the Poisson-Boltzmann equation in a cylindrical cell (see the appendix of this chapter).

In Fig. 2.5(b), we see that the twisting effect is large enough to cause the nematic phase to split into a low density nematic N_1 and a higher density, more aligned nematic phase N_2. The phase diagram features a nematic-nematic (N_1-N_2) critical point and an isotropic-nematic-nematic (I-N_1-N_2) triple point. Finally, in Fig. 2.5(c), we have lowered κD further and we see again a triple point, and a larger region of N_1-N_2 phase coexistence, the critical point of which is outside the plotted range.

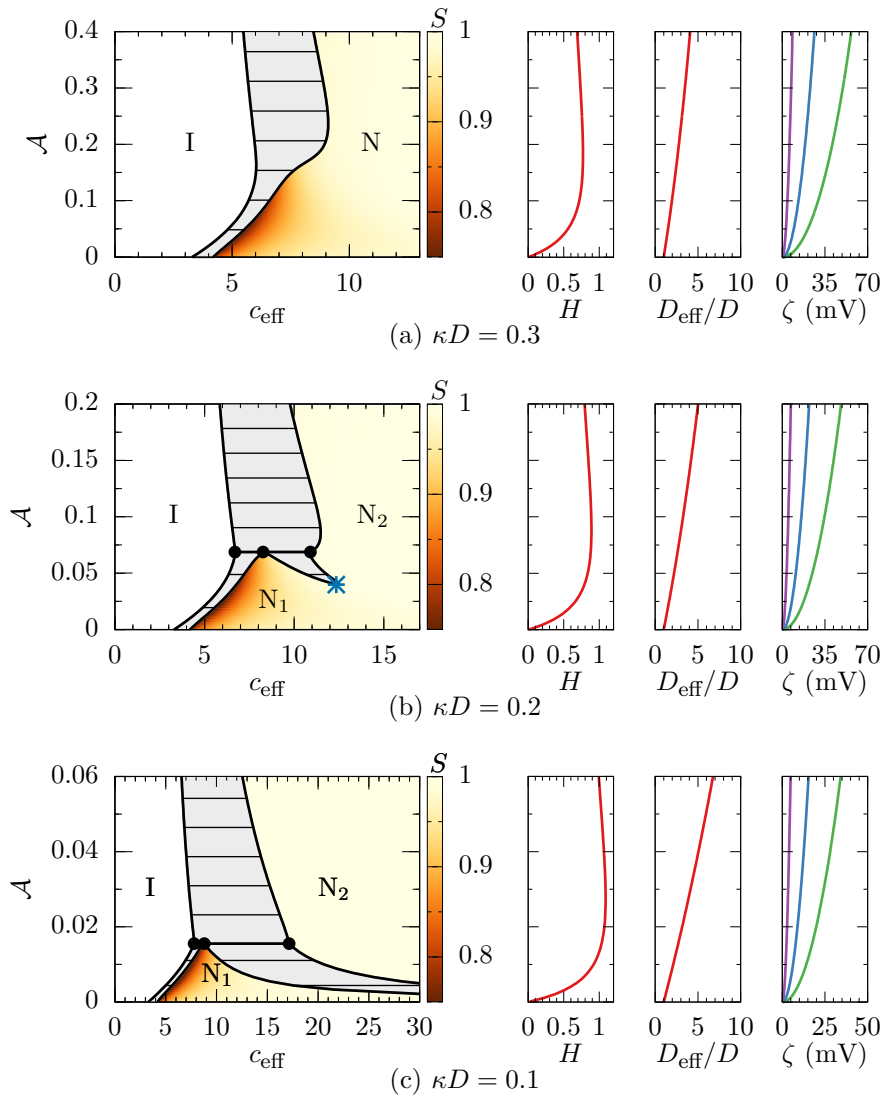

Figure 2.5.: Phase diagrams in the density c_{eff} [Eq. (2.19)]-charge $\mathcal{A}$ [Eq. (2.2)] representation for (a) $\kappa D = 0.3$, (b) $\kappa D = 0.2$, and (c) $\kappa D = 0.1$, with colors showing the nematic order parameter S, I denoting the stable isotropic phase, N the stable nematic, N_1 the weakly-aligned nematic, and N_2 the strongly aligned nematic phase. The N_1-N_2 is critical point is denoted by an asterisk and the three coexisting phases at the triple point are denoted by black dots. The tielines that connect coexisting phases are horizontal. Next to each phase diagram, the dependence of the twisting parameter H [Eq. (2.15)] and scaled effective diameter D_{eff}/D [Eq. (2.9)] on $\mathcal{A}$ is shown. In fourth column, the dependence of the zeta-potential ζ (in units of millivolts) on $\mathcal{A}$ is shown for diameter-Bjerrum length ratio $D/\lambda_B = 10, 1, 0.2$ (purple, blue, green or left to right).

In Fig. 2.6, we show three phase diagrams in the (c_{eff}, κD) plane for fixed charges characterized by (a) $\mathcal{A} = 0.08$, (b) $\mathcal{A} = 0.03$, and (c) $\mathcal{A} = 0.01$. As in Fig. 2.5, we include colors showing the nematic order parameter S and we plot the κD-dependence of the twisting parameter H, the scaled effective diameter D_{eff}/D, and the zeta-potential ζ next to each phase diagram. Note that the effective diameter increases with decreasing κD. We find again that the nematic phase can split into a weakly and strongly aligned nematic, when the twisting parameter H is of order unity (see $H(\mathcal{A}, \kappa D)$ in second columns of Figs. 2.5-2.6 and also triangles in Fig. 2.4(a) indicating locations of triple points from Figs. 2.5-2.6). Given the rather arbitrary definition of H [Eq. (2.15)], one should not expect the location of the triple points to coincide exactly with the ridge of H in Fig. 2.4(a). We stress that the phase behavior is determined by ($\mathcal{A}$, κD) and not by the single parameter H.

The phase diagrams from Figs. 2.5(b) and 2.6(b) are shown using the usual dimensionless rod concentration c in Figs. 2.7(a) and 2.7(b) to clarify the distinction between concentration and effective concentration discussed above. This representation makes explicit the lowering of the I-N transition densities with increasing charge and decreasing salt.

In order to shed light on the microscopic origin of the charge-induced nematic-nematic demixing, we show in Fig. 2.8(a) the orientation distribution functions for the two nematic phases at the triple point of Fig. 2.5(b) as a function of polar angle θ. We can relate the existence of two nematic phases to the shape of the "excluded volume" $E(\gamma)$ as a function of γ, the angle between two rods as shown in Fig. 2.8(b). We can characterize the shape of $E(\gamma)$ by introducing a cross-over angle γ^* which we give the ad hoc definition $dE(\gamma^*)/d\gamma = 4L^2 D_{\text{eff}}$ which approximately separates $E(\gamma)$ (for small γ) into a steep part for $\gamma < \gamma^*$ and a roughly linear part for $\gamma > \gamma^*$. Two rods with polar angles θ and θ' in the less aligned nematic phase can sample a larger range of $E(\gamma)$ (note that $\gamma(\theta, \theta', \varphi - \varphi') \in [0, \theta + \theta']$) and often can have an angle γ larger than γ^*. A pair of rods in the more aligned nematic phase, however, rarely has an angle γ larger than γ^*. Therefore we can understand the appearance of the denser nematic phase as a "condensation" in the pocket $0 < \gamma < \gamma^*$; the associated loss of orientational entropy is more than compensated for by the large reduction in the excluded volume.

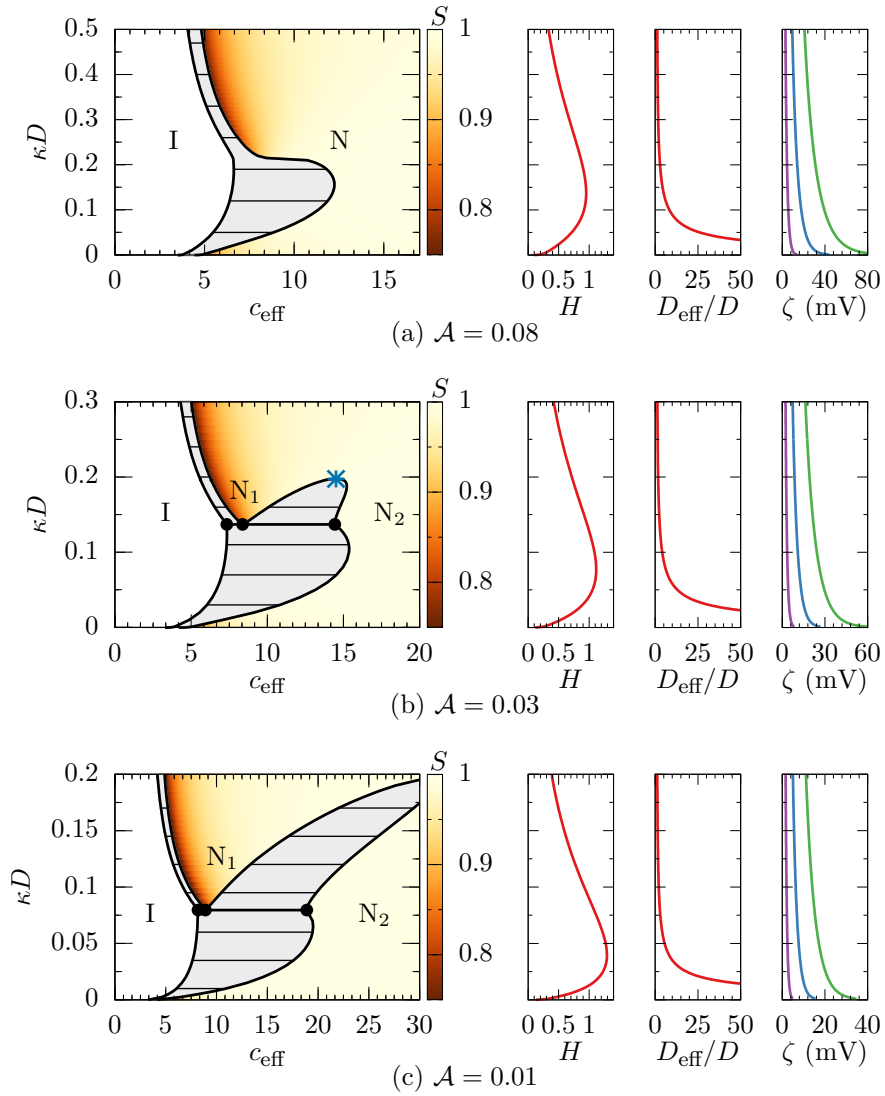

Figure 2.6.: Phase diagrams in the density c_{eff}-salt concentration κD representation for (a) $\mathcal{A} = 0.08$, (b) $\mathcal{A} = 0.03$ and (c) $\mathcal{A} = 0.01$ (see the caption of Fig. 2.5 for explanation of regions and parameters), with colors showing the nematic order parameter S. Next to each phase diagram, the dependence of the twisting parameter H and scaled effective diameter D_{eff}/D on $\mathcal{A}$ is shown. In fourth column, the dependence of the zeta-potential ζ (in units of millivolts) on κD is shown for diameter-Bjerrum length ratio $D/\lambda_B = 10, 1, 0.2$ (purple, blue, green or left to right).

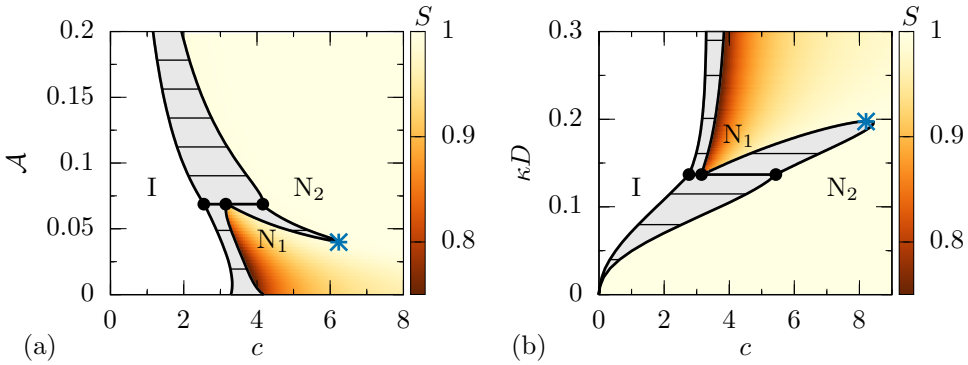

Figure 2.7.: Phase diagram in the (a) density c-charge $\mathcal{A}$ [Eq. (2.2)] representation for $\kappa D = 0.2$ [compare to Fig. 2.5(b)] and (b) density c-salt concentration κD representation for $\mathcal{A} = 0.03$ [compare to Fig. 2.6(b)], with colors showing the nematic order parameter S. The rod concentration used is $c = \frac{\pi}{4}\frac{N}{V}L^2D$. See the caption of Fig. 2.5 for explanation of regions and parameters.

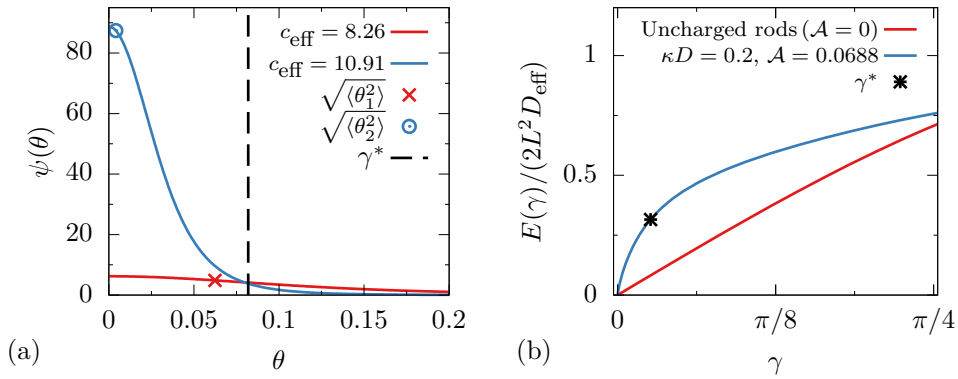

Figure 2.8.: (a) Orientation distribution functions $\psi(\theta)$ as a function of the polar angle θ for the coexisting nematic phases at I-N_1-N_2 triple point with $\kappa D = 0.2$, $\mathcal{A} = 0.0688$ [see Fig. 2.5(b)]. The low density nematic phase has effective concentration $c_{\rm eff} = 8.26$, nematic order parameter $S = 0.92$, and typical angle $\sqrt{\langle\theta_1^2\rangle} = 0.062$. The high density nematic phase has effective concentration $c_{\rm eff} = 10.91$, nematic order parameter $S = 0.99$, and typical angle $\sqrt{\langle\theta_2^2\rangle} = 0.0041$. The vertical dashed line denotes the cross-over angle γ^* that separates the "excluded volume" $E(\gamma)$ into a steep and an essentially linear regime for $\gamma < \gamma^*$ and $\gamma > \gamma^*$, respectively. (b) The "excluded volume" scaled by effective volume factor $2L^2D_{\rm eff}$ as a function of the angle γ between two rods, for uncharged rods ($\mathcal{A} = 0$) and for the triple point parameters of Fig. 2.5(b), with the cross-over angle γ^* (see text).

2.4. Relation to experimental systems

In this section, we investigate the possibility of seeing the charge-induced nematic-nematic demixing experimentally. In order for our approximations to be reliable, we require a system with $D \ll L$, $\kappa^{-1} \ll L$, and with reasonably rigid particles. We should also keep in mind that at higher densities, experimental systems of rodlike colloids undergo a nematic-smectic phase transition. For hard spherocylinders with diameter D_{eff} and aspect-ratio $L/D_{\text{eff}} > 5$ this occurs at a density approximately 47% of the close-packed density [4], which gives $c_{\text{eff}} = 3.94$, 10.32, 20.97, and 42.28 for $L/D_{\text{eff}} = 10$, 25, 50, and 100 respectively. In other words, for sufficiently long rods the smectic phase occurs far beyond the isotropic-nematic transition. For shorter rods, or rods with a smaller effective aspect ratio, $L/D_{\text{eff}} \sim 4-5$, the nematic regime is small and direct isotropic-smectic transitions are to be expected.

If we look at the phase diagram with fixed $\kappa D = 0.2$ [Fig. 2.5(b)] for instance, we see nematic-nematic coexistence at around $\mathcal{A} = 0.05$. In order for $D, \kappa^{-1} \ll L$ we could look at a system with $D = 1$ nm, $\kappa^{-1} = 5$ nm and $L \sim 100 - 1000$ nm. In water ($\lambda_B = 0.7$ nm) this gives a charge density of about $v_{\text{eff}} = 0.11\ e^-/\text{nm}$ or surface potential $\zeta = 9.3$ mV (see the appendix of this chapter), while in oil ($\lambda_B = 8$ nm), we would need $v_{\text{eff}} = 0.032\ e^-/\text{nm}$ or $\zeta = 31$ mV. Similarly, for $D = 5$ nm and $\kappa^{-1} = 25$ nm, we would need a charge density of about $v_{\text{eff}} = 0.048\ e^-/\text{nm}$ or $\zeta = 4.1$ mV in water or $v_{\text{eff}} = 0.014\ e^-/\text{nm}$ or $\zeta = 14$ mV in oil.

Compared to fd virus or tobacco mosaic virus, these are very low charge densities and zeta-potentials. For example, fd virus with a length of $L = 880$ nm, diameter $D = 6.6$ nm, and a persistence length of 2200 nm, has about $7 - 10\ e^-/\text{nm}$ at room temperature with solution pH around neutral [33, 55]. For such a high charge density, the twisting effect is small ($h \lesssim 0.15$) and also not very sensitive to ionic concentration [33]. Similarly, the more rigid tobacco mosaic virus with length $L = 300$ nm and diameter $D = 18$ nm is very highly charged around neutral pH, with about $7 - 14\ e^-/\text{nm}$ [56, 57].

Colloidal silica rods are another interesting model system as they are both monodisperse and rigid, but they have lower aspect ratios ($L/D \lesssim 22$) and bigger diameters ($D \gtrsim 200$ nm), making it hard to meet the conditions of small κD and still have $\kappa^{-1} \ll L$ [58, 59]. In Ref. [59], for instance, while $\kappa D \approx 0.1$, the surface potential is quite large ($\zeta \approx 70$ mV) and since the aspect ratio is low ($L/D \lesssim 5.6$) the silica rods form a plastic crystal phase rather than a nematic phase.

However, chemical modifications of fd can change its isoelectric point to be around a pH of 10, making it possible to tune the surface charge to arbitrarily small values [60]. Ideally, a modification of fd would be found with a slightly lower isoelectric point than pH 10, such that κ^{-1} would not be too small. Also, some polymers are rigid, have small enough diameters, and are weakly charged enough to fall in the regime of large twisting. One such a candidate is cellulose nanofibrils dispersed in water, since the surface charge density of the fibrils can be decreased to zero by lowering the pH [61]. So although some degree of tuning is needed, the predicted nematic-nematic transition seems to occur in an accessible parameter regime. An issue to consider, however, is the stability with respect to irreversible aggregation due to dispersion forces; the required low charge on the rods may not be able to balance strong Van der Waals forces so some degree of index matching may be needed.

2.5. Frank elastic constants

The strong twisting effect that we identified in the low-salt and low-charge regime raises the question to what extent the uniaxial nematic phase is actually stable with respect to spontaneous twist deformations. In general the stability of bulk nematics with respect to (weak) mechanical deformations is characterized by the Frank elastic constants K_1 (for splaying), K_2 (for twisting), and K_3 (for bending) [1, 62]. These three types of deformations are illustrated schematically in Fig. 2.9. Mechanical stability requires all three elastic constants to be positive. In this section, we check whether or not the strong twisting effect can affect the sign of K_i ($i = 1, 2, 3$) with a focus on the twist constant K_2. We derive an expression for the Frank elastic constants similar to the one derived by Vroege and Odijk [63], which is based on the derivation for uncharged rods by Straley [62].

In a distorted liquid crystal, the locally preferred orientation (i.e. the local nematic director) is given by $\hat{n}(\mathbf{r})$, where we assume that this director varies slowly in space. The relative probability of a particle at position $\mathbf{r}$ having orientation $\hat{\omega}$ is given by the locally evaluated bulk orientation distribution function $\psi(\hat{\omega} \cdot \hat{n}(\mathbf{r}))$. The excess free energy due to a director field distortion, up to second order in the gradients of $\hat{n}(\mathbf{r})$, is given in terms of the Frank

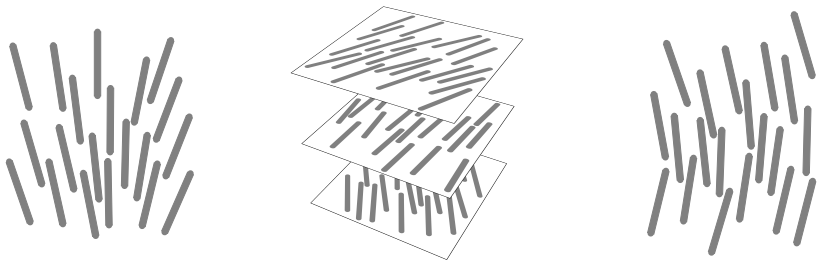

(a) (b) (c)

Figure 2.9.: Schematic illustrations of the three types of elastic deformations: (a) splay, (b) twist, and (c) bend.

elastic constants by [62]

$$\Delta F_d = \frac{1}{2}\int d\mathbf{r}\left\{K_1\left[\nabla\cdot\hat{n}(\mathbf{r})\right]^2 + K_2\left[\hat{n}(\mathbf{r})\cdot\nabla\times\hat{n}(\mathbf{r})\right]^2 + K_3\left[\hat{n}(\mathbf{r})\times\nabla\times\hat{n}(\mathbf{r})\right]^2\right\}. \tag{2.20}$$

In the appendix of this chapter, we show that within second-virial theory the Frank elastic constants are given by [63, 64]

$$\beta K_i D_{\rm eff} = -\frac{4c_{\rm eff}^2}{3\pi^2}\iint d\hat{\omega}\, d\hat{\omega}'\left\{\psi'(\hat{\omega}\cdot\hat{n})\psi'(\hat{\omega}'\cdot\hat{n})\times\frac{E(\gamma)}{2L^2 D_{\rm eff}}F_i\right\}, \tag{2.21}$$

where $\psi'(\hat{\omega}\cdot\hat{n})$ is a derivative of ψ with respect to its argument and F_i can be written in terms of local polar and azimuthal angles θ and ϕ as [64]

$$\begin{aligned}
&\text{Twist}: && F_2 = \frac{1}{4}\sin^3\theta\sin\theta'\cos(\phi-\phi')\\
&\text{Bend}: && F_3 = \cos^2\theta\sin\theta\sin\theta'\cos(\phi-\phi')\\
&\text{Splay}: && F_1 = 3F_2.
\end{aligned} \tag{2.22}$$

In Fig. 2.10, we again show the phase diagram for $\kappa D = 0.2$ in (a) the ($c_{\rm eff}$, $\mathcal{A}$) representation [see Fig. 2.5(b)] and (b) the (c, $\mathcal{A}$) representation [see Fig. 2.7(b)], with colors now showing the twist elastic constant K_2 scaled in (a) by $\beta D_{\rm eff}$ and (b) by βD. Note that K_2 is positive throughout the

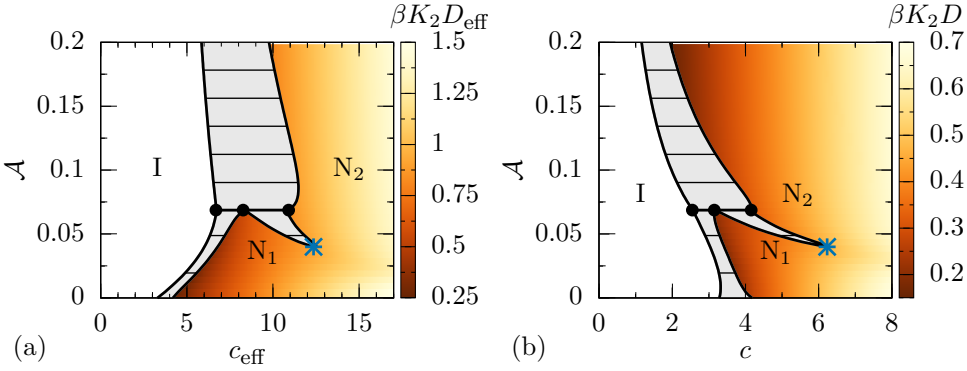

Figure 2.10.: Phase diagram in the density-charge $\mathcal{A}$ [Eq. (2.2)] representation for $\kappa D = 0.2$ (see the caption of Fig. 2.5 for explanation of regions) using (a) effective density $c_{\rm eff} = \frac{\pi}{4}\frac{N}{V}L^2 D_{\rm eff}$ and with colors showing dimensionless twist elastic constant $\beta K_2 D_{\rm eff}$ and (b) usual dimensionless density $c = \frac{\pi}{4}\frac{N}{V}L^2 D$ and with colors showing dimensionless twist elastic constant $\beta K_2 D$.

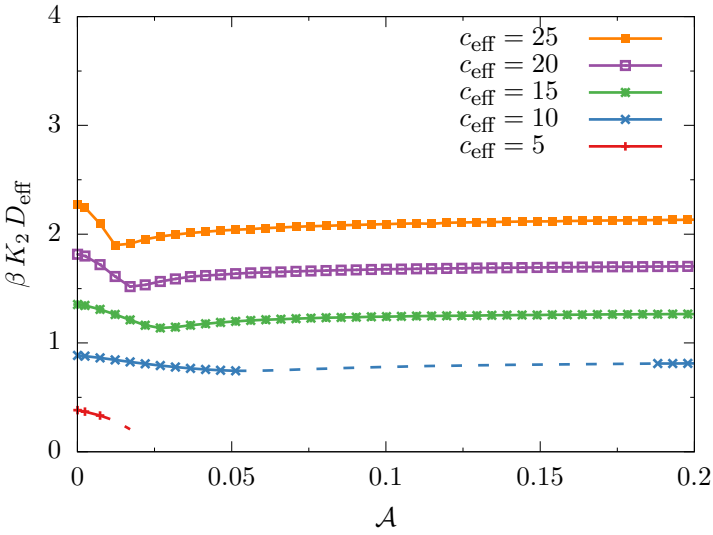

Figure 2.11.: Dependence of twist elastic constant K_2, scaled by $\beta D_{\rm eff}$, on the colloidal charge parameter $\mathcal{A}$ for screening constant $\kappa D = 0.2$ and effective concentration $c_{\rm eff} = 5, 10, 15, 20, 25$, from bottom to top. The dashed lines represent regions in the phase diagram [Fig. 2.5(b)] for which $c_{\rm eff}$ is in the two-state coexistence gap.

nematic part of the phase diagram. In Fig. 2.11, we show the twist elastic constant's dependence on the charge $\mathcal{A}$, for $\kappa D = 0.2$ and fixed values of effective concentration c_{eff}, which correspond to vertical lines in phase diagram Fig. 2.10(a). Here we see that the twist elastic constant has a hard-rod value for uncharged rods ($\mathcal{A} = 0$), decreases for small $\mathcal{A}$ (as the twisting parameter increases), and finally increases slowly back to the hard-rod value as $\mathcal{A} \to \infty$. We see that the minimum in Fig. 2.11 changes position slightly for different values of c_{eff}. This is because K_2 depends not only on the twisting effect, but also the nematic order parameter [see Fig. 2.5(b)], which first decreases and then increases with increasing $\mathcal{A}$. In addition, we calculated the bend elastic constant K_3 (not shown), which has a much stronger dependence on the nematic order parameter than K_2 does, however it is never decreased by the twisting effect. So for all parameters κD, $\mathcal{A}$ and all nematic concentrations, we find positive Frank elastic constants.

2.6. Finite aspect-ratio charged colloidal rods

In this section we investigate if spontaneous chiral symmetry breaking can occur when we consider rods of finite aspect ratio. For this purpose, we apply the recently developed second-virial density functional theory for cholesteric phases [29, 65] to a simple model of uniaxially-charged colloidal rods. This theory allows us to compute numerically the free energy F as a function of the wavenumber q of the chiral twist, for a given thermodynamic state of the system (e.g. at given temperature and density). We can therefore distinguish between a stable achiral nematic phase, for which the minimum of $F(q)$ is at $q = 0$, a stable cholesteric phase, for which the minimum of $F(q)$ is at $q^* \neq 0$, and a spontaneous breaking of the chiral symmetry, for which the minimum of $F(q)$ is at $\pm q^* \neq 0$. As stated before, finding $K_2 \propto \frac{d^2F(q)}{dq^2}|_{q=0} < 0$ would also be an indication that the system exhibits a spontaneous chiral symmetry breaking.

In analogy with Ref. [66], the colloids are modeled as hard spherocylinders (HSC) of diameter D and length L. The total charge on the rods Z is fixed by embedding N_s spheres interacting via a hard-core Yukawa potential (HY). The N_s spheres (with N_s odd) are evenly distributed along the backbone of the rod: they are separated by a distance $\delta = \frac{L}{N_s - 1}$ such that two spheres are always at the extremities of the cylindrical part of the spherocylinder.

The total pair potential between two charged rods is therefore

$$U_{12}(\mathbf{r},\hat{\omega},\hat{\omega}') = U_{HSC}(\mathbf{r},\hat{\omega},\hat{\omega}') + \sum_{i=1}^{N_s}\sum_{j=1}^{N_s} U_{HY}(r_{ij}),$$

where U_{HSC} is the hard-core potential between spherocylinders,

$$\beta U_{HSC}(\mathbf{r},\hat{\omega},\hat{\omega}') = \begin{cases} \infty & d_{\min}(\mathbf{r},\hat{\omega},\hat{\omega}') \leq D \\ 0 & d_{\min}(\mathbf{r},\hat{\omega},\hat{\omega}') > D \end{cases},$$

with $d_{\min}(\mathbf{r},\hat{\omega},\hat{\omega}')$ the minimum distance between two HSCs with center-of-mass separation $\mathbf{r}$ and orientations $\hat{\omega},\hat{\omega}'$. The sphere-sphere interaction is described by a (truncated) hard-core Yukawa potential

$$\beta U_{HY}(r_{ij}) = \begin{cases} \infty & r_{ij} < D \\ \beta\epsilon \frac{\exp[-\kappa D(r_{ij}/D-1)]}{r_{ij}/D} & D \leq r_{ij} < r_{\text{cut}} \\ 0 & r_{ij} \geq r_{\text{cut}} \end{cases}, \tag{2.23}$$

where i,j indicates spheres belonging to rods $1,2$ respectively. The parameters $\beta\epsilon$ and N_s are related by $\beta\epsilon = \left(\frac{Z}{N_s}\right)^2$, so N_s is simply a parameter that can be varied until convergence to the continuum limit is reached. As previously shown [66], this model with $N_s \geq 13$ is in excellent agreement with analytic results for the excluded volume of finite aspect-ratio rods with an effective linear charge distribution. Accordingly, we choose $N_s = 15$, which should guarantee a good agreement between the discrete-sphere and the linear-charge model. In the numerical integration we use a cutoff $r_{\text{cut}} \sim (1-2)$ L. The aspect ratio L/D, the total charge on the rod Z and the inverse of Debye screening length κD are the independent physical parameters. Our approach [29, 65] relies on the numerical calculation of the excluded volume for a set of values of the chiral wavenumber q. Such a q-dependent excluded volume is calculated by performing a Monte Carlo (MC) integration using a large number of configurations and it is then used as input to calculate the free energy as a function of the chiral wavenumber $F(q)$.[1]

We investigate a few combinations of aspect ratio (L/D) and total charge on the rods (Z), with fixed screening parameter $\kappa D = 0.2$, as reported

[1] Monte Carlo integration calculations were performed by Simone Dussi under the supervision of Marjolein Dijkstra.

in Fig. 2.12. In Fig. 2.12(a), we show the free-energy difference $\Delta F(q) = F(q) - F(q = 0)$ as a function of chiral wavenumber q, for $L/D = 10$, $Z = 1.0$ (corresponding to $\mathcal{A} = 0.034$), and two different packing fractions $\eta = 0.28$, 0.32. In some cases, we employ different q-grids to check that our results are consistent. However, within our numerical accuracy no evidence of a double minimum at $q = \pm q^* \neq 0$ has been observed for the entire set of parameters studied. From the second-derivative of $\Delta F(q)$ it is possible to calculate K_2 as a function of packing fraction η, as shown in Fig. 2.12(b) for $L/D = 10$ and two values of total charge $Z = 0.05$ ($\mathcal{A} = 8.5 \times 10^{-5}$) and $Z = 1.0$ ($\mathcal{A} = 0.034$). We see that K_2 increases with packing fraction and that the numerical uncertainty increases with packing fraction. In Fig. 2.12(c), we show the twist elastic constant as a function of packing fraction η for aspect ratios $L/D = 40$, 20, 10, 5 and different values of total charge Z on the rods. Due to the large numerical uncertainties at large packing fraction, quantitative conclusions about the actual dependence of the twist elastic constant K_2 on charge should be drawn carefully. However, as mentioned before, there are no indications that K_2 becomes negative. In addition, we show results from the previous section [i.e. Fig. 2.10(b)] for total charge on the rods $Z = 0$ ($\mathcal{A} = 0$) and $Z = 1.2$ ($\mathcal{A} = 0.051$) for aspect ratios $L/D = 40$, 20, 10 [the dashed curves in Fig. 2.12(c)]. We see that the general trend of K_2 is similar to that of the MC results for the largest aspect ratio $L/D = 40$, but as expected, Onsager theory becomes less accurate as the aspect ratio becomes smaller. In conclusion, just as in the case of infinite rods, we do not find any evidence that a linear charge distribution can induce a spontaneous chiral symmetry breaking in colloidal rods of finite length.

2.7. Summary and discussion

In this chapter, we constructed phase diagrams for charged rods within the second-virial approximation. We found that in a low salt and low, finite charge interval, where the twisting effect dominates, a coexistence between a nematic and a second, more highly aligned nematic phase occurs as well as an isotropic-nematic-nematic triple point and a nematic-nematic critical point. The required salt and shape parameters $\kappa^{-1} \sim 5D$ and $L \gg \kappa^{-1}$ are rather easy to realize experimentally, but the required low but finite zeta-potential requires some degree of tuning near the isoelectric point.

In Refs. [42, 43], a scaling analysis was used to treat the integral over the Mayer function in Eq. (2.5). Here it was predicted in a certain regime

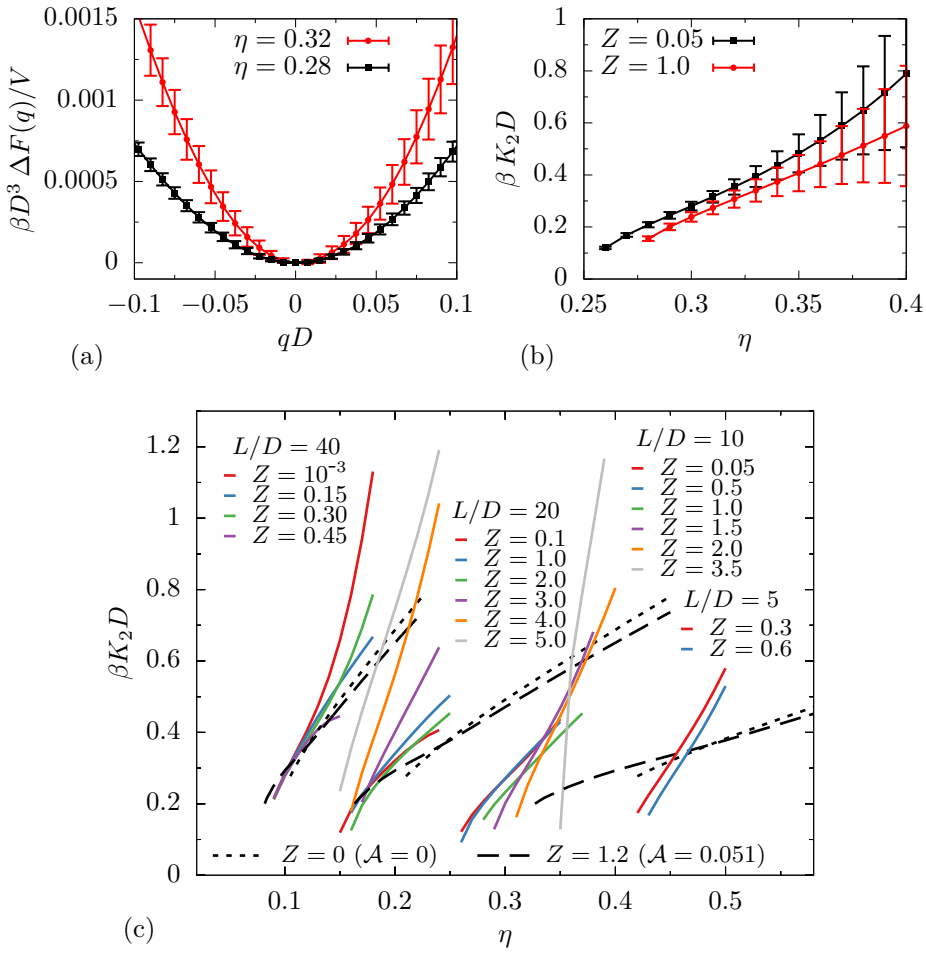

Figure 2.12.: (a) Free-energy difference $\Delta F(q) = F(q) - F(q = 0)$ as a function of chiral wavenumber qD for two different packing fractions η, and for rods with aspect ratio $L/D = 10$, total charge on rods $Z = 1.0$ (corresponding to $\mathcal{A} = 0.034$) divided over $N_s = 15$ spheres, screening parameter $\kappa D = 0.2$, and cut-off $r_{\text{cut}}/D = 20$. The error bars are calculated by averaging over 10 independent runs of 10^{10} MC steps. (b) Twist elastic constant $\beta K_2 D$ calculated from second derivative of $F(q)$ as a function of packing fraction η for $Z = 0.05$ (corresponding to $\mathcal{A} = 8.5 \times 10^{-5}$) and $Z = 1.0$ (corresponding to $\mathcal{A} = 0.034$) [for the same N_s, r_{cut}, and κD as in (a)]. (c) Twist elastic constant $\beta K_2 D$ as a function of packing fraction η for fixed screening parameter $\kappa D = 0.2$, with different aspect ratios L/D, and with different total charges Z. The solid lines are results from the MC method and the dashed lines are results from theory for $Z = 0$ ($\mathcal{A} = 0$) and $Z = 1.2$ ($\mathcal{A} = 0.051$), which are shown for aspect ratios $L/D = 40$, 20, 10 ($L/D = 5$ is outside of the plotted range).

of relatively low charge density and moderate screening, that the "excluded volume" $E(\gamma)$ is determined by steric interactions at larger angles γ whereas its angular dependence at small angles γ comes from electrostatic interactions. This competition was predicted to lead to the existence of two nematic phases, one with a weak ordering and one with a very strong ordering. This is qualitatively in agreement with our findings based on full numerical evaluations. In Ref. [44], the nematic-nematic coexistence was confirmed to be possible in the part of the regime from Refs. [42, 43] given by $D/L \ll \mathcal{A}/(2\pi) \ll (\kappa D)^2$ (the other part being ruled out due to many-body effects). This upper bound is indeed confirmed by our calculations. However, since we found that $\mathcal{A}/(2\pi)$ has values at nematic-nematic coexistence in a range $\sim 0.0025 - 0.03$, the condition for the aspect ratio D/L to be (much) smaller than this is a stricter requirement on the aspect ratio than we made in this chapter, where we set it to zero from the outset. As we used the full numerical form for $E(\gamma)$ [Eq. (2.6)] as well as numerically solved the integral equation Eq. (2.7) rather than using approximate Gaussian orientation distributions, we believe our results provide a quantitative underpinning for the nematic-nematic transitions predicted earlier in Refs. [42–44].

We calculated the twist elastic constant of the nematic phase of uniaxial charged rods. We showed that at a fixed effective concentration the twisting effect can reduce the twist elastic constant K_2, though it always remains positive. In addition, we calculated K_2 for uniaxial finite aspect-ratio rods, where we found no signs of negative K_2 either. Therefore, a uniaxial charge distribution alone seems to be not enough to break chiral symmetry, at least not within a second-virial type theory. It is an interesting possibility that by also considering the third-virial term (which includes three-body correlations), the twisting effect could be shown to stabilize a cholesteric phase. In addition, it would be interesting to see if nonlinear uniaxial charge distributions or flexibility could lead to a negative twist elastic constant. These questions are left for future studies.

Acknowledgments

We acknowledge and thank Simone Dussi for performing calculations for the finite aspect-ratio rods under the supervision of Marjolein Dijkstra. We also thank Marjolein Dijkstra and Michiel Hermes for helpful comments.

Appendix

Poisson-Boltzmann equation

In order to estimate the relation between the colloidal charge Ze and the zeta-potential ζ, we consider a single charged rod on the symmetry axis of a cylindrical cell [61]. In the long-needle limit, we can ignore end effects, and hence the potential $\psi(r, z, \varphi)$ is not only independent of the azimuthal angle φ but also of the Cartesian coordinate z that denotes the height above the center of mass of the needle, leaving only a dependence on the radial in-plane coordinate r. The Poisson-Boltzmann equation for the dimensionless potential $\phi(r) = e\beta\psi(r)$ thus takes the form

$$\phi''(r) + \frac{1}{r}\phi'(r) = \kappa^2 \sinh \phi(r), \quad r \geq D/2 \tag{2.24}$$

$$\phi(r \to \infty) = 0, \tag{2.25}$$

$$\phi'(D/2) = -4\pi\lambda_B\, \sigma, \tag{2.26}$$

where a prime denotes a derivative with respect to r and where the surface charge density $e\sigma$ is given by $\sigma = Z/(\pi LD) = v_{\text{eff}}/(\pi D)$. Equations (2.24)-(2.26) form a closed set that can be easily solved numerically on a discrete radial grid, and the required zeta-potential follows as $\zeta = k_B T \phi(D/2)/e$.

By taking the diameter as a unit of length, one easily checks that the Poisson-Boltzmann problem [Eqs. (2.24)-(2.26)] depends only on the dimensionless combinations κD and $\lambda_B v_{\text{eff}}$. However, in order to calculate ζ as a function of the charge parameter $\mathcal{A} = 2\pi(\lambda_B\, v_{\text{eff}})^2 D/\lambda_B$, one must fix D/λ_B.

Calculation of the Frank elastic constants

Within the second-virial approximation, the change in free energy due to a small spatial variation of the nematic director $\hat{n}(\mathbf{r})$ can be computed in terms of the Mayer function f as [62]

$$\Delta F_d = -\frac{1}{2} k_B T \rho^2 \iiiint d\mathbf{r}\, d\mathbf{r}'\, d\hat{\omega}\, d\hat{\omega}'\, f(\mathbf{r}' - \mathbf{r}; \hat{\omega}, \hat{\omega}') \times \psi(\hat{\omega} \cdot \hat{n}(\mathbf{r}))\big[\psi(\hat{\omega}' \cdot \hat{n}(\mathbf{r}')) - \psi(\hat{\omega}' \cdot \hat{n}(\mathbf{r}))\big]. \tag{2.27}$$

Expanding the term in square brackets to second order in derivatives of $\hat{n}$ gives

$$\begin{aligned}\psi(\hat{\omega}'\cdot\hat{n}(\mathbf{r}'))-\psi(\hat{\omega}'\cdot\hat{n}(\mathbf{r}))=\psi'(\hat{\omega}'\cdot\hat{n}(\mathbf{r}))\Big\{&(\boldsymbol{\xi}\cdot\nabla_r)\left[\hat{n}(\mathbf{r})\cdot\hat{\omega}'\right]\\&+\frac{1}{2}(\boldsymbol{\xi}\cdot\nabla_r)^2\left[\hat{n}(\mathbf{r})\cdot\hat{\omega}'\right]\Big\}\\&+\frac{1}{2}\psi''(\hat{\omega}'\cdot\hat{n}(\mathbf{r}))\left\{(\boldsymbol{\xi}\cdot\nabla_r)\left[\hat{n}(\mathbf{r})\cdot\hat{\omega}'\right]\right\}^2+\ldots,\end{aligned}$$

with $\boldsymbol{\xi}=\mathbf{r}'-\mathbf{r}$ and where $\psi'(\hat{\omega}'\cdot\hat{n}(\mathbf{r}))$ is a derivative of ψ with respect to its argument. Using this and integrating by parts to combine second order terms, we obtain for the free energy

$$\begin{aligned}\Delta F_d=-\frac{1}{2}k_BT\rho^2\iiiint d\mathbf{r}\,d\boldsymbol{\xi}\,d\hat{\omega}'\,d\hat{\omega}\,f(\boldsymbol{\xi};\hat{\omega},\hat{\omega}')\\\times\Big(\psi(\hat{\omega}\cdot\hat{n}(\mathbf{r}))\psi'(\hat{\omega}'\cdot\hat{n}(\mathbf{r}))\left\{(\boldsymbol{\xi}\cdot\nabla_r)\left[\hat{n}(\mathbf{r})\cdot\hat{\omega}'\right]\right\}\\-\psi'(\hat{\omega}\cdot\hat{n}(\mathbf{r}))\psi'(\hat{\omega}'\cdot\hat{n}(\mathbf{r}))\left\{(\boldsymbol{\xi}\cdot\nabla_r)\left[\hat{n}(\mathbf{r})\cdot\hat{\omega}\right]\right\}\left\{(\boldsymbol{\xi}\cdot\nabla_r)\left[\hat{n}(\mathbf{r})\cdot\hat{\omega}'\right]\right\}\Big).\end{aligned}\tag{2.28}$$

The first integral in Eq. (2.28) vanishes for even Mayer functions. Now we choose to write $\boldsymbol{\xi}$ as

$$\boldsymbol{\xi}=x\frac{\hat{\omega}\times\hat{\omega}'}{|\hat{\omega}\times\hat{\omega}'|}+y\,\hat{\omega}+z\,\hat{\omega}',\tag{2.29}$$

where x is the shortest distance between the rods as before (see Fig. 2.1).

We can calculate the integral over $\boldsymbol{\xi}$ in Eq. (2.28), splitting the Mayer function in two parts as

$$\begin{aligned}f(x,\gamma)&=\begin{cases}f_h, & x\le D\\ f_e & x>D\end{cases}\\&=\begin{cases}-1, & x\le D\\ \exp(-\beta U_{\mathrm{e}}(x,\gamma))-1, & x>D.\end{cases}\end{aligned}\tag{2.30}$$

The $\boldsymbol{\xi}$ integral over hard part of Mayer function, f_h is then of the form [62]

$$
\begin{aligned}
&-\int f_h(\boldsymbol{\xi};\hat{\omega},\hat{\omega}')(\boldsymbol{\xi}\cdot\mathbf{u})(\boldsymbol{\xi}\cdot\mathbf{v})\,d\boldsymbol{\xi} \qquad (2.31)\\
&=\int_{-D}^{D}dx\int_{-L/2}^{L/2}dy\int_{-L/2}^{L/2}dz\,|\hat{\omega}\times\hat{\omega}'|\\
&\quad\times\left\{y^2(\hat{\omega}\cdot\mathbf{u})(\hat{\omega}\cdot\mathbf{v})+z^2(\hat{\omega}'\cdot\mathbf{u})(\hat{\omega}'\cdot\mathbf{v})\;+x^2\frac{[(\hat{\omega}\times\hat{\omega}')\cdot\mathbf{u}]\,[(\hat{\omega}\times\hat{\omega}')\cdot\mathbf{v}]}{|\hat{\omega}\times\hat{\omega}'|^2}\right\}\\
&=\frac{1}{6}L^4D\,|\hat{\omega}\times\hat{\omega}'|\big[(\hat{\omega}\cdot\mathbf{u})(\hat{\omega}\cdot\mathbf{v})+(\hat{\omega}'\cdot\mathbf{u})(\hat{\omega}'\cdot\mathbf{v})\big]+\mathcal{O}(L^2D^3),
\end{aligned}
$$

where we introduced the shorthand notation $\mathbf{u}=\nabla_r\,[\hat{n}(\mathbf{r})\cdot\hat{\omega}]$ and $\mathbf{v}=\nabla_r\,[\hat{n}(\mathbf{r})\cdot\hat{\omega}']$ and we used the fact the rods will always overlap when $-\frac{1}{2}L<y,z<\frac{1}{2}L$ and $-D<x<D$ (other overlaps are possible, but are of order D/L). For the electrostatic part of the Mayer function, f_e, we calculate

$$
\begin{aligned}
&-\int d\boldsymbol{\xi}\,f_e(\boldsymbol{\xi};\hat{\omega},\hat{\omega}')(\boldsymbol{\xi}\cdot\mathbf{u})(\boldsymbol{\xi}\cdot\mathbf{v}) \qquad (2.32)\\
&=-2\int_{D}^{\infty}dx\int_{-L/2}^{L/2}dy\int_{-L/2}^{L/2}dz\,|\hat{\omega}\times\hat{\omega}'|\,f_e(x,\gamma)\\
&\quad\times\left\{y^2(\hat{\omega}\cdot\mathbf{u})(\hat{\omega}\cdot\mathbf{v})+z^2(\hat{\omega}'\cdot\mathbf{u})(\hat{\omega}'\cdot\mathbf{v})+x^2\frac{[(\hat{\omega}\times\hat{\omega}')\cdot\mathbf{u}]\,[(\hat{\omega}\times\hat{\omega}')\cdot\mathbf{v}]}{|\hat{\omega}\times\hat{\omega}'|^2}\right\}\\
&=-\frac{1}{6}L^4\,|\hat{\omega}\times\hat{\omega}'|\,\big[(\hat{\omega}\cdot\mathbf{u})(\hat{\omega}\cdot\mathbf{v})+(\hat{\omega}'\cdot\mathbf{u})(\hat{\omega}'\cdot\mathbf{v})\big]\times\int_{D}^{\infty}dx\,f_e(x,\gamma)\\
&\quad-2L^2\int_{D}^{\infty}dx\,x^2\frac{[(\hat{\omega}\times\hat{\omega}')\cdot\mathbf{u}]\,[(\hat{\omega}\times\hat{\omega}')\cdot\mathbf{v}]}{|\hat{\omega}\times\hat{\omega}'|}f_e(x,\gamma)\\
&=\frac{1}{12}L^2E_e(\gamma)\big[(\hat{\omega}\cdot\mathbf{u})(\hat{\omega}\cdot\mathbf{v})+(\hat{\omega}'\cdot\mathbf{u})(\hat{\omega}'\cdot\mathbf{v})\big]+\mathcal{O}(L^2D^3),
\end{aligned}
$$

where we used

$$
\begin{aligned}
E_e(\gamma)&=-2L^2\,|\sin\gamma|\int_{D}^{\infty}f(x,\gamma)\,dx \qquad (2.33)\\
&=2L^2\kappa^{-1}\,|\sin\gamma|\left[\ln\left(\frac{A'}{|\sin\gamma|}\right)+\gamma_E-\mathrm{Ei}\left(-\frac{A'}{|\sin\gamma|}\right)\right],
\end{aligned}
$$

and $|\hat{\omega} \times \hat{\omega}'| = |\sin\gamma|$. Combining Eq. (2.31) and (2.32), we have

$$\begin{aligned} &- \int f_e(\boldsymbol{\xi}; \hat{\omega}, \hat{\omega}')(\boldsymbol{\xi} \cdot \mathbf{u})(\boldsymbol{\xi} \cdot \mathbf{v})\, d\boldsymbol{\xi} \\ &= \frac{1}{12} L^2 E(\gamma) \big[(\hat{\omega} \cdot \mathbf{u})(\hat{\omega} \cdot \mathbf{v}) + (\hat{\omega}' \cdot \mathbf{u})(\hat{\omega}' \cdot \mathbf{v})\big] + \mathcal{O}(L^2 D^3). \end{aligned} \tag{2.34}$$

This agrees with Ref. [63]'s Eq. (4.2) in the regime where $A' \gtrsim 2$ (in their notation $D' = E(\gamma)/(2L^2|\sin\gamma|)$). Using Eq. (2.34) together with Eq. (2.28) and Eq. (2.20), we obtain Eq. (2.21) for the elastic constants.

Chapter 3.

Flexible boomerangs

3.1. Introduction

Steric repulsions, and therefore entropy alone, can give rise to orientationally ordered phases in systems of hard anisotropic colloids [1, 5]. Uniaxial rodlike colloids favor the isotropic phase (I) at low densities, which maximizes their orientational entropy, and at higher densities they form a nematic phase, where they align along a director to lower their excluded volume. For needle-like rods, Onsager's second-virial theory for the isotropic-nematic transition is exact [5] and therefore forms the starting point for many extensions, including those towards less elongated or less symmetric shapes. Less symmetric rigid colloids, which need three angles to describe their orientations, can form three types of homogeneous nematic phases: an oblate nematic (N_-) phase where they align along their shortest axis, a prolate nematic (N_+) phase where they align along their longest axis, and a biaxial nematic (N_B) phase, where they align along both axes. This biaxial nematic phase has been long searched for in thermotropic systems, due to its potential for opto-electronic applications [67]. Though the theoretical prediction of the biaxial nematic goes back to the 1970s [68], the observation of the N_B phase in thermotropic systems is still disputed [67].

Common biaxial particle models for studying the existence of the N_B phase are spheroplatelets, cuboids, and ellipsoids [51, 67, 69]. Monte Carlo simulations have confirmed the stability of the biaxial nematic for these particle models in certain shape and density regimes. However, in order to overcome competition with spatially ordered phases, depending on the particle model, high particle aspect ratios may be necessary [70–74]. Another biaxial particle model is that of hard boomerangs (sometimes called bent-core particles or dimers), which are usually modeled as two spherocylinders of length L and diameter D joined at one end with a certain interarm angle χ_0.

These boomerangs are not convex, and are less symmetric than the ellipsoids, spheroplatelets, or cuboids. Though ostensibly simple, boomerangs can on the basis of symmetry considerations form a large number of phases as exhaustively studied in Ref. [75]. Recently, particles with this symmetry have received increased attention due to the fact that they can form chiral phases despite being achiral themselves [76–78].

Hard needlelike boomerangs are predicted to have a so-called Landau point with a direct I-N_B transition for opening angles $\chi_0 = 107°$, with the boomerangs preferring prolate ordering above this angle and oblate ordering below this angle [79]. Thermotropic systems have a similar predicted Landau angle [80]. For lower aspect ratio boomerangs, the Landau point has been shown to shift to smaller opening angles within second-virial theory [79], whereas third-virial calculations have been shown to increase the Landau angle [81], but in both of these cases the phase diagram topology is unaffected. We expect that second-virial theory is exact in the limit that $L/D \to \infty$ [5], even for boomerangs, and in this limit the isotropic-nematic transition occurs at such a low density that competition with positionally ordered phases is not to be expected. Simulations of hard boomerangs, however, have yet to confirm this phase diagram topology [81–84]. One possible explanation for the yet unobserved biaxial nematic phase of hard boomerangs is that so far only boomerangs with relatively low aspect ratios have been simulated, where spatially ordered phases may have preempted the N_B as well as the N_- phase. These simulations also suffer from long equilibration times as the systems tend to jam close to the Landau point. However, the first experimental phase diagrams of silica boomerangs with aspect ratios of $L/D \leq 10$, also did not exhibit a biaxial nematic phase [85, 86].

Many colloidal rods with high aspect ratios are not actually rigid particles, but semiflexible [10, 87]. This semiflexibility has been shown to be key in describing the phase behavior of binary mixtures of fd virus, as the flexibility changes the effective aspect ratio of the fd virus depending on the state point [88, 89]. This was done using a theory originally developed by Wessels and Mulder [90, 91], which is based on a simple model of semiflexibility that relies on discretizing a non-convex rodlike particle into a chain of connected rigid rod segments with a bending potential that gives rise to the stiffness of the particle.

Interestingly, a recent work [92] extended the analysis of Ref. [79] from rigid boomerangs to flexible ones, and concluded that flexible boomerangs with a preferred straight configuration ($\chi_0 = 180°$) can form a biaxial nematic phase. The approach of Ref. [92] is a second-virial theory with a segmentwise

approximation for the excluded volume of two boomerangs and with an interarm bending potential. In addition, the second-virial theory is further simplified using the method of Straley [69], by considering the excluded volume of six discrete orientations of two particles and interpolating between these, which allows for all angular dependencies to be written in terms of a basis of second-rank Wigner rotation matrices.

Our purpose here is to investigate the effect of flexibility on the stability of the biaxial nematic phase for boomerangs with various preferred angles, using the method of Refs. [90, 91]. We expect our approach to be similar to that of Ref. [79] for very stiff boomerangs, since we also use a second-virial theory with a segmentwise approximation for the excluded volume. One important difference, however, is that we solve for the complete orientation distribution functions, instead of only the second-rank order parameters. In addition, we use the full form for the excluded volume within the segmentwise approximation, without interpolation or other simplifications.

This chapter proceeds as follows. In Sec. 3.2, we explain the second-virial density functional theory for hard semiflexible chains in the case of boomerangs, that is, two-segment chains, based upon Refs. [90, 91]. Additionally, we give the order parameters used to distinguish between the different phases. In Sec. 3.3, we give our results for stiff and flexible boomerangs with various preferred opening angles. Finally, we discuss these results and conclude in Sec. 3.4.

3.2. Method

We use the formalism of Wessels and Mulder [90, 91] for semiflexible chains, but only consider boomerangs, that is, chains with only two segments, where each segment is a spherocylinder of length L, diameter D, and $L \gg D$. A configuration of such a boomerang can be given by $\Omega = (\hat{\omega}_1, \hat{\omega}_2)$ where $\hat{\omega}_m$ is the unit vector describing the orientation of the mth uniaxial segment ($m = 1, 2$). We also introduce the planar interarm angle χ (see Fig. 3.1), defined by $\cos\chi = \hat{\omega}_1 \cdot \hat{\omega}_2$.

In density functional theory, we express the free energy as a functional of the single-particle density $\rho(\mathbf{r}, \Omega)$. We assume that the single-particle density has no spatial dependence, i.e. $\rho(\mathbf{r}, \Omega) = \rho\psi(\Omega)$, where $\rho = N/V$ is the average density in a system of N particles and volume V, and $\psi(\Omega)d\Omega$ is the probability to find a particle with orientation Ω in the infinitesimal interval $d\Omega$. The free energy per particle in the second-virial approximation

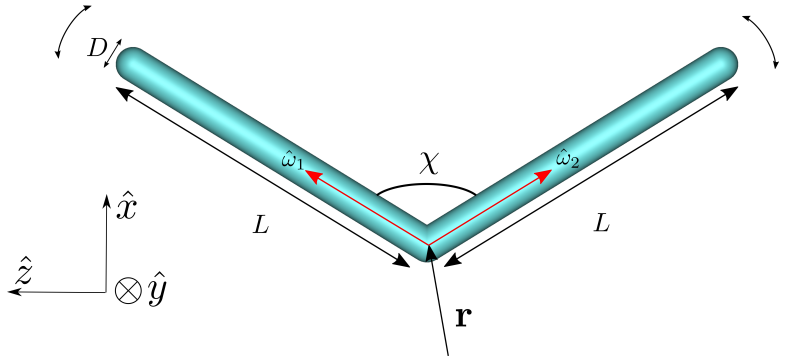

Figure 3.1.: Our model of a flexible boomerang at position $\mathbf{r}$ consisting of two spherocylinders joined at one end with an interarm angle of χ, arm lengths L, and diameter D. The red arrows show the orientations of the individual segments $\hat{\omega}_1$ and $\hat{\omega}_2$. Shown is the case with $\chi = 117°$.

can be written as

$$\frac{\beta F\left[\psi(\Omega)\right]}{N} = \ln \mathcal{V}\rho - 1 + \int d\Omega\, \psi(\Omega)\left[\ln \psi(\Omega) + u(\Omega)\right] + \frac{\rho}{2}\int d\Omega \int d\Omega' E(\Omega,\Omega')\psi(\Omega)\psi(\Omega), \tag{3.1}$$

where $\mathcal{V}$ is the thermal volume, $\beta = 1/(k_B T)$ is the inverse thermal energy, and $k_B T u(\Omega)$ is a configuration dependent bending energy of a single boomerang, which is an irrelevant constant for a rigid boomerang with a fixed opening angle χ but is of physical significance for flexible rods as we will see below. The excluded volume $E(\Omega,\Omega')$ [in Eq. (3.1)] between two boomerangs with orientations Ω and Ω' is defined as

$$\begin{aligned} E(\Omega,\Omega') &= -\int d\mathbf{r}_{12}\, f(\mathbf{r}_{12},\Omega,\Omega') \\ &= -\int d\mathbf{r}_{12}\left(\exp\left[-\beta U(\mathbf{r}_{12},\Omega,\Omega')\right] - 1\right), \end{aligned} \tag{3.2}$$

where $f(\mathbf{r}_{12},\Omega,\Omega')$ is the Mayer function, $U(\mathbf{r}_{12},\Omega,\Omega')$ is the pair potential, and $\mathbf{r}_{12} = \mathbf{r} - \mathbf{r}'$ is the vector connecting the centers of the two particles. For

hard particles we assume the pair potential to be

$$\beta U(\mathbf{r}_{12}, \Omega, \Omega') = \begin{cases} \infty, & 1 \text{ and } 2 \text{ overlap;} \\ 0, & \text{otherwise.} \end{cases} \tag{3.3}$$

However, since the excluded volume [Eq. (3.2)] of two chains is complicated to calculate for all configurations, we follow Ref. [90, 91] and use a segmentwise approximation for the excluded volume, i.e., we write

$$E(\Omega, \Omega') = \sum_{m,m'=1}^{2} e(\hat{\omega}_m, \hat{\omega}'_{m'}), \tag{3.4}$$

where $e(\hat{\omega}_m, \hat{\omega}'_{m'})$ is simply the excluded volume between two needlelike segments with $L \gg D$, given by [5]

$$e(\hat{\omega}, \hat{\omega}') = 2L^2 D \sqrt{1 - (\hat{\omega} \cdot \hat{\omega}')^2}. \tag{3.5}$$

This segmentwise approximation [Eq. (3.4)] neglects the polarity of the bent boomerangs, and it overestimates the true excluded volume worse for smaller interarm angles χ [93].

We assume that the boomerangs have a bending energy between their segments, given by [90, 91]

$$u(\hat{\omega}_1, \hat{\omega}_2) = -\frac{P}{L} \cos\left[\chi(\hat{\omega}_1 \cdot \hat{\omega}_2) - \chi_0\right], \tag{3.6}$$

where P is the persistence length and χ_0 is the preferred configuration of the boomerang, e.g., when $\chi_0 = 180^\circ$ the boomerang fluctuates around a straight rod configuration.

Equation (3.1) can be minimized with respect to the orientation distribution function (ODF) $\psi(\Omega)$ under the normalization constraint $\int d\Omega\, \psi(\Omega) = 1$, the minimizing $\psi(\Omega)$ being the equilibrium ODF [10]. The resulting Euler-Lagrange equation can be written as the non-linear self-consistency equation

$$\psi(\Omega) = \frac{1}{Z} \exp\left[-u(\Omega) - V(\Omega)\right], \tag{3.7}$$

where $Z = \int d\Omega \exp[-u(\Omega) - V(\Omega)]$ ensures the normalization of ψ and we define the self-consistent field V as

$$V(\Omega) = \rho \int d\Omega' E(\Omega, \Omega')\psi(\Omega'). \tag{3.8}$$

Although one could in principle solve Eq. (3.7) on a four-dimensional grid of polar and azimuthal angles of the two segments, it is more practical to introduce single segment distributions $\psi_m(\hat{\omega}_m)$ that only depend on a single pair of polar and azimuthal angles of the segment $m = 1, 2$. This is done by projecting the full ODF of the boomerang $\psi(\Omega)$ onto a given segment as [89, 90]

$$\psi_m(\hat{\omega}_m) = \int d\hat{\omega}_{\bar{m}}\, \psi(\Omega), \tag{3.9}$$

where $\bar{m} \neq m$ is the remaining segment. Inserting Eq. (3.7) into Eq. (3.9) results in the set of self-consistency equations for $m = 1, 2$ [90, 91]

$$\psi_m(\hat{\omega}_m) = \frac{1}{Z} q_1(\hat{\omega}_1) \exp\left[-v(\hat{\omega}_m)\right] q_2(\hat{\omega}_2), \tag{3.10}$$

where the partial-chain partition functions are given by

$$q_2(\hat{\omega}_2) = \int d\hat{\omega}_1 q_1(\hat{\omega}_1) \exp\left[-v(\hat{\omega}_1) - u(\hat{\omega}_1, \hat{\omega}_2)\right], \tag{3.11}$$

and using the normalization of ψ_m we choose $q_1(\hat{\omega}_1) = 1$. Here the single-segment self-consistent field is defined as

$$v(\hat{\omega}_m) = \rho \sum_{m'=1}^{2} \int d\hat{\omega}'_{m'} e(\hat{\omega}_m, \hat{\omega}'_{m'}) \psi_{m'}(\hat{\omega}'_{m'}), \tag{3.12}$$

such that $V(\Omega) = \sum_{m=1}^{2} v(\hat{\omega}_m)$.

We choose a coordinate system (X, Y, Z) where a segment's orientation is given by $\hat{\omega}_m = (\sin\theta_m \cos\phi_m, \sin\theta_m \sin\phi_m, \cos\theta_m)$ with ϕ_m the azimuthal angle and θ_m the polar angle with respect to $\hat{Z}$. We then numerically solve Eqs. (3.10)-(3.12) using an iterative scheme for ψ_1 and ψ_2 on a discrete grid of θ and ϕ angles, using a uniform grid of $N_\theta = 60$ and $N_\phi = 60$ angles [52, 53]. We expect this to be sufficiently accurate based on similar calculations for

uniaxial rods, which showed that $N_\theta = 40$ gave an order parameter with two digits of accuracy at the isotropic-nematic coexistence [53].

Note that we find perfect symmetry between the two segments, due to symmetry in the excluded volume and bending potentials [Eqs. (3.4) and (3.6)], and so we always find that $\psi_1(\hat{\omega}) = \psi_2(\hat{\omega})$. From the equilibrium ODFs $\psi_m(\hat{\omega}_m)$, we can compute the free energy, pressure, and chemical potential [90, 91], and hence the phase diagram following the standard procedure. For convenience we define a dimensionless density $c = \rho(\pi/4)(2L)^2 D$, which reduces to the usual definition for the case of a straight rigid rod of length $2L$ and diameter D.

In addition, we recover the full equilibrium ODF from the segment ODFs using [90]

$$\psi(\hat{\omega}_1, \hat{\omega}_2) = \frac{1}{Z} \exp\left[-v(\hat{\omega}_1) - v(\hat{\omega}_2) - u(\hat{\omega}_1, \hat{\omega}_2)\right]. \tag{3.13}$$

It also turns out to be convenient to introduce (i) the boomerang's frame (x, y, z), defined to be the orthogonal basis proportional to ($\hat{\omega}_1 + \hat{\omega}_2$, $\hat{\omega}_1 \times \hat{\omega}_2$, $\hat{\omega}_1 - \hat{\omega}_2$), see also Fig. 3.1, and (ii) the Euler angles α, β, γ that transform the particle frame to a reference frame, which together with the interarm angle χ fully determine the particle configuration (and are equivalent to $\hat{\omega}_1, \hat{\omega}_2$). We define the orientational average as $\langle\cdot\rangle = \int d\hat{\omega}_1 \int d\hat{\omega}_2 (\cdot)\psi(\hat{\omega}_1, \hat{\omega}_2)$. This allows us to calculate the probability density $g(\chi)$ for an internal configuration with interarm angle χ, which we define as

$$g(\chi) = \langle \delta(\chi - \arccos(\hat{\omega}_1 \cdot \hat{\omega}_2)) \rangle, \tag{3.14}$$

where δ is the Dirac delta function. We define the average interarm angle as $\langle\chi\rangle$ and the standard deviation of the bending fluctuations as

$$\sigma_\chi = \sqrt{\langle\chi^2\rangle - \langle\chi\rangle^2}. \tag{3.15}$$

In order to be able to distinguish and characterize the (symmetries of the) equilibrium ODF, we also define four order parameters following the

notation of Rosso [94]

$$S = \frac{1}{2}\langle(3\cos^2\beta - 1)\rangle, \tag{3.16}$$

$$U = \frac{\sqrt{3}}{2}\langle\sin^2\beta\cos 2\gamma\rangle, \tag{3.17}$$

$$P = \frac{\sqrt{3}}{2}\langle\sin^2\beta\cos 2\alpha\rangle, \tag{3.18}$$

$$F = \langle\frac{1}{2}(1+\cos^2\beta)\cos 2\alpha\cos 2\gamma - \cos\beta\sin 2\alpha\sin 2\gamma\rangle. \tag{3.19}$$

In the isotropic phase (I) all four of these order parameters are zero. A uniaxial nematic phase has S nonzero and $P = F = 0$, where $S > 0$ corresponds to a prolate nematic phase N_+ and $S < 0$ to an oblate nematic phase N_-. Note that $U \neq 0$ if the particles are biaxial as we have here for $\chi_0 \neq 180°$. In a biaxial nematic phase (N_B), all four are nonzero with P describing the phase biaxiality, and F describing both the phase and particle biaxiality. We also consider the segment order parameters $S_m = \frac{1}{2}\langle(3\cos^2\theta_m - 1)\rangle$, where θ_m is the polar angle with respect to the nematic director $\hat{n}$, which we determine as the eigenvector with the largest eigenvalue (S_m) of the diagonalized segment ordering tensor [1].

For the case of a boomerang with a preferred angle of $\chi_0 = \pi/2$, we do not expect biaxial order with a two-fold rotational symmetry, but instead four-fold rotational symmetry (called the D_4 phase in Ref. [95]), and so we also define the additional fourth-rank order parameter [95]

$$C = \cos^8\frac{\beta}{2}\cos[4(\alpha+\gamma)] + \sin^8\frac{\beta}{2}\cos[4(\alpha-\gamma)]. \tag{3.20}$$

In the isotropic or uniaxial nematic phase $C = 0$, while for an N_B phase $F \neq 0$ and $C \neq 0$ and in the D_4 phase $F = 0$ and $C \neq 0$ [95].

Due to our discrete grid of θ and ϕ angles, the Euler angles will sometimes not be correctly distributed (e.g. γ is not even defined in the case of straight rods), and so we will set a threshold of 0.1 for the absolute value of non-vanishing order parameters.

3.3. Results

We first consider stiff particles with a persistence length of $P/L = 100$, which corresponds to bending fluctuations on the order $\sigma_\chi \lesssim 6°$, with these fluctuations only weakly depending on density. The single-segment ODF, together with information about the interarm angle can provide a qualitative understanding of the full boomerang ODF, which is a function of four angles. Therefore, in Fig. 3.2, we show the equilibrium single-segment ODF $\psi_1(\theta, \phi)$ on the grid of the θ and ϕ angles using the Winkel Tripel map projection for ease of viewing, for various densities c and preferred opening angles χ_0. We also include a schematic representation of the possible phases in the lower left corner of each plot. In Fig. 3.2(a), the boomerangs prefer a straight orientation ($\chi_0 = 180°$), and at density $c = 5$ we find a prolate nematic phase where segments prefer orientations parallel or antiparallel to the nematic director $\hat{n}$ along the map pole. They also prefer to be essentially antiparallel to each other, since $\sigma_\chi \approx 3.1°$ and $\langle\chi\rangle \approx 174°$. Next, in Fig. 3.2(b), we consider particles with an intrinsic biaxiality due to a preferred opening angle $\chi_0 = 117°$, which at density $c = 20$ form a biaxial nematic phase. Here we find the average interarm angle to be $\langle\chi\rangle \approx 119°$ and the standard deviation to be $\sigma_\chi \approx 5.5°$. We conclude that if the first segment has an orientation e.g. in the peak in the upper left of Fig. 3.2(b), then the second segment must have an orientation approximately given by the peak in the lower left, or else the particle's interarm angle would differ significantly from the average interarm angle. Therefore, in this N_B phase, particles have two preferred orientations related by the transformation $\hat{x} \to -\hat{x}$ and so the segment ODF has four peaks. For a preferred angle of $\chi_0 = 90°$, the particles are platelike and stiff with $\langle\chi\rangle \approx 90°$ and $\sigma_\chi \approx 5.6°$. As evident from the single equatorial peak in Fig. 3.2(c) for $c = 15$, we find that they form an oblate nematic with $\hat{n}$ along the pole. Finally, in Fig. 3.2(d) we see that for $\chi_0 = 90°$ and $c = 20$, the boomerangs form a D_4 phase with four-fold symmetry, with the four preferred orientations being related by the transformations $\hat{x} \to -\hat{x}$, $\hat{x} \to \hat{z}$, and $\hat{x} \to -\hat{z}$.

After this illustration of the nature of the single-segment distributions $\psi_1(\hat{\omega})$, we now use the full ODF $\psi(\hat{\omega}_1, \hat{\omega}_2)$ to calculate the order parameters defined from the particle frame [Eqs. (3.16)-(3.20)]. These are shown in Fig. 3.3 as a function of the density c for stiff boomerangs ($P/L = 100$) with preferred opening angles of (a) $\chi_0 = 180°$, (b) $\chi_0 = 117°$, and (c) $\chi_0 = 90°$. For the rodlike particles in Fig. 3.3(a), we find the expected first order I-N_+ transition with coexisting isotropic density $c_i \approx 3.34$ and nematic

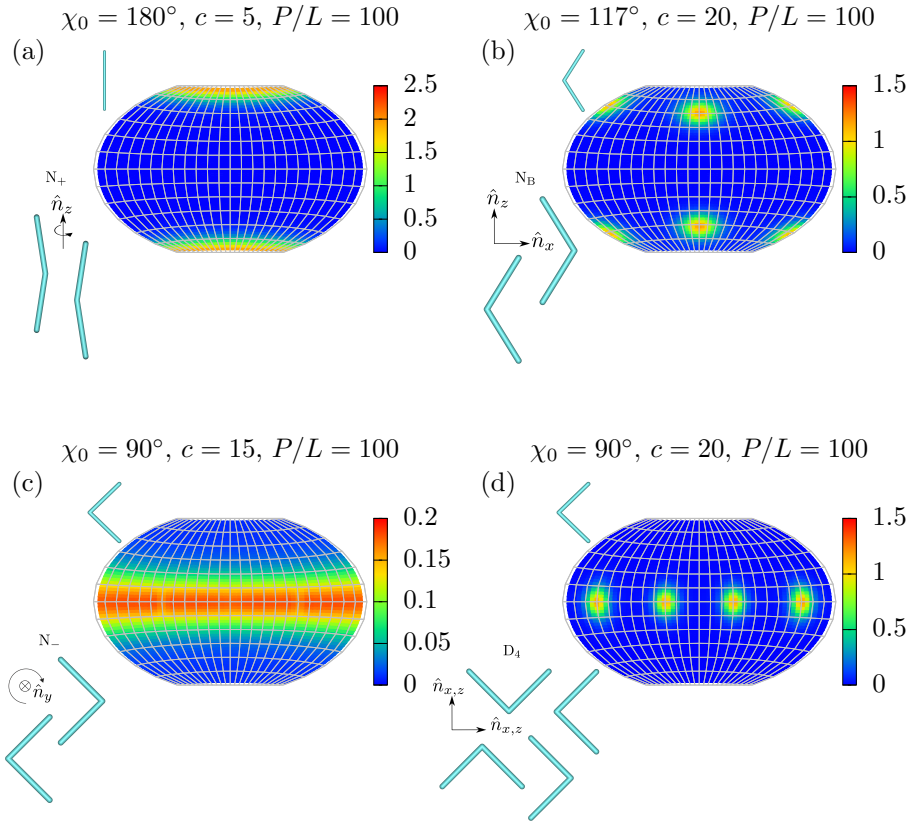

Figure 3.2.: Examples of segment orientation distribution functions $\psi_1(\theta, \phi)$ for stiff particles with $P/L = 100$ for various preferred angles χ_0 and densities c. For $\chi_0 = 180°$ and $c = 5$ (a) we find a prolate nematic N_+. For $\chi_0 = 117°$ and $c = 20$ (b) we find a biaxial nematic N_B where boomerangs align their long axis $\hat{z}$ with the pole. For $\chi_0 = 90°$ and $c = 15$ (c) we find an oblate nematic N_- with director parallel to the pole. For $\chi_0 = 90°$ and $c = 20$ (d) we find a D_4 phase with boomerangs having four equivalent preferred orientations related by a rotation of $\pi/2$. Illustrations in the upper left corners show a boomerang with the corresponding interarm angle χ_0. Illustrations in the lower left corner show a schematic representation of each phase with the subscript on the nematic director $\hat{n}$ indicating which particle axis is aligned along it, and with arrows around the director indicating symmetry under rotations around the director.

density $c_n \approx 4.17$, which we determine using the conditions of mechanical and chemical equilibrium, and which are very similar to those of rigid uniaxial rods. We note that the fact that U is a small nonzero number at low densities is an artifact of calculating the Euler angle γ for a particle with segments restricted to our numerical grid, and is not physically meaningful. Also, we note that the segment order parameter $S_1 \approx S$ since S measures alignment of the particle's $\hat{z}$ axis (see Fig. 3.1), which in this case is approximately the same as the segment orientation. In Fig. 3.3(b), we find an I-N_+ transition at $c_i \approx 9.55$ and $c_n \approx 9.70$ followed by an N_+-N_B transition at $c \approx 18$ which we determine by comparing the absolute value of the biaxial order parameters P and F to the threshold of 0.1. Since $S > S_1$ in this case, the main particle axis $\hat{z}$ is more aligned with the nematic director at high density than the segments are due to the bent shape of the particle. Finally, in Fig. 3.3(c), we find a very weakly first order I-N_- transition at $c_i \approx c_n \approx 14$ and an N_--D_4 transition at $c \approx 16$.

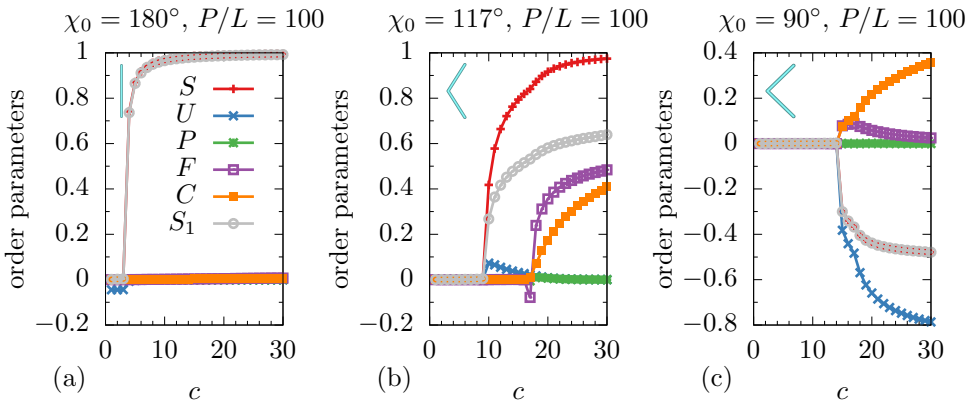

Figure 3.3.: Order parameters defined in Eqs. (3.16)-(3.20) as a function of density c for stiff boomerangs ($P/L = 100$) with preferred angles (a) $\chi_0 = 180°$, (b) $\chi_0 = 117°$, and (c) $\chi_0 = 90°$. The key applies to (a)-(c).

Next we consider semiflexible boomerangs with $P/L = 10$. In this case the bending fluctuations have a greater dependence on density, and so in Fig. 3.4 we plot the interarm probability density $g(\chi)$ for several densities c and for three preferred angles (a) $\chi_0 = 180°$, (b) $\chi_0 = 117°$, and (c) $\chi_0 = 90°$. We see in Fig. 3.4(a) that this distribution becomes more peaked and shifts to higher χ with increasing c. This effect is more pronounced in Fig. 3.4(b), where the boomerangs have $\langle\chi\rangle \approx \chi_0$ at low densities, but

pay a bending energy to straighten and hence to pack more efficiently at higher densities. In Fig. 3.4(c), we see that at densities $c \leq 15$ the particles fluctuate around $\langle\chi\rangle \approx \chi_0 = 90°$, but at high density $c = 20$, $g(\chi)$ has two peaks, one at small χ where segments are almost bent on top of each other and one at large χ where the particles are roughly straight. This is an artifact of our segmentwise excluded volume approximation, in which these two configurations have the same excluded volume and also cost the same bending energy because $\chi_0 = 90°$. In this case the full excluded volume as well as intersegment excluded volume should actually be considered. We will use the small-χ peaks that may develop in $g(\chi)$ to inform us of the break down of our model at high densities and high flexibilities.

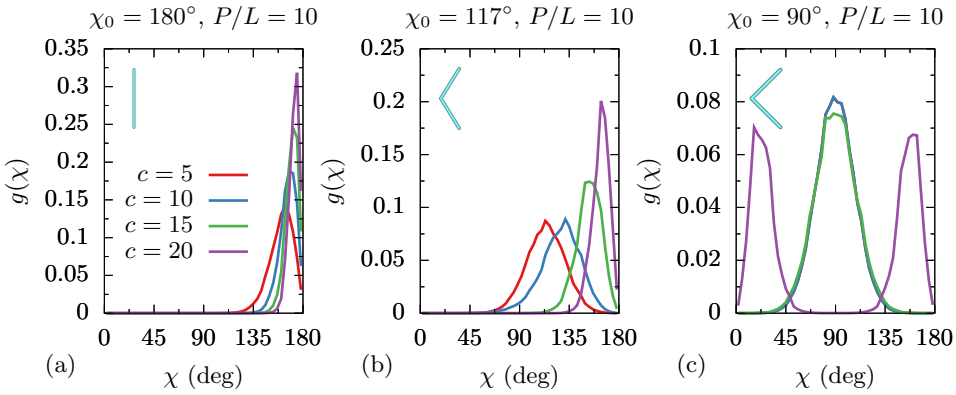

Figure 3.4.: Probability density g of the interarm angle χ for semiflexible boomerangs ($P/L = 10$) at densities $c = 5, 10, 15, 20$ for preferred angles (a) $\chi_0 = 180°$, (b) $\chi_0 = 117°$, and (c) $\chi_0 = 90°$. In (a), all four densities shown correspond to N_+ phases. In (b), $c = 5$ corresponds to the isotropic phase, while $c = 10, 15, 20$ correspond to the N_+ phase. In (c), $c = 5, 10$ correspond to the isotropic phase (we note that the blue and red curves are on top of each other), while $c = 15$ corresponds to the N_- phase and $c = 20$ corresponds to the N_+ phase. The key applies to (a)-(c).

In Fig. 3.5, we plot the average interarm angle $\langle\chi\rangle$ in (a) and the standard deviation σ_χ in (b), both as a function of the density c for five different preferred angles χ_0. As discussed, in the case of $\chi_0 = 90°$, our approximation breaks down at $c > 15$ where σ_χ becomes exceedingly large due to the spurious small-χ peak that develops. In all other cases, however, the particles tend to straighten with increasing density ($\langle\chi\rangle$ approaches 180°), which costs

bending energy but reduces their excluded volume. In addition, they tend to fluctuate less with increasing density (σ_χ decreases).

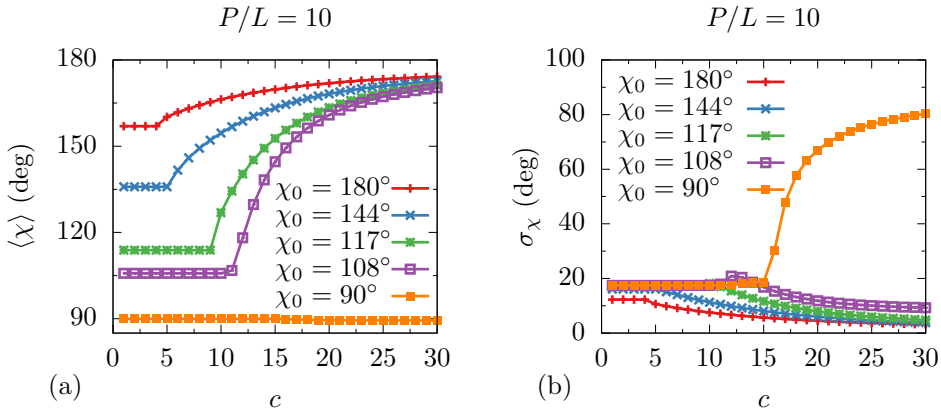

Figure 3.5.: (a) Average interarm angle $\langle\chi\rangle$ and (b) standard deviation of the interarm angle σ_χ, both as a function of the density c for flexible boomerangs with $P/L = 10$ and various preferred angles χ_0.

Next, in Fig. 3.6 we consider the order parameter trends of semiflexible boomerangs with $P/L = 10$ and with preferred opening angles of (a) $\chi_0 = 180°$, (b) $\chi_0 = 117°$, and (c) $\chi_0 = 90°$. In Fig. 3.6(a), for boomerangs with a preferred straight configuration, there is an I-N_+ transition as in the case of stiff boomerangs, but this has shifted to higher densities with $c_i \approx 4.05$ and $c_n \approx 4.54$. The density gap $c_n - c_i$ is therefore also reduced compared with stiffer rods, in agreement with flexible needles in the continuum limit [89–91, 96–98]. In the case of Fig. 3.6(b), after the isotropic-prolate nematic transition, these semiflexible boomerangs do not transition to a biaxial nematic phase as their stiff counterparts did, but instead deform from their preferred angle $\chi_0 = 117°$ to straighter configurations in the prolate nematic phase, as also discussed above. In Fig. 3.6(c), the boomerangs have an I-N_- transition as they did in the stiff case, but instead of forming a D_4 at high densities, they rather deform into straighter boomerangs and form an N_+ phase. However, as discussed above, the segmentwise approximation breaks down and we no longer trust our calculation at $c > 15$ in Fig. 3.6(c).

We use the order parameters and the thermodynamic quantities to construct phase diagrams in the (χ_0, c) representation in Fig. 3.7 for the four different persistence lengths: (a) $P/L = 100$, (b) $P/L = 20$, (c) $P/L = 10$,

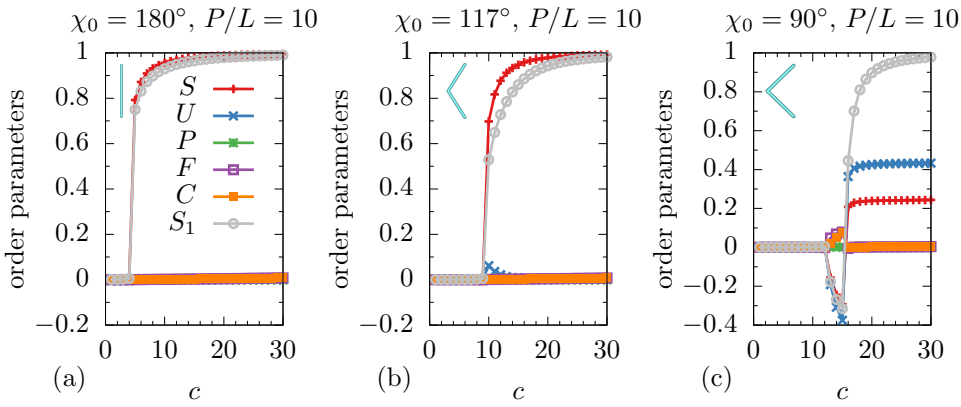

Figure 3.6.: Order parameters as a function of density c for semiflexible boomerangs ($P/L = 10$) with preferred angles (a) $\chi_0 = 180°$, (b) $\chi_0 = 117°$, and (c) $\chi_0 = 90°$. The key applies to (a)-(c).

and (d) $P/L = 5$. In addition, we use the probability distribution for interarm angles $g(\chi)$ to set an approximate criterion of $\int_0^{\pi/4} d\chi\, g(\chi) > 0.1$ to signify the break down of the theory, which is shown as a crosshatched region in the phase diagrams of Fig. 3.7. In the rigid case of Fig. 3.7(a), we see an isotropic phase at low densities, with a transition at higher densities to a prolate nematic when $\chi_0 > 112°$ and to an oblate nematic when $\chi_0 < 112°$. This separation between prolate and oblate ordering at $\chi_0 \approx 112°$ is similar to the Landau angle of $\chi_0 = 107°$ found for rigid boomerangs in Ref. [79]. We do not see a direct isotropic to biaxial nematic transition due to our threshold of 0.1 for the order parameters, which is not unexpected since the order parameters are predicted to be small close to the Landau point. In addition, as discussed, we do not find an N_B phase but rather a D_4 phase for preferred angles close to $\chi_0 = 90°$. In Fig. 3.7(b), we find a similar topology, but see that the flexibility destroys much of the region of biaxial nematic stability, with the prolate nematic phase encroaching on this region and the separation between the N_- and N_+ moving to smaller angles. The mechanism is the relatively cheap energy penalty to bend the boomerangs into needle-shaped objects. For the even more flexible boomerangs in Fig. 3.7(c), there is no longer a biaxial nematic or D_4 phase. Finally, in the most flexible case studied here [Fig. 3.7(d)], we see that the region in which we predict our approximation to break down has become larger.

In Ref. [92], high flexibility was shown to cause spontaneous formation of biaxial nematics from boomerangs with $\chi_0 = 180°$, which are uniaxial on average. However, we found only uniaxial prolate nematic phases for $\chi_0 = 180°$ even for $P/L = 5$ ($\sigma_\chi \lesssim 13°$) and $P/L = 1$ ($\sigma_\chi \lesssim 50°$) (not shown). The latter case is so flexible that even at low densities for $\chi_0 = 180°$, $g(\chi)$ has a peak at small angles, so we no longer trust our approximation there.

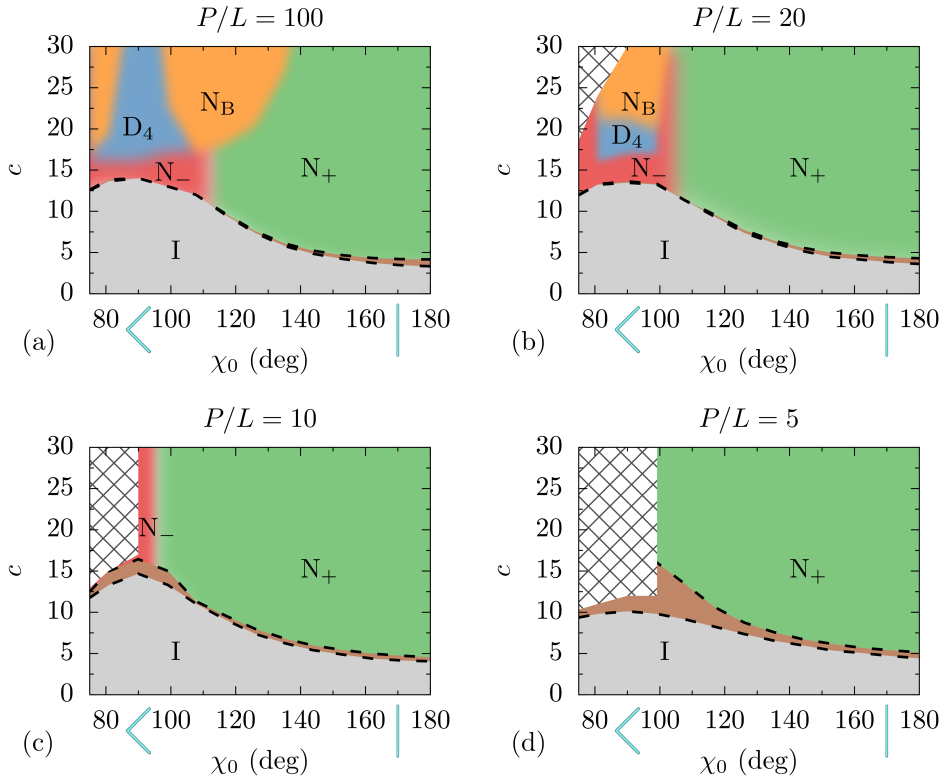

Figure 3.7.: Phase diagrams in the preferred angle χ_0 and density c representation for semiflexible boomerangs with a persistence length of (a) $P/L = 100$, (b) $P/L = 20$, (c) $P/L = 10$, and (d) $P/L = 5$. Crosshatched regions denote the breakdown of the segmentwise approximation for the excluded volume. The illustrations along the horizontal axis show the particle shape for $\chi = 90°$ and $\chi = 180°$.

3.4. Discussion and conclusions

In this chapter, we used second-virial density functional theory for semiflexible chains to study the phase behavior of hard semiflexible boomerangs with different persistence lengths and preferred angles. For stiff boomerangs, we found that the separation between prolate and oblate ordering occurs at $\chi_0 \approx 112°$, which is similar to the Landau angle of $\chi_0 = 107°$ reported for rigid boomerangs [79]. However, our phase diagram has a limited region of oblate nematic stability, due to the preference of platelike boomerangs to form a D_4 phase with four-fold rotational symmetry. This phase requires fourth-rank order parameters to identify it, and was neglected in the work of Ref. [79] where only second-rank order parameters were considered.

In contrast with recent results [92], we did not find any evidence of a biaxial nematic phase composed of flexible boomerangs with a straight preferred configuration, which are uniaxial particles on average. Moreover, we found that even for particles that are intrinsically biaxial, flexibility discourages the formation of biaxial nematic phases in favor of prolate nematic phases. The underlying mechanism that we identified here is that, at high densities, the flexible boomerangs tend to stretch out in order to reduce their excluded volume. This is similar to an experimentally observed stretching of semiflexible polymer coils in a background nematic in Ref. [99], which was shown by theory in Ref. [88].

Using the excluded volume in the segmentwise approximation, as was also done in other works studying boomerangs [79, 92], allowed us to formulate the theory in terms of single segment properties, from which the full particle orientation distribution functions and thermodynamics can nevertheless be deduced. We expect this approach to be more accurate than the method based on directly solving for the set of four second-rank order parameters as was done in Ref. [79] for rigid boomerangs and in Ref. [92] for flexible boomerangs. For instance, only considering the second-rank order parameters limits the possible phases that can be studied, excluding for example the D_4 phase. Moreover, Ref. [92] is based on the additional approximation of interpolating the excluded volume between six known configurations in order to write it in terms of four angles (three relative Euler angles plus one interarm angle), even though for the flexible case actually five angles would have been needed within this method: three relative Euler angles plus the interarm angles of both particles. Note however that the segmentwise excluded volume in terms of the segment orientations only depends on four angles, the cosines of which being the dot products of the orientations of

each pair of segments. Our method not only yields richer information as we have the full boomerang orientation distribution function, but it also has the advantage of being able to treat flexible boomerangs with a bent preferred configuration.

However, a drawback of the currently used approach of the segmentwise approximation is that it neglects the polarity of the boomerangs, which becomes worse for very bent configurations. We saw that in the case of very flexible particles at high densities, this led to spurious results where the boomerangs tended to prefer "closed up" configurations with small interarm angles. The recently developed strategy to use Monte Carlo calculations to calculate the excluded volume kernel $E(\Omega, \Omega')$ more precisely [29, 65] could be used for going beyond the segmentwise approximation, and may reveal polar or chiral phases in the phase diagrams [75, 78, 93].

Acknowledgments

We thank Massimiliano Chiappini, Marjolein Dijkstra, and Simone Dussi for useful discussions.

Chapter 4.

Rigid boomerangs

4.1. Introduction

Less symmetric than rods, boomerangs are an ostensibly simple particle model that can potentially form a large number of phases [75]. In Chapter 3, we studied hard, flexible boomerangs using the fact that a boomerang is made of two uniaxial segments to simplify the form of the excluded volume. We saw that this segmentwise approximation for the excluded volume breaks down as the boomerangs become more bent. In this chapter, we numerically calculate the excluded volume for rigid boomerangs, in order to go beyond the segmentwise approximation used in Chapter 3 for flexible boomerangs and in Ref. [79] for rigid boomerangs. This allows us to study rigid boomerangs with any fixed interarm angle χ (see particle model in Fig. 4.1).

A boomerang is a biaxial particle that needs three Euler angles (see Appendix A) to describe its orientation if is rigid, or four angles if it is flexible. Though in principle the excluded volume and equilibrium orientation distribution functions could be calculated on a grid of the three Euler angles, here we utilize an alternative method of expanding in basis functions to solve the Euler-Lagrange equation.

In Chapter 3, we only considered spatially homogeneous phases. For shorter particles, the range of stability of the nematic phases may be severely limited by positionally ordered phases, such as smectic or columnar phases. For rigid boomerangs with $L = 5D$, Monte Carlo simulations found that while above $\chi \approx 135°$ there was an isotropic to prolate nematic to smectic phase sequence with increasing packing fraction, below $\chi \approx 135°$ there was no nematic due to a direct isotropic to smectic sequence [82]. Furthermore, Ref. [82] found that the smectic phase switches from a non-polar smectic A to polar smectic A with decreasing χ at $\chi = 167°$. Similar results were found in experiments of rigid silica boomerangs with $L/D \leq 10$, where various smectic

phases were observed, but no nematic phases [85, 86]. Our goal in this chapter is to examine the nematic phase behavior of hard, rigid boomerangs with all possible opening angles, and examine the stability of the nematic phases with respect to smectic phases.

In Sec. 4.2, we describe the expansion in a basis of Wigner matrices and give the Euler-Lagrange equation. Then, in Sec. 4.3 we describe the bifurcation analysis used to study the stability of the nematic phases with respect to smectic perturbations. We show the order parameters and phase diagrams Sec. 4.4. Finally, we conclude in Sec. 4.5.

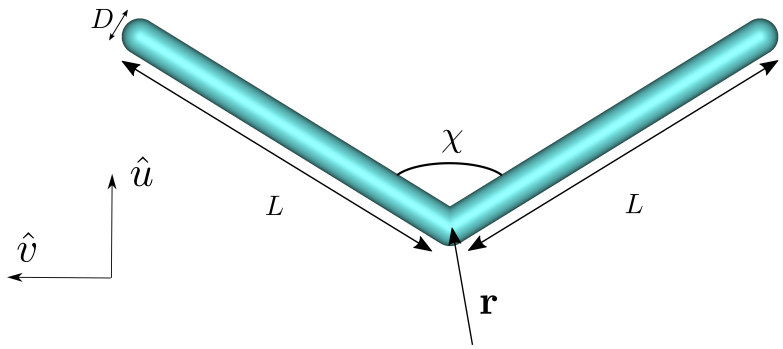

Figure 4.1.: Our model of a rigid boomerang at position $\mathbf{r}$ consisting of two spherocylinders joined at one end with an interarm angle of χ, arm lengths L, and diameter D. Shown is the case with $\chi = 117°$. The particle's "longest" axis is defined to be $\hat{v}$ for $\chi \geq 90°$ and $\hat{u}$ for $\chi < 90°$.

4.2. Expansion in Wigner matrices

We expand all Euler angle dependencies in a complete basis of Wigner matrices $\mathcal{D}^l_{mn}(\Omega)$ (see also Appendix B). For the excluded volume [Eq. (1.12)] this gives

$$E(\Omega_{12}) = \sum_{l=0}^{\infty} \sum_{m,n=-l}^{l} E^l_{mn} \mathcal{D}^l_{mn}(\Omega_{12}), \tag{4.1}$$

where we can use the orthogonality of the Wigner matrices [Eq. (B.5)] to write the coefficients as

$$E^l_{mn} = \frac{2l+1}{8\pi^2} \int d\Omega\, E(\Omega)\, \mathcal{D}^l_{mn}(\Omega)^*. \tag{4.2}$$

These coefficients can be calculated for a given particle shape using Monte Carlo integration. Since $E(\Omega)$ is real, $E^{l\,*}_{mn} = (-1)^{m-n}\, E^l_{-m-n}$. Also, since the excluded volume is symmetric under particle exchange, i.e., $E(\Omega) = E(\Omega^{-1})$, we find that $E^{l\,*}_{mn} = E^l_{nm}$.

For the orientation distribution function $\psi(\Omega)$ we expand

$$\psi(\Omega) = \sum_{l=0}^{\infty} \frac{2l+1}{8\pi^2} \sum_{m,n=-l}^{l} \langle \mathcal{D}^l_{mn} \rangle^* \mathcal{D}^l_{mn}(\Omega), \tag{4.3}$$

where the coefficients $\langle \mathcal{D}^l_{mn} \rangle$ are order parameters, since they are given by

$$\langle \mathcal{D}^l_{mn} \rangle = \int d\Omega\, \mathcal{D}^l_{mn}(\Omega) \psi(\Omega). \tag{4.4}$$

We can also choose to expand the logarithm of the orientation distribution function as

$$\psi(\Omega) = \frac{1}{Z} \exp\left[\sum_{l=0}^{\infty} \sum_{m,n=-l}^{l} \psi^l_{mn} \mathcal{D}^l_{mn}(\Omega) \right], \tag{4.5}$$

with the normalization of $\psi(\Omega)$ assured by the factor

$$Z = \int d\Omega\, \exp\left[\sum_{l=0}^{\infty} \sum_{m,n=-l}^{l} \psi^l_{mn} \mathcal{D}^l_{mn}(\Omega) \right]. \tag{4.6}$$

Here we prefer the expansion Eq. (4.5), since the coefficients ψ^l_{mn} are unbounded and this expansion is expected to converge faster than Eq. (4.3) [100]. The Euler-Lagrange equation [Eq. (1.18)] for the second-virial theory is then

$$\psi^l_{mn} = -\rho\, G(\eta) \sum_{p=-l}^{l} E^l_{pn} \langle \mathcal{D}^l_{mp} \rangle^*, \tag{4.7}$$

where we use Parsons-Lee second-virial theory by taking $B_2 \to G(\eta)B_2$ in Eq. (1.10), with $G(\eta)$ the Parsons-Lee prefactor [Eq. (C.4)]. This prefactor approximately includes higher order virial terms, making second-virial theory more quantitatively accurate for moderate aspect ratio rods. For rigid boomerangs, Parsons-Lee second-virial theory gave reasonable agreement with the equation of state found from Monte Carlo simulations [81]. Equation (4.7) together with Eq. (4.4) can be solved for the set of coefficients ψ^l_{mn}, where the expansion in Eq. (4.5) is truncated at some $l = l_{\max}$. Based on the particle and phase symmetries, the number of ψ^l_{mn} coefficients can be reduced [51] and in addition, since $\psi(\Omega)$ is real we find that $\psi^l_{mn} = (-1)^{m-n}\psi^l_{-m-n}$. Here we focus on the coefficients with $l \leq 2$, which are the most important ones close to the isotropic-nematic transition. Of course, at higher densities we expect this approximation to be quantitatively inaccurate and the higher order l coefficients to become important.

Following the convention of Ref. [94], we define four order parameters [which are equivalent to Eqs. (3.16)-(3.19)] as

$$S = \langle \mathcal{D}^2_{00} \rangle, \tag{4.8}$$

$$U = \sqrt{2}\,\mathrm{Re}\langle \mathcal{D}^2_{0\pm 2} \rangle, \tag{4.9}$$

$$P = \sqrt{2}\,\mathrm{Re}\langle \mathcal{D}^2_{\pm 20} \rangle, \tag{4.10}$$

$$F = \mathrm{Re}\left[\langle \mathcal{D}^2_{22} \rangle + \langle \mathcal{D}^2_{-22} \rangle \right], \tag{4.11}$$

all of which are zero in the isotropic phase (I). In a uniaxial phase, the order parameters S and U are nonzero and $P = 0 = F$, with $S < 0$ corresponding to an oblate nematic N_-, and $S > 0$ corresponding to a prolate nematic N_+. In a biaxial nematic, all four of these order parameters are nonzero. In addition, we define the packing fraction $\eta = \rho v_0$, where the single-particle volume v_0 is determined using Monte Carlo integration.

4.3. Smectic bifurcation

We now examine the limits of the stability of the nematic phases of boomerangs with respect to smectic fluctuations using a bifurcation analysis [12–14, 51]. A bifurcation analysis is simply studying what new solutions $\rho_1(\mathbf{r}, \Omega)$ to the Euler-Lagrange equation Eq. (1.7) branch off from a known solution $\rho_0(\mathbf{r}, \Omega)$, and finding the bifurcation density at which this occurs. This is done by inserting $\rho(\mathbf{r}, \Omega) = \rho_0(\mathbf{r}, \Omega) + \varepsilon\rho_1(\mathbf{r}, \Omega)$ with $\varepsilon \ll 1$ into the Euler-Lagrange

equation Eq. (1.7) and solving the equation of order ε.[1] If we take a nematic distribution as our reference, then $\rho_0(\mathbf{r},\Omega) = \rho\,\psi_0(\Omega)$, where at average density ρ, $\psi_0(\Omega)$ is a solution of Eq. (1.18). Furthermore on the basis of the translational invariance of the nematic phase, it can be shown that the solutions are of the periodic form $\rho_1(\mathbf{r},\Omega) \propto \rho\,\psi_1(\Omega)\cos(\mathbf{q}\cdot\mathbf{r})$, for arbitrary $\mathbf{q}$. This leads to the following eigenvalue equation [12, 14–16]

$$\psi_1(\Omega_1) = \rho\,G(\eta)\,\psi_0(\Omega_1)\int d\Omega_2\,\hat{f}(\mathbf{q};\Omega_{12})\,\psi_1(\Omega_2), \tag{4.12}$$

where the Fourier transform of the Mayer function is

$$\hat{f}(\mathbf{q};\Omega_{12}) = \int d\mathbf{r}\,f(\mathbf{r};\Omega_{12})\cos(\mathbf{q}\cdot\mathbf{r}), \tag{4.13}$$

and where for hard particles the Mayer function is given by Eq. (1.16). We must find the smallest density $\rho = \rho^*$ (note that $\psi_0(\Omega)$ implicitly depends on ρ) where Eq. (4.12) has a non-trivial solution $\psi_1(\Omega)$ for some $\mathbf{q}^* \neq 0$.

To simplify the problem, we can make a decoupling approximation, that is, $\psi_1(\Omega) = \psi_0(\Omega)$ [15]. Using this and integrating over both sides in Eq. (4.12), the bifurcation equation becomes

$$1 = \rho\,G(\eta)\int d\Omega_1\int d\Omega_2\,\hat{f}(\mathbf{q};\Omega_{12})\psi_0(\Omega_1)\psi_0(\Omega_2). \tag{4.14}$$

We note that while using the expansion Eq. (4.3) with equilibrium coefficients $\langle\mathcal{D}^l_{mn}\rangle$ resulting from solving Eq. (4.7) leads to an algebraic equation as a result of the orthogonality of the $\mathcal{D}^l_{mn}$, this expansion is extremely bad at characterizing very ordered nematic phases if it is truncated at low l. Therefore we use Eq. (4.5) with the equilibrium ψ^l_{mn} for $\psi_0(\Omega)$ when solving Eq. (4.14), and evaluate the integrals on the right-hand side using Monte Carlo integration for various wavevectors $\mathbf{q}$ and various densities ρ. We then determine the smallest $\rho = \rho^*$ which satisfies Eq. (4.14). For smectic A phases, the wavevector $\mathbf{q}$ is parallel to the nematic director $\hat{n}$ which we use as our coordinate frame's $\hat{z}$ axis. Here we only consider $\mathbf{q} = q\hat{z}$, $q\hat{y}$, $q\hat{x}$, though in principle other $\mathbf{q}$ should be considered if tilted smectics or columnar phases are expected. The bifurcating wavenumber q is $q = q^*$ and this is related to the layer spacing by $d^* = 2\pi/q^*$.

[1] Note that we use Parsons-Lee second-virial theory in this chapter, in which $G(\eta)$ appears in the exponents of Eqs. (1.7) and (1.18).

This decoupling approximation amounts to neglecting coupling between orientational and positional order. As this restricts the bifurcation orientation distribution functions to a smaller set, we expect this to shift the bifurcation point to higher densities. Though we may not find quantitatively accurate results with this additional approximation, we may still be able to make conclusions about the the nematic-smectic transition as a function of interarm angle and aspect ratio. We note that this approximation is likely worse for studying short particles as was shown for rods [16]. In addition, we expect this to be worse at estimating the bifurcation densities for nematic to polar smectic phases, as these clearly exhibit orientational and positional coupling.

4.4. Results

First, we consider the spatially homogeneous phases of boomerangs with $L = 10D$ and various interarm angles χ. For each boomerang shape, we compute the excluded volume coefficients [Eq. (4.2)] using Monte Carlo integration with 10^{11} Monte Carlo steps. We then solve the Euler-Lagrange equation [Eq. (4.7)] for the equilibrium coefficients ψ^l_{mn} up to $l_{\max} = 2$ for various packing fractions. In Fig. 4.2, we show the resulting equilibrium order parameters as a function of packing fraction, for various interarm angles χ. For small opening angles of $\chi = 40°$ [Fig. 4.2(a)], we find a transition from an isotropic to prolate nematic (with boomerangs aligned along their $\hat{u}$ axes) at $\eta \approx 0.26$, followed by a transition to a biaxial nematic at $\eta \approx 0.4$. For $\chi = 90°$ [Fig. 4.2(b)], we find an isotropic to oblate nematic (with boomerangs' $\hat{u}$ and $\hat{v}$ axes aligned in plane perpendicular to the nematic director $\hat{n}$) to biaxial nematic sequence. There is an approximately direct isotropic to biaxial nematic sequence at $\chi = 105°$ [Fig. 4.2(c)]. For even larger opening angles ($\chi = 120°$), we find again a transition from an isotropic to prolate nematic (with boomerangs aligned along their $\hat{v}$ axes) in Fig. 4.2(d). We note that sign of the biaxial order parameter F indicates a physically irrelevant switching of alignment axes.

In addition, we consider adding higher order l, however, this changes the phase behavior very little. In Fig. 4.3, we show the effect on the order parameters of adding terms up to $l_{\max} = 4$ or $l_{\max} = 6$, for two opening angles χ. We only see a small increase in the alignment of the nematic phases and no qualitative differences.

In systems of stiff flexible boomerangs (see Chapter 3), the biaxial nematic was found to be replaced by a four-fold symmetric D_4 phase around $\chi = 90°$.

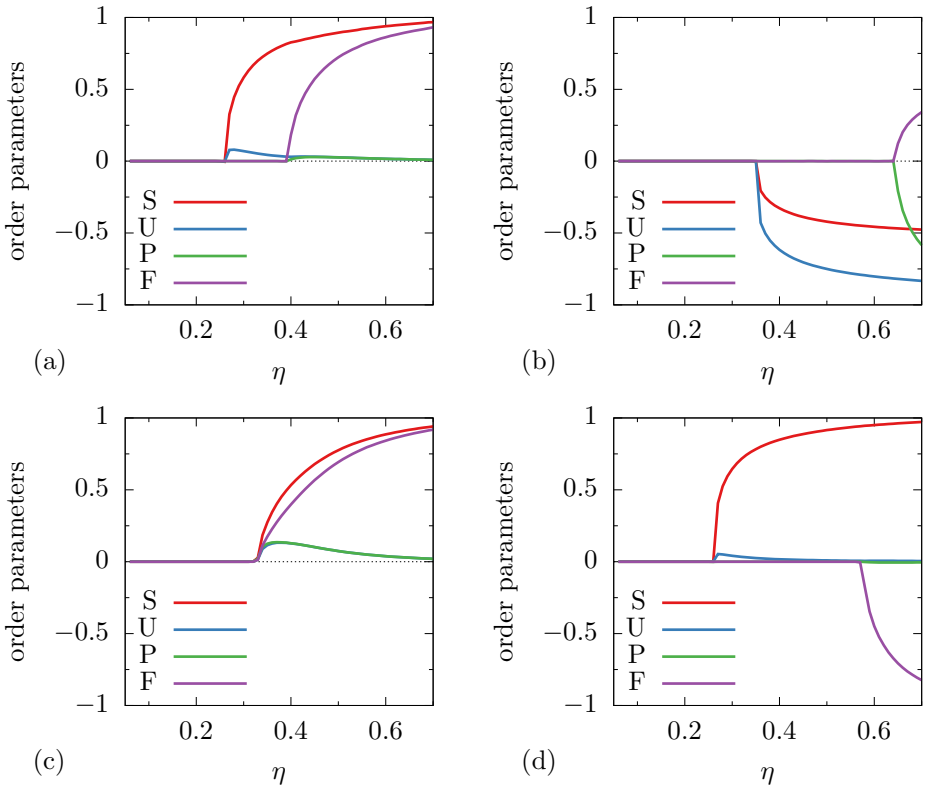

Figure 4.2.: Order parameters as a function of packing fraction η, for boomerangs with $L = 10D$ and for interarm angles (a) $\chi = 40°$, (b) $\chi = 90°$, (c) $\chi = 105°$, and (d) $\chi = 120°$.

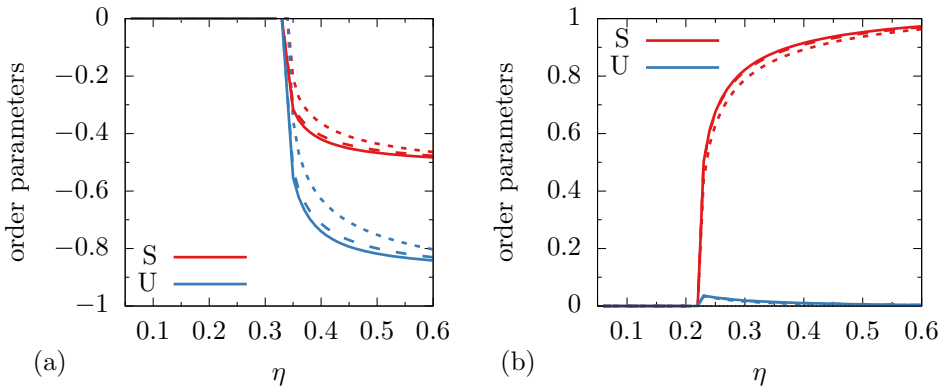

Figure 4.3.: Order parameters as a function of packing fraction η, for boomerangs with $L = 10D$ and for interarm angles (a) $\chi = 80°$, (b) $\chi = 130°$ with truncation at $l_{\max} = 2$ (dotted), $l_{\max} = 4$ (dashed), and $l_{\max} = 6$ (solid).

Such a phase would have a vanishing order parameter F [Eq. (4.11)] but nonzero order parameters $\langle \mathcal{D}^4_{44} \rangle$ and $\langle \mathcal{D}^4_{-44} \rangle$. For several angles at and around $\chi = 90°$ we repeated our calculations with $l_{\max} = 4$, however, such a phase was never found to be stable. We believe this can be explained by comparing the segmentwise excluded volume [Eq. (3.4)] to the full excluded volume. In Fig. 4.4, we plot the two-dimensional excluded volume (excluded area) for $\chi = 90°$ as a function of relative orientation α, which is equivalent to two boomerangs lying with their arms within a single plane, such that we can use the analytical result from Ref. [93]. Here we see that while within the segmentwise approximation $E(0) = E(\pi/2) = E(\pi)$ is minimal, the exact excluded volume is only minimized by the antiparallel configuration ($\alpha = \pi$).

Though we allowed for ψ^l_{mn} with odd l, m, and n in our calculations, since the boomerangs have a polar shape, a polar phase never was found to be favorable. This is to be expected in light of results showing that the excluded volume of two antiparallel boomerangs is half that of two parallel ones [93], shown in Fig. 4.4 for $\chi = 90°$ in two dimensions. Of course, in the case of spatially inhomogeneous phases such as smectics or spatially modulated phases such as twist-bend nematics, a polar configuration may be preferable.

We use the order parameters and free energies to build a phase diagram in the interarm angle χ and packing fraction η plane for boomerangs with $L = 10D$ for $l_{\max} = 2$. By a common tangent construction or equivalently setting the pressure and chemical potentials of the isotropic and nematic phases equal, we solve for the isotropic and nematic coexistence densities.

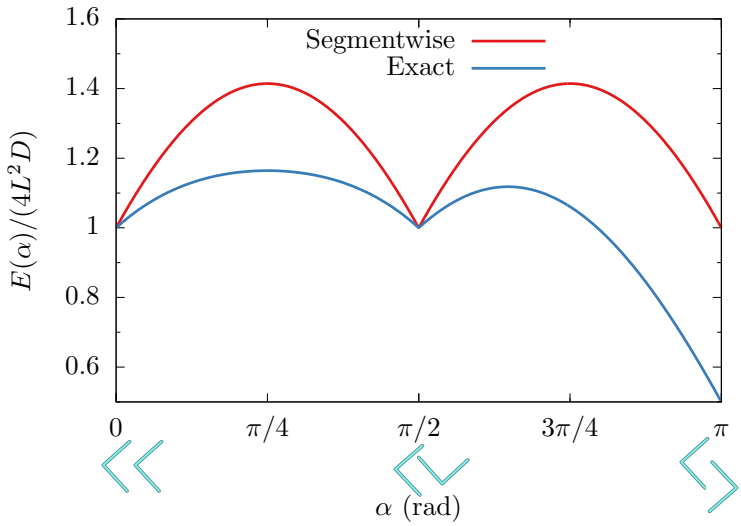

Figure 4.4.: Dimensionless excluded volume as a function of relative orientation α for two boomerangs with $\chi = 90°$ in two dimensions, within the segmentwise approximation [Eq. (3.4)] and the exact results from Ref. [93]. Illustrations along the horizontal axis show relative particle orientations.

In Fig. 4.5, we show the resulting phase diagram. We find an isotropic (I) phase at low packing fractions, and for rodlike boomerangs with $\chi > 105°$ or $\chi < 52.5°$, we find an isotropic to prolate nematic (N_+) transition with increasing packing fraction. For interarm angles of $52.5° < \chi < 105°$, there is an isotropic-oblate nematic (N_-) transition. Separating the oblate from prolate ordering we find a direct isotropic to biaxial nematic phase at $\chi \approx 52.5°$ and $\chi \approx 105°$, the latter of which is in good agreement with Ref. [79] (which studied the range $\chi > 90°$ and found a Landau point at $\chi = 107.36°$). Close to the four-phase Landau points, the isotropic-nematic transition becomes weakly first order.

To calculate the integrals in the smectic bifurcation equation [Eq. (4.14)] for various packing fractions η and wavenumbers q, we use Monte Carlo integration with 10^{11} Monte Carlo steps. We calculate the uncertainty by calculating the standard error in the bifurcation densities obtained using five independent subsets of the Monte Carlo data. For $L = 10D$, the uncertainty in the bifurcation density was less than one percent. The solid curve in Fig. 4.5 shows the resulting smallest η^* with a nontrivial solution for $\mathbf{q} = q\hat{z}$, $q\hat{y}$, $q\hat{x}$, where the nematic director is parallel to $\hat{z}$ (and for the biaxial nematic

the other directors are parallel to $\hat{x}$ and $\hat{y}$). We see that the region of stability of the prolate nematic phases is decreased for the intermediate values of χ with respect to straight rods with $\chi = 0°$ or $\chi = 180°$.

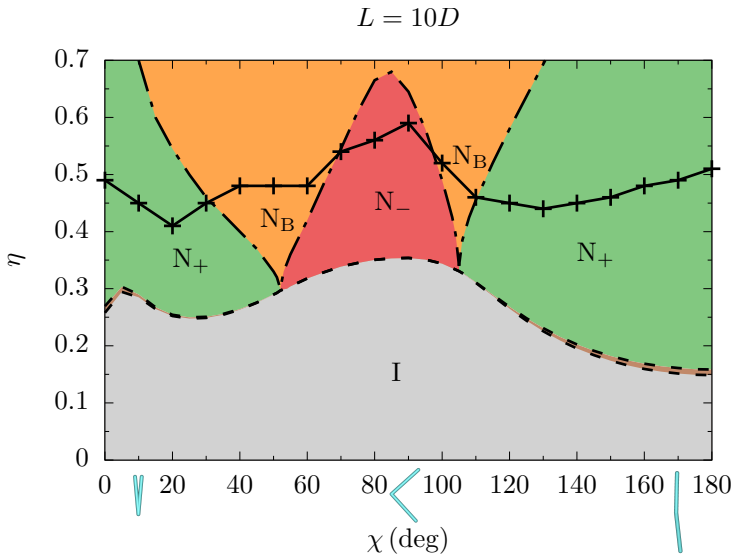

Figure 4.5.: Phase diagram for boomerangs with equal length arms ($L = 10D$) as a function of the angle χ and the packing fraction η. At low packing fraction, an isotropic phase (I) is found, while at higher packing fractions oblate (N_-), prolate (N_+), and biaxial (N_B) nematic phases are found, with two Landau points at $\chi \approx 52.5°$ and $\chi \approx 105°$. The brown region between the dashed curves is the isotropic-nematic coexistence region and the black solid curve corresponds to the nematic-smectic bifurcation packing fraction.

In Fig. 4.6, we show the smectic layer spacing $d^* = 2\pi/q^*$ for the nematic-smectic bifurcation. For smectics bifurcating from prolate nematics, we find that $\mathbf{q} = q\hat{z}$, i.e., the bifurcating wavevector is parallel to the the nematic director (smectic A). We see that as the interarm angle χ decreases from $\chi = 180°$, the layer spacing decreases since the effective length of the particle decreases. For $\chi \approx 80°$, the bifurcating smectic is perpendicular to the nematic director of the oblate nematic, with a layer spacing $d^* \approx L$.

In Fig. 4.7, we show phase behavior of boomerangs with interarm angle $\chi = 130°$ in the arm aspect ratio L/D, packing fraction η plane. Similarly to the case of spherocylinders, the isotropic-nematic packing fraction decreases with aspect ratio. In contrast with the case of straight spherocylinders

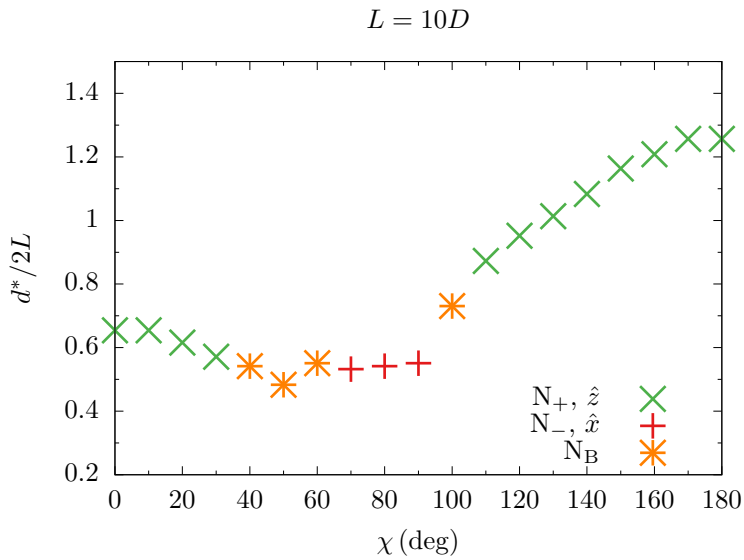

Figure 4.6.: Smectic layer spacing d^* divided by the total boomerang contour length $2L$ as a function of interarm angle χ.

which have almost no change in smectic density for total aspect ratios $L/D \gtrsim 10$ [4, 15], we find that for boomerangs with $\chi = 130°$ the smectic bifurcation density decreases with packing fraction. We limit the aspect ratios considered here to $L \leq 40D$, as the number of necessary Monte Carlo steps increases with aspect ratio. The uncertainty on this calculation was less than five percent for aspect ratios $L \approx 30D$ and less than seven percent for $L \approx 40D$.

4.5. Conclusions

In this chapter, we studied the phase behavior of boomerangs with opening angles $0° \leq \chi \leq 180°$. We used Monte Carlo integration to calculate the excluded volume coefficients, and so went beyond the segmentwise approximation used in Chapter 3. We found two Landau points with direct isotropic-biaxial nematic transitions, separating the prolate and oblate ordering. This was in good agreement with the rigid boomerang results from Ref. [79] for $\chi > 90°$. However, the oblate and biaxial nematic phases have thus far never been observed in computer simulations. Since the simulations

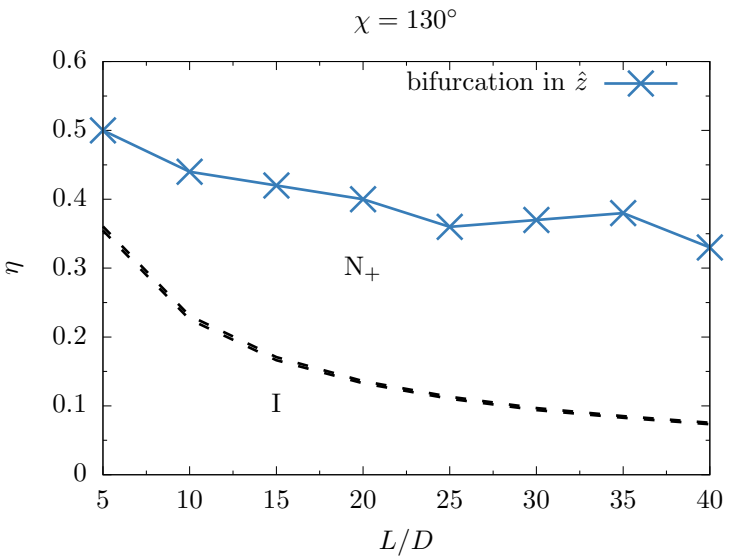

Figure 4.7.: Smectic bifurcation packing fraction η^* (blue) and the isotropic-nematic coexistence packing fractions (black, dashed) for boomerangs with interarm angle $\chi = 130°$ as a function of arm length L/D.

in Ref. [82] were restricted to relatively short arm lengths ($L/D = 5$), it is perhaps unsurprising that the smectics preempt the nematic phases for $\chi < 135°$ since the effective particle aspect ratio is reduced. Our nematic-smectic bifurcation showed that the smectics can somewhat reduce the range of stability of the nematics, but did not find that it preempted them entirely. Surprisingly, we found that the nematic-smectic bifurcation density decreased with aspect ratio for $\chi = 130°$, which may show that higher aspect ratios do not necessarily provide larger regions of stability for nematics of boomerangs, unlike the case of straight spherocylinders.

The major shortcoming of our bifurcation analysis is that we used a decoupled approximation for the nematic-smectic bifurcation, which neglects translational and orientational coupling. This likely overestimates the bifurcation density as discussed above. In addition, the simulations in Ref. [82] found a polar smectic formed for $\chi \lesssim 167°$, and so most likely the translational and orientational coupling cannot be neglected in this regime. The full nematic-smectic bifurcation is therefore an interesting future step. As colloidal boomerangs can now be synthesized in the lab [85, 86, 101] and increasing computation power allows for the simulations of longer boomerangs,

we expect the issue of the (non-)existence of the oblate and biaxial nematic phases to be settled in the coming years.

Acknowledgments

We thank Simone Dussi for his help on the Monte Carlo integration of the virial coefficients. We also thank Massimiliano Chiappini and Marjolein Dijkstra for useful discussions.

Chapter 5.

Cuboids

5.1. Introduction

There has long been interest in the biaxial nematic N_B phase, which exhibits two optical axes in contrast to the ordinary uniaxial nematic phase that displays only a single optical axis. Biaxial nematic phases have long held promise for applications in novel opto-electronic devices, but their limited window of thermodynamic stability is of great concern. In fact, even though the theoretical prediction of the existence of the N_B phase goes back to the 1970's [68, 69], and first claims of its experimental observation in a micellar system date back to 1980 [102], the existence of a stable N_B phase in thermotropic systems is still the subject of much debate [67]. In 2004, novel experiments on different molecular thermotropic systems again claimed to observe the N_B [103–106], which in the meantime was also observed in computer simulations of attractive particles [107, 108]. More recently, an N_B phase was observed in colloidal dispersions of purely repulsive board-like particles in 2009 [109], where the stability was argued to stem from polydispersity that prevents the system from forming a smectic phase [110]. This finding in an entropy-dominated system appears to be consistent with the observation of a stable N_B phase in early simulations of hard biaxial ellipsoids [70, 71], which do not exhibit a smectic phase either [111]. Interestingly, however, recent simulations of hard spheroplatelets (with a stable smectic phase in their phase diagram) also revealed a stable N_B phase [72], whereas ostensibly similarly shaped cuboidal particles do not [112]. On top of this confusing situation comes an unsettled issue regarding the topology of the phase diagram, in particular whether a prolate (N_+) or oblate (N_-) uniaxial nematic phase intervenes the isotropic (I) and N_B phase or whether a direct I-N_B phase transition is possible. According to early theoretical studies the density-shape representation of the phase diagram exhibits a cusp-like feature

where a rod-like regime with I-N_+ coexistence and a plate-like regime with I-N_- coexistence merge at the so-called dual shape into a single multi-critical point with a direct I-N_B phase transition, as shown in Fig. 5.1(a) [51, 113]. More recent Landau-type theories, however, also allow for other scenarios either with or without a direct I-N_B transition [see Fig. 5.1(b)] [67, 114–116].

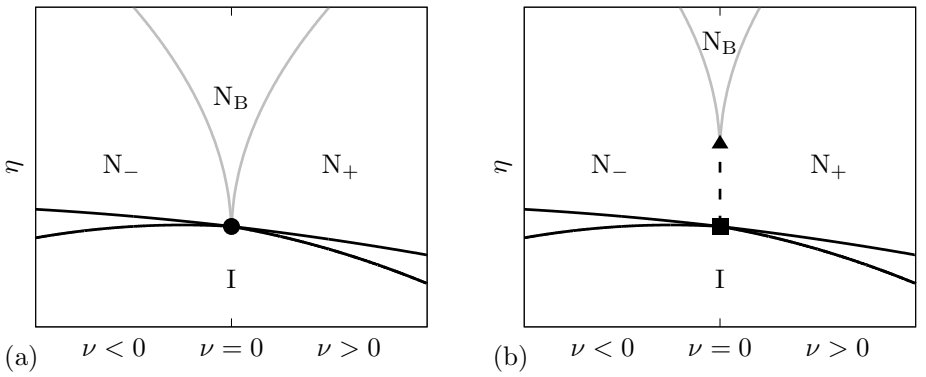

Figure 5.1.: Possible cuboid phase diagram topologies in the shape parameter ν, packing fraction η plane. Within second-virial theory, the dual-shape $\nu = 0$ separates the rod-like ordering (N_+) from the plate-like ordering (N_-), with the isotropic (I) to nematic transition becoming weakly ordered approaching $\nu = 0$, with the black solid lines giving the coexisting isotropic and nematic phases. In (a), there is a direct isotropic to biaxial nematic (N_B) phase transition at $\nu = 0$ with the circle representing the four-phase Landau point, whereas in (b) there is an intermediate uniaxial nematic phase along the dashed line, with three-phase points indicated by the square and triangle.

A recent work [74] used Monte Carlo and Event-Driven Molecular Dynamics simulations to settle the issue of the existence and stability of the biaxial nematic phase in entropy-driven systems by performing computer simulations of hard biaxial cuboids, triangular prisms, and rhombic platelets. These shapes can be characterized by long (L), medium (M), and short (S) particle axes that give rise to the dimensionless particle length $L^* \equiv L/S$ and particle width $M^* \equiv M/S$. As earlier predicted [51], a biaxial nematic phase was indeed found close to the so-called dual shape, for which the shape parameter $\nu = L/M - M/S$ is zero. The N_B phase, however, was only found to be stable if the particle anisotropy exceeds a critical value L^*_{min}, which, surprisingly, varies significantly between the different particle families. For cuboids the necessary anisotropy was found to be $L^* > 23$ [74], whereas for

dual-shaped spheroplatelets that closely resemble the cuboids at first sight, recent simulations [72, 73] revealed an N_B phase for $L^* > 9$. For the rhombi and two types of triangular prisms, a minimal anisotropy of $L^*_{\text{min}} = 9, 11, 14$, respectively, was needed [74]. This trend in which particle shapes with triangular, rounded, or rhombic cross-sections have smaller L^*_{min} than cuboids suggests that the 2D packing efficiency of the particle cross-section in a smectic layer largely determines L^*_{min} [112, 113, 117, 118].

Surprisingly, Ref. [74] found that strong competition with the N_B phase comes not only from the smectic phase at high densities, but also from the uniaxial nematic phases at relatively low densities, such that a direct I-N_B phase transition does not exist due to an intervening uniaxial nematic phase. For the cuboids, the intervening uniaxial phase was found to be oblate at and around the dual shape [74].

In this chapter, we apply density functional theory to systems of hard cuboids to investigate both the lack of a direct I-N_B transition and the reason why the intervening uniaxial nematic phase is oblate. The cuboid particle model and schematic illustrations of the nematic phases are shown in Fig. 5.2. We employ both a discrete orientation Zwanzig model and a continuous orientation model where angular dependencies are expanded in Wigner matrices. In order to break the symmetry between prolate shapes with $\nu > 0$ and oblate shapes with $\nu < 0$, one must go beyond second virial theory. Therefore we study both of these density functional theories at both the second- and third-virial level. Surprisingly, we find that even at the second-virial level, there is no direct I-N_B transition unless the particles are very short. Within third-virial theory, the Zwanzig model gives that the prolate nematic phase is favored at the dual shape, whereas the continuous model finds the oblate is preferred, in agreement with the simulations of Ref. [74].

In the Sec. 5.2, we describe the two models used here, namely the Zwanzig model in Sec. 5.2.1 and the continuous orientation model in Sec. 5.2.2. We then present our results in Sec. 5.3 and conclude in Sec. 5.4.

5.2. Method

5.2.1. Zwanzig model

First we consider the Zwanzig model, where we approximate the orientation distribution function of the six discrete, orthogonal orientations as $\psi(\Omega) = \psi_i$

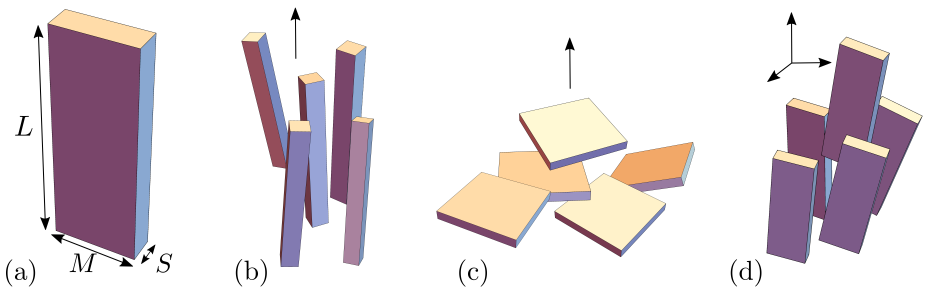

Figure 5.2.: (a) A cuboid with particle dimensions L, M, and S. Illustrations of the (b) N_+, (c) N_-, and (d) N_B phases, with arrows indicating nematic directors.

with $i = 1, \ldots, 6$. Following Ref. [110], we can define the orientation vectors

$$\begin{aligned} \mathbf{X} &= (L, M, S, L, M, S), \\ \mathbf{Y} &= (M, S, L, S, L, M), \\ \mathbf{Z} &= (S, L, M, M, S, L), \end{aligned} \tag{5.1}$$

such that the dimensions of a particle with orientation i in the $\hat{x}, \hat{y}, \hat{z}$ directions are X_i, Y_i, Z_i, respectively (see Fig. 5.3 for an illustration of the allowed six orientations). Now, the excluded volume [Eq. (1.12)] of two particles with orientations i and j is simply given by [110]

$$E_{ij} = (X_i + X_j)(Y_i + Y_j)(Z_i + Z_j). \tag{5.2}$$

Similarly, we can write the three-particle excluded volume [Eq. (1.14)] for the Zwanzig model as

$$\begin{aligned} \hat{E}_{ijk} =& (X_iX_j + X_jX_k + X_iX_k) \\ & \times (Y_iY_j + Y_jY_k + Y_iY_k)(Z_iZ_j + Z_jZ_k + Z_iZ_k). \end{aligned} \tag{5.3}$$

For a full derivation of Eqs. (5.2)-(5.3), see the Appendix of this chapter. Then the free energy [Eq. (1.10) with appropriate replacements of $\int d\Omega \to \sum_{i=1}^{6}$]

is

$$\frac{\beta F(\psi_i)}{V} = \rho(\ln \mathcal{V}\rho - 1) + \rho \sum_{i=1}^{6} \psi_i \ln \psi_i + \frac{\rho^2}{2} \sum_{i,j=1}^{6} E_{ij}\psi_i\psi_j + \frac{\rho^3}{6} \sum_{i,j,k=1}^{6} \hat{E}_{ijk}\psi_i\psi_j\psi_k, \tag{5.4}$$

Using Eqs. (5.1)-(5.3), and minimizing the free energy [Eq. (5.4)] with respect to ψ_i at fixed ρ with the normalization condition $\sum_{i=1}^{6} \psi_i = 1$ gives the Euler-Lagrange equation

$$\psi_i = \frac{1}{Z} \exp\left(-\rho \sum_{j=1}^{6} E_{ij}\psi_j - \frac{\rho^2}{2} \sum_{j,k=1}^{6} \hat{E}_{ijk}\psi_j\psi_k \right), \tag{5.5}$$

with $Z = \sum_{i=1}^{6} \exp\left(-\rho \sum_{j=1}^{6} E_{ij}\psi_j - \frac{\rho^2}{2} \sum_{j,k=1}^{6} \hat{E}_{ijk}\psi_j\psi_k\right)$ ensuring the normalization of ψ_i.

For given coefficients E_{ij} and $\hat{E}_{ijk}$, and for a given density ρ, Eq. (5.5) can be solved iteratively for the equilibrium distribution ψ_i^{eq}. Note that the second-virial approximation is obtained by setting $\hat{E}_{ijk} = 0$ in Eq. (5.5). Then, ψ_i^{eq} can be used to identify the phase and to obtain the equilibrium free energy.

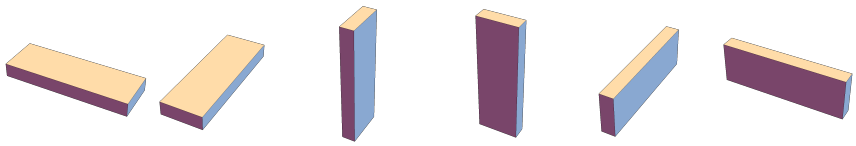

Figure 5.3.: The six orthogonal orientations considered in the Zwanzig model.

5.2.2. Expansion in Wigner matrices

In our second model, the orientations are continuous rather than discrete and we expand all Euler angle dependencies in a complete basis of Wigner matrices $\mathcal{D}^l_{mn}(\Omega)$ (see Appendix B). Within a second-virial theory, this gives the same expansions as in Chapter 4, with Eq. (4.1) giving the expansion

for the excluded volume with expansion coefficients E^l_{mn}. We note that for hard cuboids, an analytic expression for $E(\Omega)$ is known [11], which we write explicitly as a function of the three Euler angles Ω in the Appendix of this chapter.

We expand $\psi(\Omega)$ in Wigner matrices [Eq. (4.3)] with the order parameters $\langle \mathcal{D}^l_{mn} \rangle$ being the coefficients of the expansion. In addition, we expand the logarithm of the orientation distribution function [Eqs. (4.5)-(4.6)] with coefficients ψ^l_{mn}. We prefer the latter [Eq. (4.5)], since the coefficients ψ^l_{mn} are unbounded and this expansion is expected to converge faster than Eq. (4.3) [100].

For the continuous-orientation model within a third-virial theory, we also expand

$$\hat{E}(\Omega_{12}, \Omega_{13}) = \sum_{l,m,n} \sum_{l',m',n'} \hat{E}^{ll'}_{mm'nn'} \mathcal{D}^l_{mn}(\Omega_{12}) \mathcal{D}^{l'}_{m'n'}(\Omega_{13}), \tag{5.6}$$

where for brevity we write $\sum_{lmn} = \sum_{l=0}^{\infty} \sum_{m,n=-l}^{l}$, and where the coefficients are

$$\hat{E}^{ll'}_{mm'nn'} = \frac{2l+1}{8\pi^2} \frac{2l'+1}{8\pi^2} \int d\Omega_{12} \int d\Omega_{13} \hat{E}(\Omega_{12}, \Omega_{13}) \times \mathcal{D}^l_{mn}(\Omega_{12})^* \mathcal{D}^{l'}_{m'n'}(\Omega_{13})^*. \tag{5.7}$$

For a specific particle shape, we calculate $\hat{E}^{ll'}_{mm'nn'}$ using Monte Carlo integration, with either 100 or 200 independent runs of with 10^{10} MC steps [29, 65].

The third-virial Euler-Lagrange equation is

$$\psi^l_{mn} = -\rho \sum_{p=-l}^{l} E^l_{pn} \langle \mathcal{D}^l_{mp} \rangle^* - \frac{\rho^2}{2} \sum_{\tilde{l}\tilde{m}\tilde{n}\tilde{p}} \sum_{l'm'n'p'} \hat{E}^{\tilde{l}l'}_{\tilde{m}m'\tilde{n}n'} \times C(\tilde{l}, \tilde{p}; l', p'; l, m)\, C(\tilde{l}, \tilde{n}; l', n'; l, n)\, \langle \mathcal{D}^{\tilde{l}}_{\tilde{p}\tilde{m}} \rangle^* \langle \mathcal{D}^{l'}_{p'm'} \rangle^*, \tag{5.8}$$

where C is the Clebsch-Gordan coefficient that arises from integrals over three Wigner matrices [see Eq. (B.15)]. Note that the second-virial approximation is obtained by setting $\hat{E}^{ll'}_{mm'nn'} = 0$. Equation (5.8) together with Eq. (4.4) can be solved for the set of coefficients ψ^l_{mn}, where the expansion in Eq. (4.5) is truncated at some $l = l_{\max}$. Based on the particle and phase symmetries, the number of ψ^l_{mn} coefficients can be reduced to those with even l, m, n [51] and in addition, since $\psi(\Omega)$ is real we find that $\psi^l_{mn} = (-1)^{m-n} \psi^l_{-m-n}$. Here

we focus on the coefficients with $l = 2$, which are the only ones required by symmetry [51] and also the most important ones close to the dual shape where the isotropic-nematic transition is expected to be weakly first order. Of course, at higher densities we expect this approximation to be quantitatively inaccurate and the higher order (even) l coefficients to become important.

Once the second or third-virial Euler-Lagrange equation is solved for the equilibrium $\{\psi^l_{mn}\}$, these can be used to obtain the order parameters [Eq. (4.4)] and the free energy [Eq. (1.10)]. Following the convention of Ref. [94], we define four order parameters S, U, P, and F [Eqs. (4.8)-(4.11)], all of which are zero in the isotropic phase. In a uniaxial phase, the order parameters S and U are nonzero and $P = 0 = F$, with $S < 0$ corresponding to an oblate nematic N_-, and $S > 0$ corresponding to a prolate nematic N_+. In a biaxial nematic, all four of these order parameters are nonzero. In addition, we define the packing fraction $\eta = \rho v_0$, where the single-particle volume $v_0 = LMS$.

5.3. Results

We first present the results for the Zwanzig model described in Sec. 5.2.1. In Fig. 5.4, we show phase diagrams in the length L^*, packing fraction η plane, for dual-shaped cuboids with $L^* = M^{*2}$, truncating the free energy at (a) the second-virial term and (b) the third-virial term. Contrary to Mulder's conclusion on the basis of a bifurcation analysis [51] our dual-shaped cuboids within the second-virial theory [Fig. 5.4(a)] have *no* direct I-$\mathrm{N_B}$ transition for $L^* > 11$,[1] but rather an I-$\mathrm{N_+}$/$\mathrm{N_-}$-$\mathrm{N_B}$ sequence, where the $\mathrm{N_+}$/$\mathrm{N_-}$ phases have identical free energies within the second-virial theory. However, in agreement with Ref. [110] we do find a direct I-$\mathrm{N_B}$ transition for $L^* \leq 11$. In the third-virial theory, the $\mathrm{N_+}$/$\mathrm{N_-}$ symmetry is broken in favor of $\mathrm{N_+}$ at $\nu = 0$ [Fig. 5.4(b)], in agreement with the fundamental measure theory results of Ref. [119], but not in agreement with the continuum simulations of Ref. [74], where $\mathrm{N_-}$ is favored.

Next, we consider the continuum model described in Sec. 5.2.2 with the Wigner matrix expansion truncated at $l = 2$. In Fig. 5.5, we show the free energy differences [(a),(c),(e)] between the phases and the order parameters

[1] In the range $11 < L^* \leq 13$, there is a narrow density regime where the uniaxial and biaxial nematic phases have the same free energy within our numerical accuracy. Although we will say throughout that there is an intermediate uniaxial phase when $L^* > 11$, we are not certain this phase is stable unless $L^* \geq 13$.

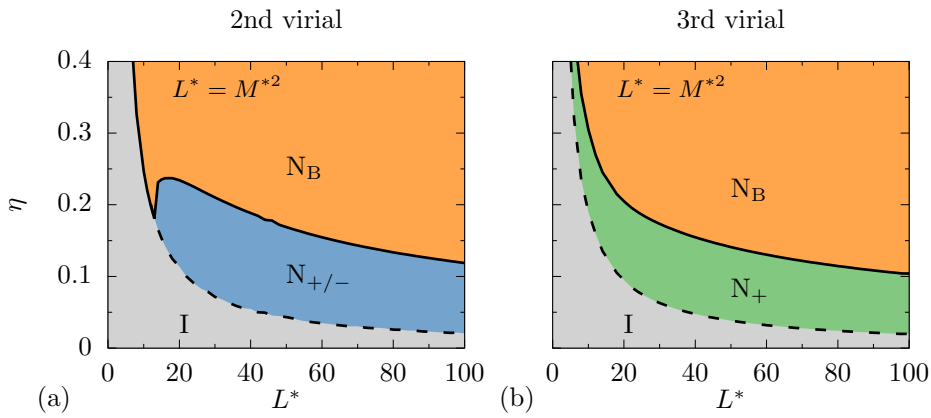

Figure 5.4.: Phase diagram for dual-shaped cuboids in the $L^* - \eta$ plane for Zwanzig model within the (a) second- and (b) third-virial theory.

[(b),(d),(f)] as a function of packing fraction η using the continuum second-virial theory for three shapes with $M^* = 8$ and (a-b) $L^* = 63$ ($\nu = -0.125$), (c-d) $L^* = 64$ ($\nu = 0$), and (e-f) $L^* = 65$ ($\nu = 0.125$). As expected, for $\nu < 0$ (a-b), we find an I-N_--N_B sequence, and for $\nu > 0$ (e-f) an I-N_+-N_B sequence. However, for $\nu = 0$ (c-d), we find that the biaxial phase has a higher free energy than the uniaxial nematic (oblate or prolate, since these have identical free energies) for a small range of packing fractions above the isotropic phase, and therefore the phase sequence is I-N_+/N_--N_B. Note that the order parameters shown in Fig. 5.5(d) are for both the biaxial nematic N_B, which is metastable in the region $0.1 \lesssim \eta \lesssim 0.17$, and for the prolate nematic N_+. We found that adding higher order l in the Wigner matrix expansion [Eq. (4.5)] slightly increased the order at a given density (see the appendix of this chapter) but otherwise had little effect on the phase behavior. We found no direct isotropic-biaxial nematic transition for $M^* = 8$, even if the Wigner matrix expansion was truncated at $l_{\max} = 4$ or $l_{\max} = 6$.

We make similar plots of the free energy differences between phases as a function of packing fraction η for our continuous-orientation third-virial theory in Fig. 5.6, for three shapes with $L^* = 36$ and for (a) $M^* = 6$ ($\nu = 0$), (b) $M^* = 4$ ($\nu = 5$), and (c) $M^* = 3$ ($\nu = 9$). Here we see that for the dual shape [Fig. 5.6(a)], the oblate nematic is always favored over the prolate. For a more rod-like cuboid [Fig. 5.6(b)], the prolate is favored at low packing fraction and the oblate at higher packing fractions. For an even more rod-like

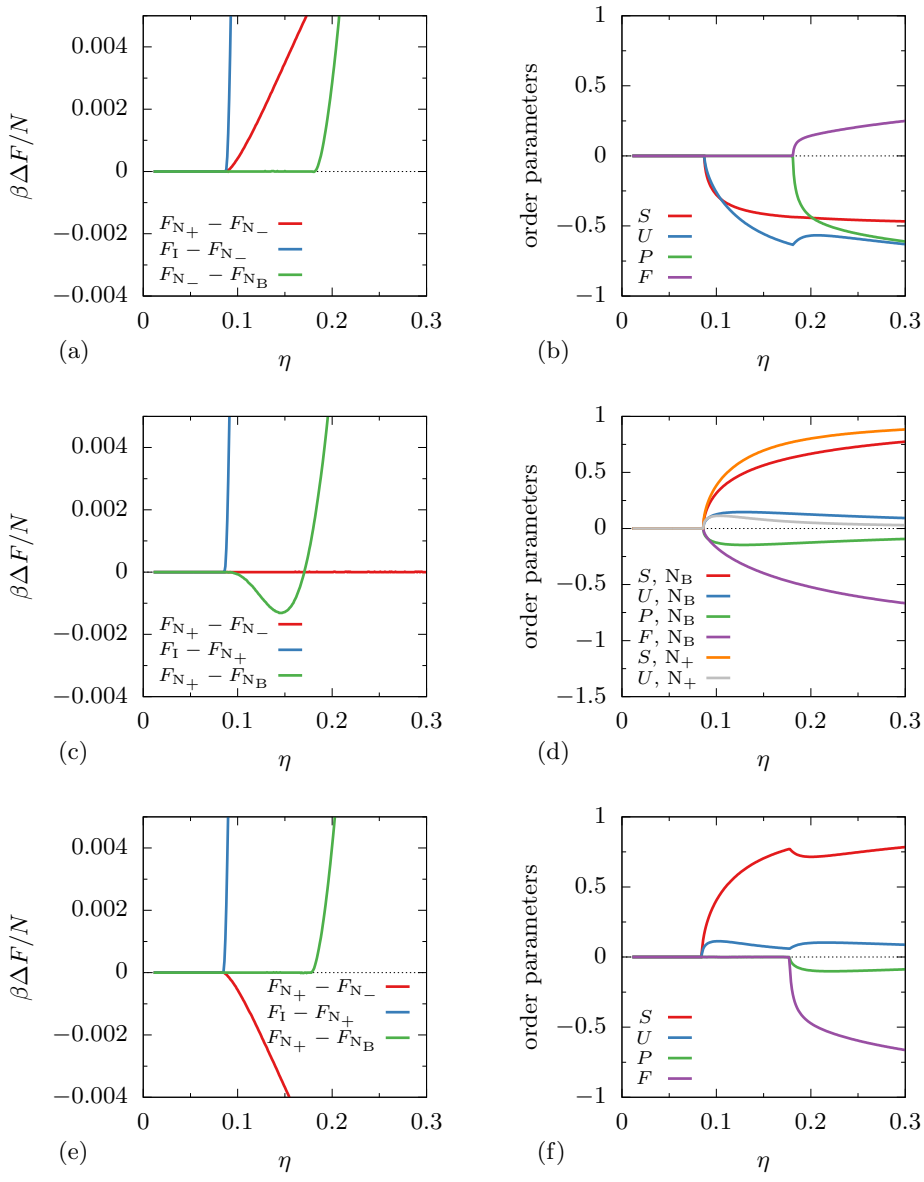

Figure 5.5.: Continuous-orientation second-virial theory results for cuboids with $M^* = 8$ and (a-b) $L^* = 63$ ($\nu = -0.125$), (c-d) $L^* = 64$ ($\nu = 0$), and (e-f) $L^* = 65$ ($\nu = 0.125$). The left column (a,c,e) shows the free energy difference ΔF between the different phases as a function of packing fraction η. The right column (b,d,f) shows the order parameters as a function of η for the (possibly metastable) biaxial phase (order parameters S, U, P, F are nonzero), oblate nematic ($P = 0 = F$, $S < 0$), or prolate nematic ($P = 0 = F$, $S > 0$).

cuboid [Fig. 5.6(c)], the prolate nematic is favored for a larger range of densities. We find that the biaxial nematic phase shifts to higher densities compared to what we found for the second-virial theory, and this phase has very small biaxial order parameters P, $F \sim 0.01$. However, we caution that at these high densities our theory is not quantitatively accurate, both because we only take the $l = 2$ term in the Wigner expansion and because higher order virial terms become necessary. Therefore we focus our attention on the uniaxial nematic behavior close to the isotropic-nematic transition. For all L^* studied, we found that at $\nu = 0$ the oblate nematic is preferred over the prolate for the continuous-orientation third-virial theory.

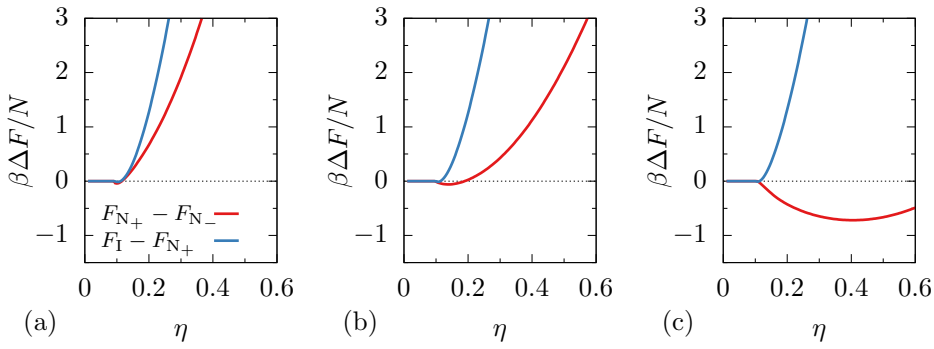

Figure 5.6.: Continuous-orientation third-virial theory results for cuboids with $L^* = 36$. The free energy difference ΔF between the different phases as a function of packing fraction η is shown for (a) $M^* = 6$ ($\nu = 0$), (b) $M^* = 4$ ($\nu = 5$), and (c) $M^* = 3$ ($\nu = 9$). Key applies to (a-c). With increasing η, we see (a) I-N$_-$, (b) I-N$_+$-N$_-$, and (c) I-N$_+$ phase sequences.

We show the second-virial phase diagram of cuboids with $M^* = 8$ in the $L^* - \eta$ representation in Fig. 5.7(a). As in the Zwanzig model (with $L^* > 11$), there is no direct isotropic to biaxial nematic phase transition. As previously discussed, at the second-virial level there is symmetry about $\nu = 0$ ($L^* = M^{*2}$), with the oblate and prolate nematic phases having identical free energy at the dual shape. Next, in the Fig. 5.7(b), we show the third-virial meta-phase diagram of phase sequences of hard cuboids in the (M^*, L^*) plane. Here we choose (somewhat arbitrarily) to label the nematic phase sequences up to $\eta = 0.4$ for long particles ($L^* \geq 50$) and up to $\eta = 0.6$ for short particles ($L^* < 50$). However, we emphasize that we have not studied the stability of the nematic phases with respect to positionally ordered phases and that we

only trust our results close to the isotropic nematic transition as discussed above. We find that adding the third-virial term to the continuum model gives a qualitative agreement with the simulations of Ref. [74], since then the phase sequence I-N$_-$-N$_\mathrm{B}$ appears for $\nu = 0$ (dashed line). Also, clearly the N$_-$ phase (red shaded area) invades the rod-like regime above the dashed line.

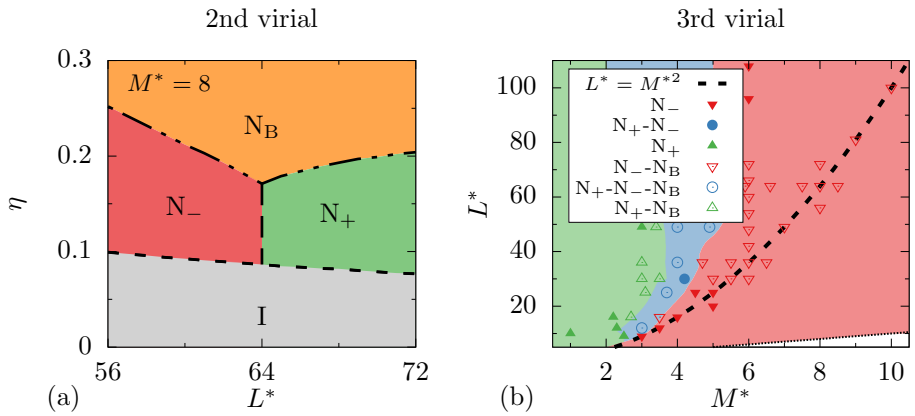

Figure 5.7.: (a) Phase diagram for $M^* = 8$ cuboids in the $L^* - \eta$ plane within the continuous-orientation second-virial theory. (b) Meta-phase diagram of cuboids in the (M^*, L^*) plane for continuum orientations within a full third-virial theory. Different symbols denote different nematic phase sequences from low to high packing fraction (up to $\eta = 0.6$ for $L^* < 50$ and up to $\eta = 0.4$ for $L^* \geq 50$), neglecting spatially ordered phases.

We also looked at the importance of the third-virial term as a function of particle aspect ratio. For spherocylinders in the isotropic phase, the ratio of the third-virial term to the second squared $B_{3,\mathrm{iso}}/B_{2,\mathrm{iso}}^2 \approx 0.3$ for short spherocylinders ($L/D = 10$) and less than 0.07 for long spherocylinders ($L/D = 100$) [8, 9]. For dual-shaped cuboids (with $L^* = M^{*2}$), the same ratio between the virial terms exceeds 0.45 for $L^* = 10$ and about 0.25 for $L^* = 100$. Clearly, for the aspect-ratios studied here the third-virial term cannot be safely neglected, and actually even the higher virial terms should have been included.

5.4. Conclusions

In conclusion, we used discrete and continuous orientation models and second- and third-virial theories to study the homogeneous liquid crystal phases of cuboids close to the so-called dual shape ($\nu = 0$). At the second-virial level, we found that as predicted, $\nu = 0$ separates the region of prolate ordering from that of oblate ordering. However, we did not find a direct isotropic to biaxial nematic transition for long cuboids ($L^* > 11$) within Zwanzig model.

To break the symmetry between N_+ and N_- phases around $\nu = 0$, we added the third-virial term to both our discrete and continuous orientation models. At the dual shape, the intervening uniaxial nematic phase between the isotropic and biaxial nematic phase was N_+ in the Zwanzig model and N_- in the continuous orientation model, the latter of which is in agreement with Monte Carlo simulations of cuboids [74].

Asymmetries in the phase diagram of ellipsoids were found from third-virial theory [120] and from simulations [121]. The simulations [121] of hard biaxial ellipsoids showed an isotropic to oblate nematic to biaxial nematic sequence with increasing density, at $\nu \approx 0$. This was already hinted at from theory [120], where it was found that the third-virial coefficient is larger for oblate ellipsoids than prolate ellipsoids, and so the oblate ellipsoids form nematic phases at lower densities than their prolate counterparts. Indeed, it is known that the third-virial term is important for thin disks ($B_3/B_2^2 \approx 0.44$ for infinitely thin disks) [122], unlike needle-like rods, where $B_3/B_2^2 \to 0$ as $L/D \to \infty$ [5]. Simulations of spheroplatelets [72, 73] also hint towards oblate ordering being more favorable at low density, since the authors find an isotropic to oblate biaxial nematic (with a small biaxial order parameter), to prolate biaxial nematic sequence with increasing density.

We have demonstrated that a continuous orientation model within a third-virial theory is required to give qualitatively accurate results for the phase behavior of hard cuboids. The fact that the discrete orientation Zwanzig model gives qualitatively inaccurate results can perhaps be understood by the fact that the fewer the allowed orientations, the larger the number of virial terms needed to obtain convergence [5, 123].

Acknowledgments

We thank Simone Dussi, Nikos Tasios, and Marjolein Dijkstra for their collaboration on biaxial nematic phases. Also, we thank Simone Dussi

for help on the Monte Carlo integration of the virial coefficients and the Zwanzig calculation. We acknowledge Bela Mulder for helpful discussions and Oleg Lavrentovich for useful comments about experiments on thermotropic systems.

Appendix

Here we calculate the second- and third-virial terms within a Zwanzig model. We also give the explicit expression for the excluded volume as a function of three Euler angles. In addition, we show results with higher order l terms in the Wigner matrix expansion within continuous second-virial theory.

Second-virial Zwanzig

We first consider the one-dimensional case of two parallel line segments with lengths X_i and X_j and with center-to-center separation of $x_{12} = x_1 - x_2$. For hard particles, the Mayer function is -1 for overlapping configurations and 0 otherwise, and so we can write it as

$$\begin{aligned} -f(x_{12}) &= \Theta\left(x_{12} - \frac{1}{2}(X_i + X_j)\right) - \Theta\left(x_{12} + \frac{1}{2}(X_i + X_j)\right) \\ &= \Pi\left(\frac{x_{12}}{X_i + X_j}\right), \end{aligned} \tag{5.9}$$

where Θ is a Heaviside step function and $\Pi(x/a)$ is a rectangular function of x centered around zero with length a. The excluded length is

$$\begin{aligned} E_{ij} &= \int_{-\infty}^{\infty} dx_{12}\, \Pi\left(\frac{x_{12}}{X_i + X_j}\right) \\ &= X_i + X_j. \end{aligned} \tag{5.10}$$

The three-dimensional case [Eq. (5.2)] is simply the product of the one-dimensional results for each direction.

Third-virial Zwanzig

For the three-particle excluded volume, we assume the parallel line segments have lengths X_i, X_j, and X_k and have positions x_1, x_2, and x_3 respectively.

The center-to-center separations are $x_{12} = x_1 - x_2$, $x_{13} = x_1 - x_3$, and $x_{23} = x_2 - x_3 = x_{13} - x_{12}$. The product of the three Mayer functions is

$$-f(x_{12})f(x_{13})f(x_{23}) = \Pi\left(\frac{x_{12}}{X_i + X_j}\right)\Pi\left(\frac{x_{13}}{X_i + X_k}\right)\Pi\left(\frac{x_{23}}{X_j + X_k}\right), \tag{5.11}$$

and the excluded length is

$$\begin{aligned}\hat{E}_{ijk} &= \int_{-\infty}^{\infty} dx_{12} \int_{-\infty}^{\infty} dx_{13}\, \Pi\left(\frac{x_{12}}{X_i + X_j}\right)\Pi\left(\frac{x_{13}}{X_i + X_k}\right)\Pi\left(\frac{x_{23}}{X_j + X_k}\right) \\ &= \int_{-(X_i+X_j)/2}^{(X_i+X_j)/2} dx_{12} \int_{-(X_i+X_k)/2}^{(X_i+X_k)/2} dx_{13}\, \Pi\left(\frac{x_{13} - x_{12}}{X_j + X_k}\right) \qquad (5.12) \\ &= (X_iX_j + X_jX_k + X_iX_k), \qquad (5.13)\end{aligned}$$

where in the last step we used geometric considerations shown in Fig. 5.8 to calculate the integral in Eq. (5.12).

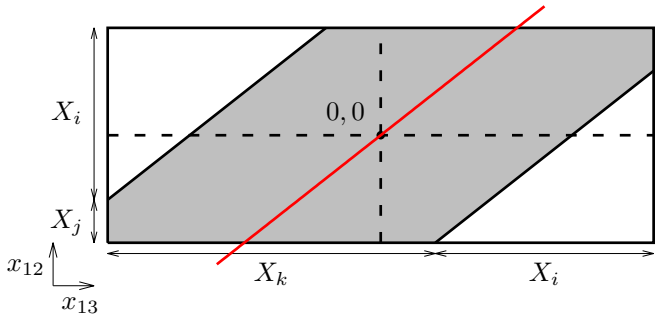

Figure 5.8.: The rectangle represents the integration bounds in Eq. (5.12), the red line is the line where $x_{13} - x_{12} = 0$, and the shaded region is the region where the rectangle function Π in the argument of Eq. (5.12) is unity (elsewhere it is zero).

As before, the three-dimensional case [Eq. (5.3)] is simply the product of the one-dimensional results for each direction.

Excluded volume of cuboids

Here for completeness we show the derivation of excluded volume $E(\Omega)$ [Eq. (1.12)] for cuboids of dimensions L, M, S, which is based on the calculation in Ref. [11].

A zonotope is a convex body that can be built from line segments through Minkowski addition. Each line segment is given by its length and orientation. A zonotope is then specified by the set of line segments: $\mathcal{L} = \{L_1, L_2, \ldots, L_n\}$, and defined through $Z(\mathcal{L}) = L_1 \oplus L_2 \oplus \cdots \oplus L_n$. The excluded volume of two zonotopes Z and Z' with line segments $\mathcal{L}$ and $\mathcal{L}'$, respectively, is then [11]

$$\begin{aligned} E(Z, Z') &= \mathcal{V}[Z(\mathcal{L} \cup \mathcal{L}')] \\ &= \mathcal{V}[Z(\mathcal{L})] + \mathcal{V}[Z(\mathcal{L}')] + \sum_{L \neq L' \in \mathcal{L}, L'' \in \mathcal{L}'} \mathcal{V}[L \oplus L' \oplus L''] \\ &+ \sum_{L \in \mathcal{L}, L' \neq L'' \in \mathcal{L}'} \mathcal{V}[L \oplus L' \oplus L''], \end{aligned} \tag{5.14}$$

where $\mathcal{V}[B]$ denotes the volume of the body (set) B.

We assume a cuboid is a zonotope consisting of three line segments: $\mathcal{B} = \{D_1, D_2, D_3\}$ with lengths d_1, d_2, d_3 and perpendicular orientations $\hat{m}_1, \hat{m}_2, \hat{m}_3$. Similarly, the second cuboid has $\mathcal{B}' = \{D_1', D_2', D_3'\}$ with lengths d_1', d_2', d_3' perpendicular orientations $\hat{m}_1', \hat{m}_2', \hat{m}_3'$. The volume of a single cuboid is given by

$$\mathcal{V}[Z(\mathcal{B})] = d_1 d_2 d_3. \tag{5.15}$$

The contribution from the first sum of Eq. (5.14), assuming $L_a \in \mathcal{B}$ and $L_b \neq L_c \in \mathcal{B}'$, is given by

$$\sum_{i=1}^{3} \sum_{1 \leq j,k \leq 3} d_i d_j' d_k' |\hat{m}_i \cdot (\hat{m}_j' \times \hat{m}_k')|. \tag{5.16}$$

Similarly, the contribution from the second sum of Eq. (5.14), assuming $L_a \neq L_b \in \mathcal{B}$ and $L_c \in \mathcal{B}'$, is given by

$$\sum_{i=1}^{3} \sum_{1 \leq j,k \leq 3} d_i' d_j d_k |\hat{m}_i' \cdot (\hat{m}_j \times \hat{m}_k)|. \tag{5.17}$$

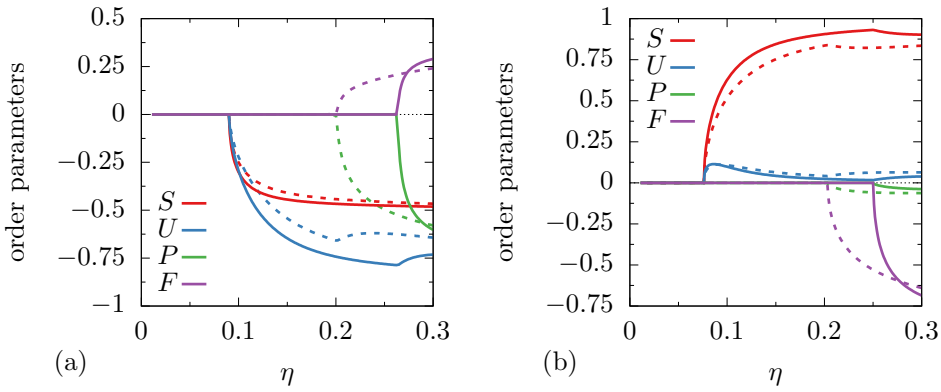

Figure 5.9.: Order parameters as a function of packing fraction η for a cuboid with (a) $M^* = 8$, $L^* = 61$ and (b) $M^* = 8$, $L^* = 72$, where we truncate at $l_{\max} = 2$ (dashed) and $l_{\max} = 4$ (solid).

We can write this explicitly in terms of angles, by fixing a coordinate system on the second particle: $\hat{m}'_1 = \hat{x}$, $\hat{m}'_2 = \hat{y}$, and $\hat{m}'_3 = \hat{z}$. We will further let the dimensions of each particle be $d_1 = d'_1 = M$, $d_2 = d'_2 = S$, and $d_3 = d'_3 = L$. Then the excluded volume as a function of the the three relative Euler angles $\Omega = (\alpha, \beta, \gamma)$ is

$$
\begin{aligned}
E(\Omega) = {} & 2LSM + M\,[\,2LS\,|\cos\alpha\cos\beta\cos\gamma - \sin\alpha\sin\gamma| \\
& + LM\,(\,|\cos\beta\cos\gamma\sin\alpha + \cos\alpha\sin\gamma| + |\cos\gamma\sin\alpha + \cos\alpha\cos\beta\sin\gamma|\,) \\
& + SM\,(|\cos\alpha\sin\beta| + |\cos\gamma\sin\beta|)\,] + L\,[\,LS\,(\,|\cos\alpha\sin\beta| \\
& + |\cos\gamma\sin\beta|\,) + LM\,(|\sin\alpha\sin\beta| + |\sin\beta\sin\gamma|) + 2SM\,|\cos\beta|\,] \\
& + S\,[\,LS\,(|\cos\beta\cos\gamma\sin\alpha + \cos\alpha\sin\gamma| + |\cos\gamma\sin\alpha + \cos\alpha\cos\beta\sin\gamma|) \\
& + 2LM\,|\cos\alpha\cos\gamma - \cos\beta\sin\alpha\sin\gamma| + SM\,(|\sin\alpha\sin\beta| + |\sin\beta\sin\gamma|)\,]\,.
\end{aligned}
$$

This result can be checked against that of hexagonal platelets in Ref. [11] by setting $\chi_1 = \chi_3 = 0$, $\chi_2 = \pi/2$, $d_1 = d_3 = M/2$, $d_2 = S$, and $\ell = L$.

Second-virial results to a higher order in l

Here we comment on the effect of adding higher order terms in l to the sum in Eq. (4.5). In Fig. 5.9, we show the order parameters as a function of packing fraction η for two different cuboid shapes and for different truncations in l. The main effect of truncating at $l_{\max} = 2$ (dotted curves) compared to

$l_{\max} = 4$ (solid curves) is a small underestimation in the order at a given density and an underestimation of the density of the uniaxial to biaxial nematic transition. We see that the qualitative behavior is well-captured by the $l_{\max} = 2$. The higher l do not change the phase diagram topology shown in Fig. 5.7(a), indeed, their only effect is a small increase in the packing fraction range of stability of the uniaxial nematic at the dual shape. We note that the computational cost of adding higher l beyond $l = 2$ grows rapidly, as there are $(2l + 1)^2$ coefficients at order l, and taking into account the symmetries of the cuboid this is reduced to $\sim (2l + 1)^2/4$.

Chapter 6.

Sedimentation of binary mixtures of rods

6.1. Introduction

Colloidal sedimentation-diffusion (SD) equilibria are the result of a competition between gravitational energy (which favors a high mass density at the bottom) and entropy (which favors a homogeneous distribution of matter). In a sufficiently dilute one-component system, where the particles can be considered non-interacting, the height-dependent density profile is simply the barometric distribution, a fact which can be used to determine the buoyant masses of colloids. Historically, however, Perrin used colloids with a known buoyant mass to determine Boltzmann's constant k_B from the barometric profile [17]. For one-component colloidal systems, a single density profile can be used to determine the osmotic equation of state. Therefore sedimentation is an important tool to gain information about thermodynamic properties [18–21].

Ultracentrifugation can also be used as a method to study SD equilibrium. Here the gravitational field is replaced by a centrifugal one, which allows for alteration of the (effective) buoyant mass by varying angular frequency of the centrifuge's rotation [124–126].

Gravity can also lead to non-barometric profiles and unexpected new phenomena, for instance when considering colloidal systems with electrostatic interactions. A well-studied example is the SD equilibrium of charged spheres at low salt, where interactions lead to the creation of a macroscopic electric field [125, 127–129]. A microscopic theory arising from a generalization of Archimedes' principle, which accounts for density perturbations in the solvent due to interactions with colloids, was successful in describing experimental results such as denser particles floating on top of a lighter fluid [130, 131].

Other counter-intuitive behavior occurs when considering mixtures, for example, a liquid floating between two gases [132] or a nematic phase floating on top of an isotropic phase in a platelet-sphere mixture [133]. For a recent review on sedimentation see Ref. [134].

It is more difficult, however, to draw conclusions about bulk phase diagrams of binary mixtures from SD experiments. Recently, Refs. [135, 136] showed that the chemical potential representation of a bulk phase diagram together with the local density approximation can be used to create a stacking diagram, which gives all possible stacking sequences of a binary mixture in SD equilibrium. In fact, an application of this method to patchy colloidal mixtures in SD equilibrium showed a good agreement between this method and Monte Carlo simulations which also included lateral walls [137]. In order to apply this method, it is necessary to revisit established results on binary mixtures in order to obtain bulk phase diagrams in the plane of chemical potentials.

One of the theoretically most accessible model systems of binary hard-core mixtures is rod-rod mixtures, since Onsager theory [5] can be used to obtain accurate results in the needle limit. There is a wealth of work concerning long and short rod mixtures, which have a rich phase behavior including isotropic-nematic demixing with strong fractionation [5, 100, 138, 139] and also, when the length ratio is sufficiently high, nematic-nematic demixing [138, 140–145]. Thick and thin rod mixtures can also exhibit isotropic-isotropic demixing, in addition to isotropic-nematic and nematic-nematic phase separation [146–149]. These mixtures were also studied theoretically for finite aspect ratio rods [150, 151] and in experiments [87], and are therefore a well-understood binary system.

Here we apply the method of Refs. [135, 136] to a binary mixture of thick and thin needles. First, in Sec. 6.2, we review Onsager theory for a binary mixture and display phase diagrams for three diameter ratios. We then construct the stacking diagrams using the chemical potential representation of the phase diagrams in Sec. 6.3. In addition, we show example sedimentation paths, which are given by lines in the plane of chemical potentials, but which we also translate into contours in the composition-pressure and density-density representations. We conclude in Sec. 6.4 by discussing relevant experimental results and possible difficulties in determining bulk properties from sedimentation profiles.

6.2. Onsager theory for binary mixtures

We briefly review Onsager theory extended to binary mixtures of thick and thin rods, closely following Ref. [148]. We consider N_σ hard rods of two species $\sigma = 1, 2$ with equal lengths L but different diameters D_1 and D_2, suspended in a solvent with volume V at room temperature T. The two species of rods have a diameter ratio $d = D_2/D_1 > 1$ and the total number of rods is $N = N_1 + N_2$. We assume needle-shaped rods with $L \gg D_1, D_2$ such that the excluded volume for a pair of rods of species σ and σ' is $(D_\sigma + D_{\sigma'})L^2|\sin\gamma|$, with γ the angle between the two rods. We define the dimensionless number density as $c = bN/V$, with $b = (\pi/4)L^2D_1$ the second virial coefficient of the thin rods in the isotropic phase, and the composition fraction of thick rods as $x = N_2/N$. Each species has an orientation distribution function $\psi_\sigma(\hat{\omega})$, where $\hat{\omega}$ is the orientation of the long axis of the rod. The free energy F is a functional of $\psi_1(\hat{\omega})$ and $\psi_2(\hat{\omega})$ given by [5, 100, 148]

$$\frac{\beta F[\psi_1, \psi_2]}{N} = f[\psi_1, \psi_2] = \ln c + f_{\rm mix} + f_{\rm or} + f_{ex}, \tag{6.1}$$

where the mixing contribution $f_{\rm mix}$, the orientation contribution $f_{\rm or}$, and the excess contribution $f_{\rm ex}$ due to excluded volume interactions are given by

$$\begin{aligned}
f_{\rm mix} &= x\ln x + (1-x)\ln(1-x),\\
f_{\rm or} &= \int d\hat{\omega}\,[(1-x)\psi_1(\hat{\omega})\ln\psi_1(\hat{\omega}) + x\psi_2(\hat{\omega})\ln\psi_2(\hat{\omega})]\,,\\
f_{\rm ex} &= \frac{4c}{\pi}\iint d\hat{\omega}\,d\hat{\omega}'|\sin\gamma|\,\left[(1-x)^2\psi_1(\hat{\omega})\psi_1(\hat{\omega}')\right.\\
&\qquad \left. + x(1-x)(1+d)\psi_1(\hat{\omega})\psi_2(\hat{\omega}') + x^2 d\,\psi_2(\hat{\omega})\psi_2(\hat{\omega}')\right].
\end{aligned}$$

For a given c and x, the equilibrium orientation distribution functions can be obtained by minimizing $f[\psi_1, \psi_2; c, x]$ with respect to $\psi_\sigma(\hat{\omega})$ at fixed normalizations $\int \psi_\sigma(\hat{\omega})\,d\hat{\omega} = 1$, which gives the equilibrium distributions as solutions of the integral equations [10, 148]

$$C_1 = \ln\psi_1(\hat{\omega}) + \frac{4c}{\pi}\int d\hat{\omega}|\sin\gamma|\,[2(1-x)\psi_1(\hat{\omega}') + x(1+d)\psi_2(\hat{\omega}')]\,, \tag{6.2}$$

$$C_2 = \ln\psi_2(\hat{\omega}) + \frac{4c}{\pi}\int d\hat{\omega}|\sin\gamma|\,[(1-x)(1+d)\psi_1(\hat{\omega}') + 2xd\,\psi_2(\hat{\omega}')]\,, \tag{6.3}$$

where C_σ are Lagrange multipliers that ensure proper normalizations of $\psi_\sigma(\hat{\omega})$.

At low enough c, the isotropic distributions $\psi_\sigma^{\mathrm{I}} = 1/(4\pi)$ are the only (stable) solutions to Eqs. (6.2) and (6.3) [13, 51], which gives for the free energy of the isotropic phase

$$f^{\mathrm{I}}(x,c) = \ln c + f_{\mathrm{mix}} - \ln(4\pi) + c(1+(d-1)x). \tag{6.4}$$

At higher densities, the excluded volume becomes more important in Eqs. (6.2) and (6.3) and the minimizing orientation distribution functions become peaked around a nematic director $\hat{n}$. If we choose a coordinate system with the z-axis parallel to $\hat{n} = (0,0,1)$, the unit vector $\hat{\omega}$ can be written as $\hat{\omega} = (\sin\theta\,\cos\varphi, \sin\theta\,\sin\varphi, \cos\theta)$, with φ the azimuthal angle and θ the polar angle with respect to $\hat{n}$. In the uniaxial nematic states of interest here, the orientation distribution function is independent of the azimuthal angle φ and has up-down symmetry, and so we can write $\psi(\hat{\omega}) = \psi(\theta) = \psi(\pi-\theta)$. To determine the orientation distribution function for the nematic phase, we solve Eqs. (6.2) and (6.3) using an iterative scheme on a discrete grid of polar angles $\theta \in [0, \pi/2)$ [52, 53]. In Ref. [148], a scaling analysis was used to determine the extremely peaked orientation distribution functions in the high-density limit. However, with present-day computational resources such a scaling is not needed in the density regime of interest here. This is illustrated in Fig. 6.1, where the orientation distribution functions $\psi_1(\theta)$ and $\psi_2(\theta)$ for both 500 and 5000 θ-angles are in good agreement in a region of high ordering where the nematic order parameters $S_\sigma = \langle (3\cos^2\theta - 1)/2 \rangle_\sigma$ are $S_1 = 0.996$ and $S_2 = 0.998$. Therefore we simply employ a θ-grid of 500 angles, which we deem sufficiently accurate for the present purposes. For a given d, x, and c, we numerically calculate the nematic equilibrium orientation distribution functions $\psi_1(\theta)$ and $\psi_2(\theta)$ and insert them into Eq. (6.1), which yields the equilibrium free energy of the nematic phase, $f^{\mathrm{N}}(x,c)$.

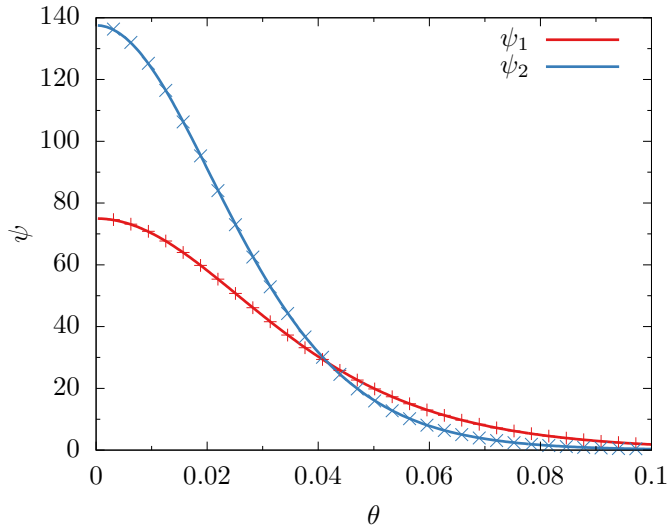

Figure 6.1.: Orientation distribution functions ψ_1 and ψ_2 of thin and thick needles as a function of the polar angle θ (in units of radians) for diameter ratio $d = 4.2$, composition $x = 0.99$, and density $c = 8$ for a grid of 500 angles (symbols) and of 5000 angles (lines). The order parameters for the thin and thick rods are $S_1 = 0.996$ and $S_2 = 0.998$, respectively.

The pressure P (in units of k_BT/b) and chemical potentials μ_σ (in units of k_BT) can be found from the free energy, using

$$\begin{aligned}
\beta b P^\alpha &= c^2 \left(\frac{\partial f^\alpha(x,c)}{\partial c} \right)_x , \\
\beta \mu_1^\alpha &= f^\alpha(x,c) + c \left(\frac{\partial f^\alpha(x,c)}{\partial c} \right)_x + (1-x) \left(\frac{\partial f^\alpha(x,c)}{\partial x} \right)_c , \\
\beta \mu_2^\alpha &= f^\alpha(x,c) + c \left(\frac{\partial f^\alpha(x,c)}{\partial c} \right)_x - x \left(\frac{\partial f^\alpha(x,c)}{\partial x} \right)_c ,
\end{aligned} \tag{6.5}$$

where $\alpha = \mathrm{I}, \mathrm{N}$ denotes the isotropic or nematic phase, respectively.

Coexistence between two states (x^α, c^α) and ($x^{\alpha'}$, $c^{\alpha'}$) is found using the conditions of chemical and mechanical equilibrium: $\mu_1^\alpha = \mu_1^{\alpha'}$, $\mu_2^\alpha = \mu_2^{\alpha'}$, and $P^\alpha = P^{\alpha'}$.

As shown in Ref. [148], there are four distinct phase diagram topologies for all possible diameter ratios $d > 1$. For all diameter ratios there is isotropic-

nematic demixing and for $d < 4$ this is the only demixing. For $4 \leq d < 4.29$ there is also nematic-nematic demixing ending in a consolute point, while for $d \geq 4.29$ this nematic-nematic demixing is no longer closed by the consolute point. For $d \geq 8$ there is an additional isotropic-isotropic demixing. Here we will examine three diameter ratios ($d = 3.5$, 4.2, 10) which have increasing complexity and show all possible features.

For the diameter ratio $d = 3.5$, we show in Fig. 6.2 the phase diagram in (a) the composition x-pressure P and (b) density c_1-density c_2 representations, where we define the dimensionless number density of thin rods as $c_1 = c(1-x)$ and the density of thick rods as $c_2 = cxd$. For this diameter ratio, the only stable coexistence is found between isotropic (I) and nematic (N) phases [148]. The spindle-shaped I-N coexistence region (shaded with tie-lines shown as dashed lines) shows considerable fractionation, since the thicker rods have a stronger tendency to orientational order. Fig. 6.2(a) is in quantitative agreement with previous results from Ref. [148].

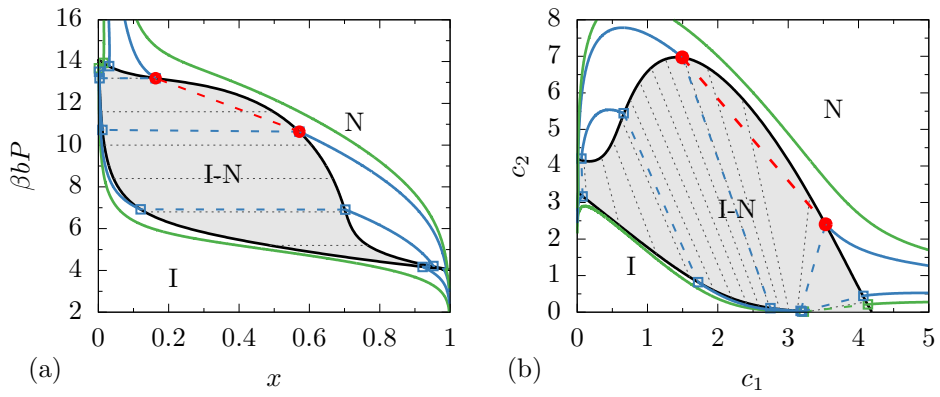

Figure 6.2.: Bulk phase diagram for diameter ratio $d = 3.5$ in (a) the composition x - pressure P and (b) the density c_1- density c_2 representations, where x denotes the mole fraction of thicker rods (species 2). The tie-lines connecting coexisting isotropic (I) and nematic (N) phases are shown by dashed lines. The colored curves indicate sedimentation paths discussed in Sec. 6.3.

The phase behavior becomes more complicated for the diameter ratio of $d = 4.2$. For this diameter ratio, there is not only an isotropic-nematic demixing, but also a nematic-nematic (N_1-N_2) demixing as shown in Fig. 6.3 in (a) in the composition x-pressure P and in (b) in the density c_1-density c_2 representation. Here we denote the nematic phase rich in thin rods by N_1 and the nematic phase rich in thick rods by N_2. In addition, we have an

isotropic-nematic-nematic (I-N_1-N_2) triple point (black dots) and a nematic-nematic (N_1-N_2) upper critical point (black square). We note that while the I-N binodals of Fig. 6.3(a) are in good agreement with results from Ref. [148], the N_1-N_2 critical point occurs at about half of the pressure and at slightly higher x than was found in Ref. [148]. However, since we have checked and demonstrated in Fig. 6.1 that our θ-grid is sufficiently accurate, we believe this difference is caused by the sensitivity of the phase boundaries to small numerical inaccuracies in the orientation distribution function calculated within the high-pressure scaling analysis.

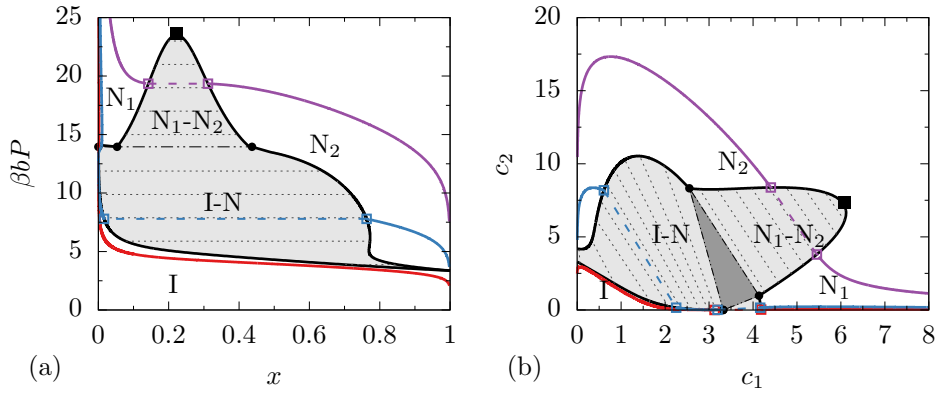

Figure 6.3.: Bulk phase diagram for diameter ratio $d = 4.2$ in (a) the composition x - pressure P and (b) the density c_1- density c_2 representations. The tie-lines connecting coexisting isotropic-nematic (I-N) and nematic-nematic (N_1-N_2) phases are shown by dashed lines. The nematic-nematic critical point is denoted by a black square and the isotropic-nematic-nematic triple point by black dots. The colored curves indicate sedimentation paths discussed in Sec. 6.3.

The final diameter ratio we consider here is $d = 10$. As shown in Fig. 6.4, there is an isotropic-isotropic (I_1-I_2) demixing at low pressures ending in a lower I_1-I_2 critical point (black square), and an I_1-I_2-N_2 triple point (black dots). In addition, this diameter ratio (and any with $d \geq 4.29$) also features an I-N_1-N_2 triple point at pressures beyond the scale of Fig. 6.4, with the nematic-nematic demixing persisting as $P \to \infty$ [148]. For both Fig. 6.4(a) the composition x-pressure P and Fig. 6.4(b) the density c_1-density c_2 representation the plot ranges are limited to low pressures/ densities for clarity.

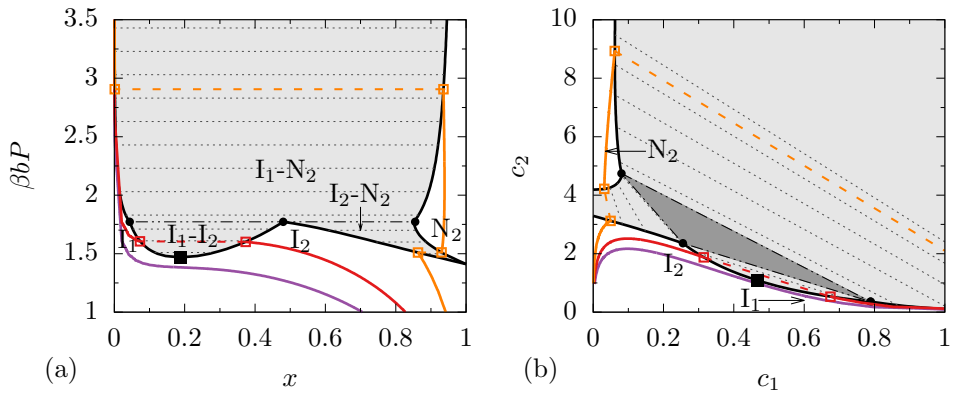

Figure 6.4.: Bulk phase diagrams for diameter ratio $d = 10$ in (a) the composition x - pressure P and (b) the density c_1- density c_2 representations. The tie-lines connecting coexisting isotropic-isotropic (I_1-I_2), isotropic-nematic (I_2-N_2 and I_1-N_2) phases are shown by dashed lines. The isotropic-isotropic critical point is denoted by a black square and the isotropic-isotropic-nematic triple point by black dots. The colored curves indicate sedimentation paths discussed in Sec. 6.3.

6.3. Sedimentation

We now consider a binary colloidal mixture in sedimentation-diffusion equilibrium, following the theoretical framework but not the notation of Refs. [132, 133, 135, 136]. In the employed local density approximation (LDA), the height-dependent local chemical potential of species $\sigma = 1, 2$ in the phase $\alpha = \mathrm{I}, \mathrm{N}$ can be written as [152]

$$\beta\mu_\sigma^\alpha\left(x(z), c(z)\right) = \beta\mu_\sigma^{\mathrm{tot}} - z/l_\sigma, \tag{6.6}$$

where z is the vertical coordinate, $\mu_\sigma^{\mathrm{tot}}$ is the total chemical potential of species σ (which is a spatial constant in equilibrium), and $l_\sigma = k_B T/(m_\sigma g)$ is the gravitational length of species σ with m_σ the buoyant mass and g the acceleration due to gravity. Eliminating z from Eq. (6.6) for $\sigma = 1, 2$, allows us to write the linear relation

$$\beta\mu_2^\alpha(\mu_1^\alpha) = a + s\beta\mu_1^\alpha, \tag{6.7}$$

where the "composition" variable a and the slope s are defined by

$$\begin{aligned} a &= \beta\mu_2^{\text{tot}} - s\beta\mu_1^{\text{tot}}, \\ s &= m_2/m_1. \end{aligned} \tag{6.8}$$

Note that a large positive a implies a 2-rich sample and that s can take positive or negative values depending on the signs of the buoyant masses.

For a given a and s, i.e., for a given overall composition of the sample and the buoyant masses of the particles, Eq. (6.7) gives a sedimentation path through the phase diagram in the μ_1-μ_2 representation. The crossing of a binodal in the μ_1-μ_2 phase diagram corresponds to the interface between two phases in a test tube and we can use Eq. (6.6) to relate a difference in heights in the sample $\Delta z = z_1 - z_2$ to a difference in either of the chemical potentials as

$$\beta\Delta\mu_\sigma = \beta\mu_\sigma(x(z_1), c(z_1)) - \beta\mu_\sigma(x(z_2), c(z_2)) = -\Delta z/l_\sigma. \tag{6.9}$$

Since following one line (segment) in the μ_1-μ_2 phase diagram gives the height-dependent sequence of phases in a test tube, all possible lines in this representation give all possible stacking sequences. A stacking sequence is thus determined by the slope s (the ratio of the buoyant masses of the two species), the length of the path (proportional to the height of the container), the composition variable a (determined by the overall composition and concentration), and the direction of the path (determined by the signs of the buoyant masses) [132, 133, 135, 136].

In order to construct a stacking diagram, we must find boundaries between stacking sequences in the s-a plane. Following Refs. [135, 136] we distinguish three types of features in these diagrams: (1) Sedimentation binodals– the set of all lines tangent to a binodal in the μ_1-μ_2 phase diagram, (2) terminal lines– the set of all lines through an end point of a binodal (triple point or critical point), and (3) asymptotic terminal lines– the set of lines with the asymptotic slope of a bulk binodal that does not terminate at a finite chemical potential. Note that both horizontal and vertical asymptotic terminal lines occur for a binary mixture approaching a pure composition ($\mu_\sigma \to -\infty$ corresponding to $N_\sigma/V \to 0$), however, in the s-a representation, the vertical asymptote does not appear as it corresponds to a line with infinite slope s.

We now present the phase diagrams of Sec. 6.2 in the plane of chemical potentials, from which we construct corresponding stacking diagrams. For the diameter ratio of $d = 3.5$, the chemical potential μ_1- chemical potential

μ_2 phase diagram, shown in Fig. 6.5(a), consists of a single binodal separating the isotropic phase (I) from the nematic phase (N), with a vertical and a horizontal asymptote corresponding to $x = 0, 1$. Even this simple phase diagram gives rise to four different stacking sequences in our stacking diagram, as shown in Fig. 6.5(b). Here we label all stacking sequences from bottom to top of sample under the assumption that $m_1 < 0$; if we had taken the assumption instead that $m_1 > 0$, the labels would describe the path from top to bottom of the test tube. There are two stacking sequence boundaries in Fig. 6.5(b): one sedimentation binodal (solid line) and one asymptotic terminal line (dotted line). The most complicated of four sequences, ININ, is made possible by the existence of an inflection point in the binodal in Fig. 6.5(a), which allows the binodal in the μ_1-μ_2 representation to be crossed three times by a straight line. We have added lines to Fig. 6.5(a), which show four possible sedimentation paths corresponding to distinct points in Fig. 6.5(b), with the colors of the sedimentation path corresponding to those of its stacking sequence in Fig. 6.5(b) (crosses are shown here for each sedimentation path in (a)). For the four different fixed s and a, we have sedimentation lines in Fig. 6.5(a), which can be transformed to sedimentation contours in the phase diagrams of Fig. 6.2(a) and (b). These contours must satisfy $a = \beta\mu_2^\alpha(c, x) - s\beta\mu_1^\alpha(c, x)$ from which the contours in the c_1-c_2 representation follow readily. Moreover, since we know $P(c, x)$, by inverting this to find $c(P, x)$ we can plot contours in the $(x,\ P)$ plane as well.

For the diameter ratio of $d = 4.2$, we show the μ_1-μ_2 representation in Fig. 6.6(a). As discussed in the previous section, for this diameter ratio there is not only isotropic-nematic demixing, but also nematic-nematic (N_1-N_2) demixing. As in Fig. 6.3, we have an I-N_1-N_2 triple point (black dot) and a N_1-N_2 critical point (black square). In Fig. 6.6(b) we show the stacking diagram in the s, a plane, and in Fig. 6.6(c) we show a zoomed-in version of this. The stacking diagram has five different boundaries: two sedimentation binodals (solid lines), one asymptotic terminal line (dotted line), and two terminal lines corresponding to the triple point and the critical point (dashed lines). Altogether, we find twelve regions, eleven of which are distinct stacking sequences (note that some colors are repeated), some of which are so small that they can only be seen in the zoom-in shown in (c). The smallest of these, $IN_1N_2N_1$ in the lower right of (c), comes from the fact that the calculated N_1-N_1 binodal in (a) is very close to, but not perfectly linear; however, these tiny regions may not be easily experimentally accessible, so here we focus on a few of the larger regions. Three of the larger regions are illustrated by the sedimentation lines shown in Fig. 6.6(a), corresponding to the crosses

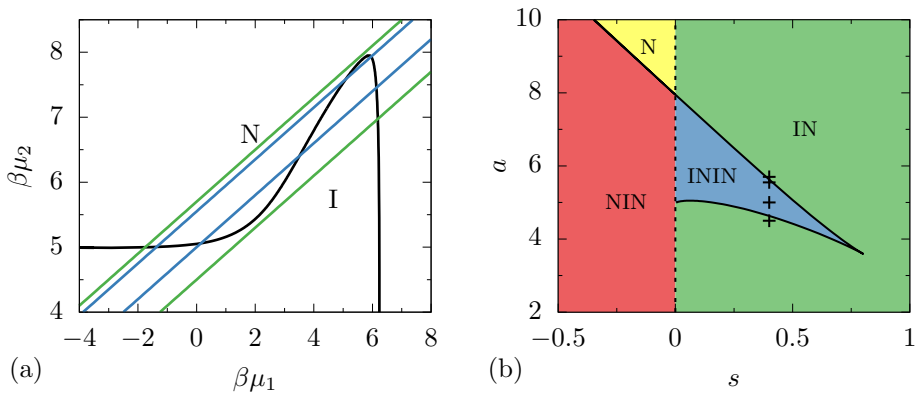

Figure 6.5.: (a) Bulk phase diagram for diameter ratio $d = 3.5$ in the plane of the chemical potentials μ_1-μ_2, where lines show sedimentation paths with slope $s = 0.4$ and intercept a of 4.5 (lower green), 5 (lower blue), 5.55 (upper blue) and 5.7 (upper green). (b) Stacking diagram for $d = 3.5$ in the slope s, composition a plane (see text), where the plus symbols represent the four sedimentation lines from (a). See text for explanation of the regions and curves.

in Fig. 6.6(b), with their equivalent sedimentation contours shown in the x-P and c_1-c_2 representations of the phase diagram in the previous section (Fig. 6.3). Clearly, the crossing of a μ_1-μ_2 line can correspond to a huge density or composition jump in the x-P and c_1-c_2 representations.

The final diameter ratio we consider is $d = 10$ (Fig. 6.7). As shown in the plane of chemical potentials in Fig. 6.7(a), we have an I-N_1-N_2 triple point (black triangle), an I_1-I_2 critical point (black square), and an I_1-I_2-N_2 triple point (black dot). The N_1-N_2 binodal has a well-defined slope as $\mu_{1,2} \to \infty$ [136]. In Fig. 6.7(a) we also show three examples of sedimentation paths corresponding to three points in the stacking diagram shown in (b) and three sedimentation contours in the x-P and c_1-c_2 phase diagrams of Fig. 6.4. In Fig. 6.7(b), we see that the stacking diagram is extremely rich; there are three sedimentation binodals (solid lines), one asymptotic terminal line (dotted line), and three terminal lines corresponding to the two triple points and one critical point (dashed lines). Altogether, we find sixteen distinct stacking sequences [though colors are repeated in Fig. 6.7(b)].

We use the fact that a difference in heights is proportional to a difference in chemical potential [see Eq. (6.9)], to plot the dependence of composition x and density c on height z (in units of the gravitational length l_1 of species one). For diameter ratio $d = 3.5$, we show in Fig. 6.8 four "test tubes" corresponding

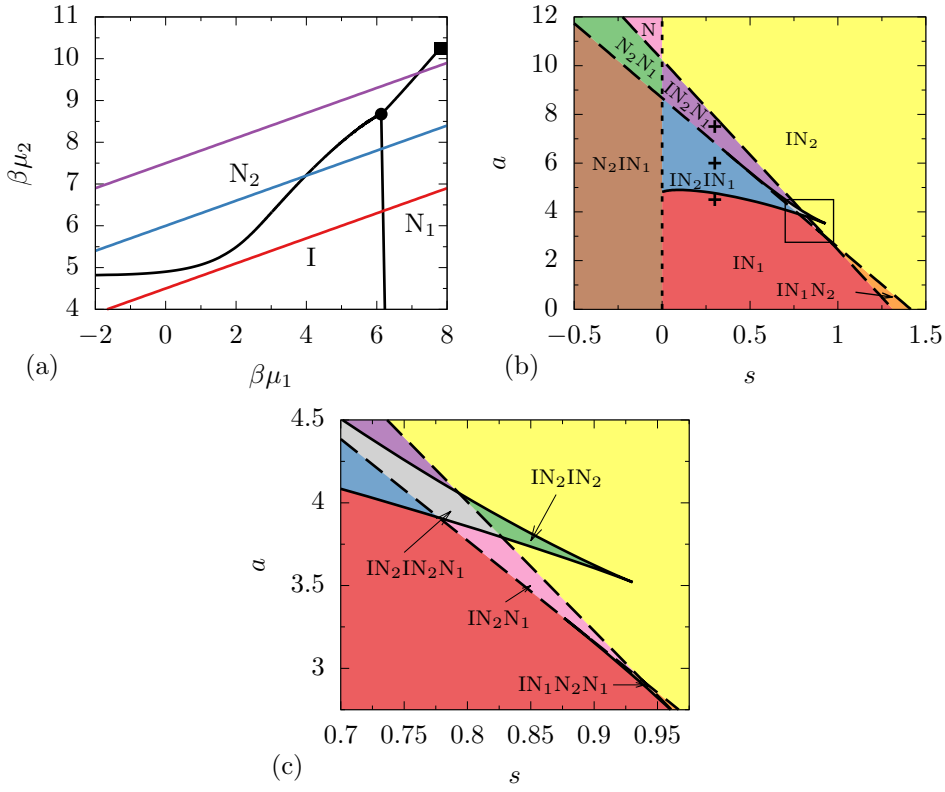

Figure 6.6.: (a) Bulk phase diagram for diameter ratio $d = 4.2$ in the plane of the chemical potentials μ_1-μ_2, where lines show sedimentation paths with slope $s = 0.3$ and intercept a of 4.5 (red), 6 (blue), and 7.5 (purple). (b) Stacking diagram for $d = 4.2$ in the slope s, composition a plane (see text), where the plus symbols represent the sedimentation lines from (a). In (c) we show a zoomed in version of (b). See text for explanation of the regions and curves.

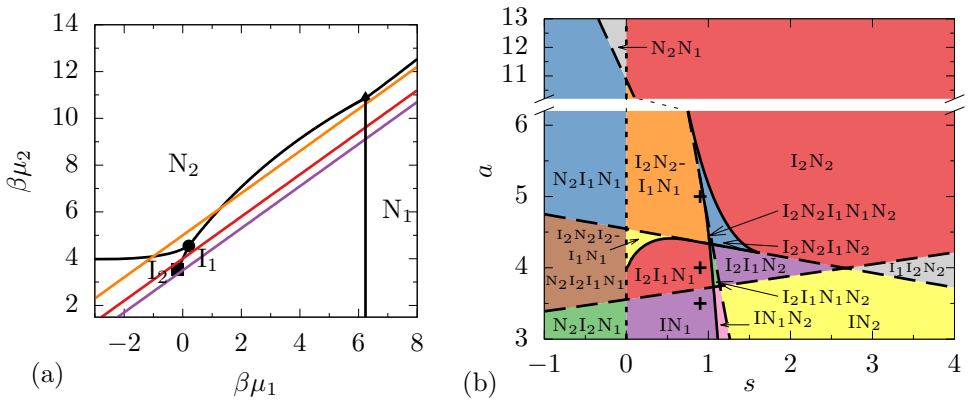

Figure 6.7.: (a) Bulk phase diagram for diameter ratio $d = 10$ in the plane of the chemical potentials μ_1-μ_2, where lines show sedimentation paths with slope $s = 0.9$ and intercept a of 3.5 (purple), 4 (red), and 5 (orange). (b) Stacking diagram for $d = 10$ in the slope s, composition a plane (see text), where the plus symbols represent the sedimentation lines from (a). See text for explanation of the regions and curves.

to the four sedimentation contours with $s = 0.4$ and (a) $a = 4.5$, (b) $a = 5$, (c) $a = 5.55$, and (d) $a = 5.7$ displayed in Figs. 6.2 and 6.5. Here we take both buoyant masses to be positive (which leads to inverted stacking sequences with respect to previous figures where we assumed $m_1 < 0$). We arbitrarily choose a test tube of height $12l_1$ by limiting $\beta\mu_1 \in [-4, 8]$ in all four cases (which also limits μ_2 for a given a and s); a shorter test tube could limit the number of layers that are seen. In Fig. 6.8(a) we see a stacking sequence with a thin-rich nematic phase on the bottom and above that an isotropic phase that transitions from thin-rich to thick-rich with increasing height. In Fig. 6.8(b) there are four sedimented layers, from bottom to top: a thin-rich nematic, a thin-rich isotropic, a thick-rich nematic, and a thick-rich isotropic. Here we see that the density and composition are non-monotonic in z. Similarly, there are four layers in Fig. 6.8(c), with the bottommost isotropic layer becoming thinner as the middle nematic layer grows thicker, and the changes in composition and density at the interfaces between phases being more pronounced than in (b). Finally, in Fig. 6.8(d), there are once again only two layers, namely a large nematic layer which transitions from thin- to thick-rich with a thick-rich isotropic floating on top.

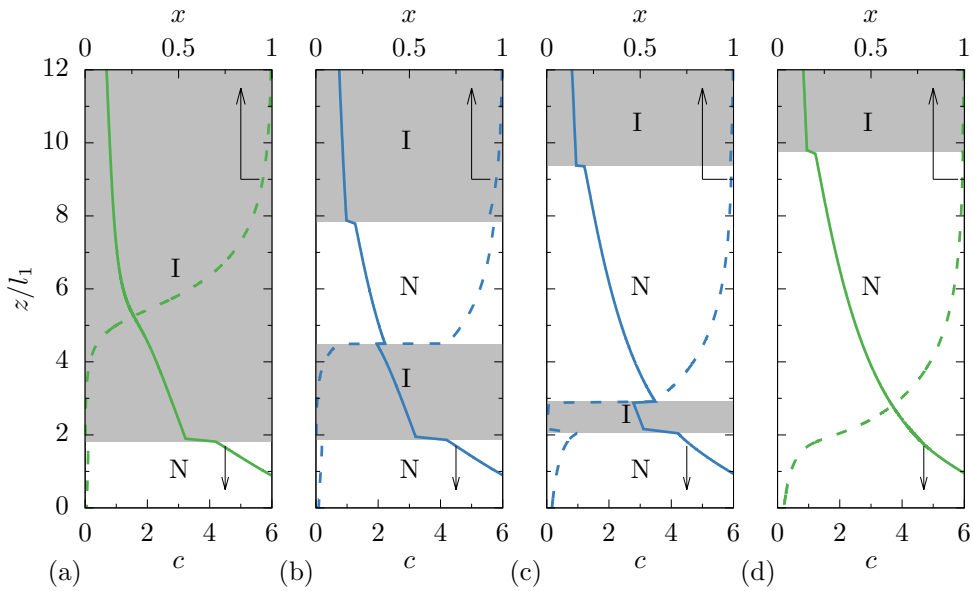

Figure 6.8.: Composition x (dashed) and density c (solid) as a function of height in test tube z (rotated so z is on vertical axis) for diameter ratio $d = 3.5$, slope $s = 0.4$, and composition variable (a) $a = 4.5$, (b) $a = 5$, (c) $a = 5.55$, and (d) $a = 5.7$ (see also Figs. 6.2 and 6.5). Gray indicates an isotropic phase (I) while the white indicates a nematic phase (N) and the arrows are to emphasize that the dashed curves correspond to the upper x-axes while the solid curves correspond to the lower x-axes. Here we assume both species have positive buoyant masses.

6.4. Summary and discussion

We studied the sedimentation of binary mixtures of thick and thin hard rods, focusing on diameter ratios $d = 3.5, 4.2, 10$ by considering sedimentation paths as straight lines in the plane of chemical potentials. This method is based on the local density approximation, which is known to be good for most colloidal rod systems, since the typical gravitational lengths of these systems of roughly a centimeter are much larger than all relevant correlations lengths. An exception is colloidal silica rods, which may have gravitational lengths on the order of the particle dimensions [3, 153, 154]. By considering all sedimentation paths, we constructed stacking diagrams. Experimentally, it is possible to sample the different regions of the stacking diagram by changing the composition of the mixture, the height of the container, and the maximum accessible density by e.g. (ultra)centrifugation [124–126, 135, 136].

We found that even the simplest phase diagram (for diameter ratio $d = 3.5$), with only spindle-shaped isotropic-nematic demixing, led to a stacking diagram with four regions, including sequences with an isotropic phase floating between two nematic phases. Adding a single binodal and associated critical and triple points, as occurs for diameter ratio $d = 4.2$, increases this number of regions to eleven distinct stacking sequences. Our richest phase diagram (for diameter ratio $d = 10$), contained two triple points and one critical point, produced a stacking diagram with sixteen distinct regions, including two with five sedimented layers. In addition to this straightforward application of the method developed in Refs. [135, 136], we also translated sedimentation lines from the plane of chemical potentials to paths in the more familiar representations of composition-pressure and density-density, and showed the density and composition profiles as a function of height for the diameter ratio $d = 3.5$.

The sedimentation contours shown in Figs. 6.2-6.4 are very "jumpy", with several possibly surprising effects of gravity on binary mixtures present. In Fig. 6.8, we see for instance that there are rapid changes in composition and density as a function of height in a "test tube", which change non-monotonically along the sedimentation path. Figures 6.8(b) and (c) show the stacking sequences NINI, which is possible even though there is no triple point in the bulk phase diagram. This leads us to the point that studying the sedimentation of mixtures experimentally demands great care in drawing conclusions about the bulk phase diagrams. If the concentrations of the two coexisting phases are measured sufficiently close to the interface between two layers, it should indeed be possible to experimentally reconstruct the bulk

phase diagram on the basis of measurements of many sample compositions. Suppose however, that a layer is very thin (e.g. even thinner than the middle isotropic phase in Fig. 6.8(c)) such that it is experimentally invisible or missed. The observed sedimentation sequence might then be assumed to imply that a thick-rich nematic coexists with a thin-rich nematic. This potential "mistake" is illustrated by the red dashed lines in Figs. 6.2(a) and (b) that show a hypothetical "false" nematic-nematic coexistence line, even though there is no nematic-nematic demixing present in the bulk phase diagram.

In Ref. [87], the phase behavior of binary mixtures of fd virus and fd coated with neutral polymer polyethylene glycol (PEG) was studied. The diameter of the bare fd was varied by changing the ionic strength, which varied its effective diameter and thus the diameter ratio, while the buoyant mass ratio remained fixed at $0.3 \leq s \leq 0.7$ and the gravitational length of the bare fd was approximately 4 cm. For diameter ratios $d \geq 3$ the authors find N_{thin}-I_{thin}-N_{thick} and N_{thin}-N_{thick} stacking sequences. We show in Figs. 6.2 and 6.5 that an NIN stacking sequence can occur without the presence of triple point, and as argued above, an observed coexistence between two nematics could possibly be a NIN stacking sequence with a very thin isotropic layer. In the case of Ref. [87], a convincing phase diagram which included an N_{thin}-I_{thin}-N_{thick} triple point and nematic-nematic demixing was presented based on many measurements, and was also qualitatively backed up by theoretical calculations [151]. However, we do wish to stress that a single observation of a stacking sequence of the type ABA of phases A and B in a binary mixture does not imply the existence of an AAB triple point in the bulk phase diagram.

Though a single sedimentation density profile for a one-component system yields the full equation of state of the system, for colloidal mixtures this is clearly not so. Here we illustrated the inherent difficulties in drawing conclusions about bulk phase diagrams of binary mixtures. So although systematic measurements of SD properties do allow for conclusions to be drawn about bulk phase diagrams of mixtures, one should be wary and study a large set of thermodynamic state points.

Onsager theory only gives quantitative results for needlelike, rigid rods but it can be readily generalized to study more realistic systems as well. Both including finite size effects [151] and adding flexibility [88, 89] were shown to give better agreement with experimental results for binary mixtures of fd virus. However, the ungeneralized Onsager theory did capture qualitative features of the phase behavior including the isotropic-nematic, nematic-nematic, and isotropic-isotropic demixing.

Here we only considered homogeneous phases, but of course at higher pressures one should expect phases with partial positional ordering, such as smectic phases. For a one-component system of needlelike rods, the nematic-smectic transition occurs at pressures far beyond the isotropic-nematic transition, however, for rods with a small aspect ratio $L/D \sim 4 - 5$ the nematic regime is small and direct isotropic-smectic transitions are to be expected [4]. For a binary mixture, these inhomogeneous phases will also lead to richer phase diagrams and hence richer stacking diagrams. For shorter rods, smectic phases can preempt isotropic-nematic and nematic-nematic transitions, thus significantly altering the phase diagram [155].

We note that three-component systems, let alone polydisperse ones, are expected to be even richer, but also considerably more complicated to analyze in full detail. This is left for future studies.

Acknowledgments

We thank Patrick Hooijer and Marjolein Dijkstra for helpful discussions.

Chapter 7.

Connectedness percolation of deformed rods

7.1. Introduction

Nanocomposites of carbon nanotubes or metallic wires dispersed in plastics are seen to be promising replacements of indium tin-oxide for transparent electrodes [156, 157]. Opto-electronic applications of this material require as low as possible percolation thresholds, to keep the materials transparent. The percolation threshold, the critical filler loading required to get significant electrical conduction, depends crucially on the formulation and processing of the composite. It is not surprising then that a significant amount of effort has been invested and continues to be invested in understanding what factors precisely control the percolation threshold [157].

Continuum percolation theory and computer simulations of highly idealized models of the elongated filler particles, usually modeled as hard rods or ellipsoids, indicate that the filler fraction at the percolation threshold should be of the order of the inverse aspect ratio of the particles [157]. Similar models have been invoked to study the impact of length and width polydispersity [158–163], attractive interactions [158], alignment [164, 165], etc. While being very informative, the question arises how accurate these idealized models are. Indeed, carbon nanotubes are often not straight cylinders but instead quite tortuous or riddled with kink defects [166, 167]. The same is true for other types of conductive filler particles. However, little theoretical effort has been put into studying the applicability of these perfect rod models to systems with shape defects.

In this chapter, we investigate the impact of the precise shape of the rods upon the percolation threshold. For this purpose, we apply connectedness percolation theory to kinked and bent rods. Here we vary the aspect ratio,

the kink location and angle, and the curvature. We find that the main contributing factor in determining the percolation threshold is the aspect ratio, not the precise shape of the particle, unless it is extremely deformed. This implies that idealized models are indeed useful in an experimental context. We also find that the universal scaling of the percolation threshold with particle length and connectivity range is only very weakly affected by the particle shape.

The remainder of this chapter is structured as follows. In Sec. 7.2, we present the methodology that we base our calculations on. We use connectedness percolation theory within the second-virial approximation, augmented by the Parsons-Lee correction in order to account for finite-size effects. We use Monte Carlo integration to calculate the overlap volumes of the particles. In Sec. 7.3, we present our results and we summarize our findings in Sec. 7.4.

7.2. Method

Here we study the size of clusters of connected particles, where we define two particles as connected if their surface-to-surface distance is less than a certain connectedness criterion (connectedness range) Δ. This connectedness criterion is related to the electron tunneling distance and depends on the nanofiller properties as well as the dielectric properties of the medium [158, 168]. Using connectedness percolation theory [169, 170], we study the average cluster size of connected particles. Specifically, we are interested in the percolation threshold, that is, the lowest density at which the average cluster size diverges.

For completeness and clarity, we now give the full derivation of the percolation threshold. Letting n_k denote the number of clusters of $k = 1, 2, \ldots$ particles, then the probability of a particle being in a cluster of size k is simply $s_k = kn_k/N$, where $N = \sum_k kn_k$ is the total number of particles [171]. Then the weight-averaged number of particles in a cluster is defined as $S = \sum_k ks_k = \sum_k k^2 n_k/N$. This can be rewritten as $S = \sum_k (kn_k + k(k-1)n_k)/N = 1 + 2N_c/N$, where in the last step we defined $N_c = \sum_k k(k-1)n_k/2$, which is the number of pairs of particles within the same cluster [171]. The density at which S diverges is the percolation threshold, and in addition S can be probed indirectly by measuring the frequency-dependent dielectric response, which has a sharp peak at the percolation threshold [172]. Below we calculate N_c, and thus S.

Now we consider clusters composed of rigid, non-spherical particles. The orientation of such particles can be given by three Euler angles $\Omega = (\alpha, \beta, \gamma)$. Assuming a uniform spatial distribution of particles with number density ρ, the orientation distribution function $\psi(\Omega)$ is defined so that the probability to find a particle with an orientation in the interval $d\Omega$ is given by $\psi(\Omega)d\Omega$, with the normalization constraint that $\int d\Omega\, \psi(\Omega) = \int_0^{2\pi} d\alpha \int_0^{\pi} d\beta \sin\beta \int_0^{2\pi} d\gamma\, \psi(\Omega) = 1$. The orientational average is denoted $\langle \ldots \rangle_\Omega = \int d\Omega \ldots \psi(\Omega)$.

The pair connectedness function P is defined such that $\rho^2 P(\mathbf{r}_1, \mathbf{r}_2, \Omega_1, \Omega_2)$ $\psi(\Omega_1)\psi(\Omega_2) d\mathbf{r}_1 d\mathbf{r}_2 d\Omega_1 d\Omega_2$ is the probability of finding a particle in volume $d\mathbf{r}_1$ with orientation in $d\Omega_1$ and a second particle in volume $d\mathbf{r}_2$ with orientation in $d\Omega_2$, given that the two particles are in the same cluster [170]. From this definition, it follows that

$$\begin{aligned} N_c &= \frac{\rho^2}{2} \int d\mathbf{r}_1 \int d\mathbf{r}_2 \langle \langle P(\mathbf{r}_1, \mathbf{r}_2, \Omega_1, \Omega_2) \rangle_{\Omega_1} \rangle_{\Omega_2} \\ &= \frac{\rho N}{2} \int d\mathbf{r}_{12} \langle \langle P(\mathbf{r}_{12}, \Omega_1, \Omega_2) \rangle_{\Omega_1} \rangle_{\Omega_2}, \end{aligned} \tag{7.1}$$

where the one-half prefactor avoids double counting and in the second line of Eq. (7.1) we assume translational invariance with $\mathbf{r}_{12} = \mathbf{r}_1 - \mathbf{r}_2$. It follows that the weight-averaged cluster size can be written as

$$S = \lim_{\mathbf{q} \to 0} S(\mathbf{q}), \tag{7.2}$$

with

$$S(\mathbf{q}) = 1 + \rho \langle \langle \hat{P}(\mathbf{q}, \Omega_1, \Omega_2) \rangle_{\Omega_1} \rangle_{\Omega_2}, \tag{7.3}$$

where we denote the Fourier transform of an arbitrary function g by $\hat{g}(\mathbf{q}) = \int d\mathbf{r} g(\mathbf{r}) \exp(i\mathbf{q} \cdot \mathbf{r})$.

The Fourier transform of the pair connectedness function obeys the connectedness Ornstein-Zernike equation, given by [170]

$$\hat{P}(\mathbf{q}, \Omega_1, \Omega_2) = \hat{C}^+(\mathbf{q}, \Omega_1, \Omega_2) + \rho \langle \hat{C}^+(\mathbf{q}, \Omega_1, \Omega_3) \hat{P}(\mathbf{q}, \Omega_3, \Omega_2) \rangle_{\Omega_3}, \tag{7.4}$$

with $\hat{C}^+(\mathbf{q}, \Omega_1, \Omega_2)$ the spatial Fourier transform of the direct pair connectedness function which measures short-range correlations. Given a closure for $\hat{C}^+$, we can calculate $\hat{P}(\mathbf{q}, \Omega_1, \Omega_2)$ and thus $S(\mathbf{q})$.

In this thesis, we only consider percolation in the isotropic phase, where all orientations are equally probable and so $\psi(\Omega) = 1/(8\pi^2)$. Due to the global rotational invariance of the system and symmetry under particle exchange, the pair connectedness function $\hat{P}$ has the following properties

$$\hat{P}(\mathbf{q}, \Omega_1, \Omega_2) = \hat{P}(\mathbf{q}, \Omega_{12}) = \hat{P}(q, \Omega_{12}) = \hat{P}(q, \Omega_{21}), \tag{7.5}$$

where $q = |\mathbf{q}|$ and $\Omega_{12} = \Omega_1^{-1}\Omega_2$ denotes the relative orientation between particle 1 and particle 2. Analogous properties hold for $\hat{C}^+$.

Using the properties in Eq. (7.5) and integrating both sides in Eq. (7.4) over Ω_2 gives

$$\langle \hat{P}(q, \Omega_{12})\rangle_{\Omega_2} = \langle \hat{C}^+(q, \Omega_{12})\rangle_{\Omega_2} + \rho\langle \hat{C}^+(q, \Omega_{13})\, \langle \hat{P}(q, \Omega_{32})\rangle_{\Omega_2}\, \rangle_{\Omega_3}. \tag{7.6}$$

Consider the second term on the right-hand side of Eq. (7.6). By a measure-invariant change of variables $\Omega_2 \to \Omega_3^{-1}\Omega_2 = \Omega_{32}$, we find that $\langle \hat{P}(q, \Omega_{32})\rangle_{\Omega_2} = \langle \hat{P}(q, \Omega_{32})\rangle_{\Omega_{32}}$. By subsequently performing similar changes of variables on the remaining integrals in Eq. (7.6), we find

$$\langle \hat{P}(q, \Omega_{12})\rangle_{\Omega_{12}} = \langle \hat{C}^+(q, \Omega_{12})\rangle_{\Omega_{12}} + \rho\langle \hat{C}^+(q, \Omega_{13})\rangle_{\Omega_{13}}\langle \hat{P}(q, \Omega_{32})\rangle_{\Omega_{32}} \tag{7.7}$$

which can be solved as

$$\langle \hat{P}(q, \Omega)\rangle_{\Omega} = \frac{\langle \hat{C}^+(q, \Omega)\rangle_{\Omega}}{1 - \rho\langle \hat{C}^+(q, \Omega)\rangle_{\Omega}}. \tag{7.8}$$

Therefore the weight-averaged cluster size obeys

$$S = \frac{1}{1 - \rho \lim_{q\to 0}\langle \hat{C}^+(q, \Omega)\rangle_{\Omega}}. \tag{7.9}$$

The percolation threshold is defined as the density at which Eq. (7.9) diverges, i.e.,

$$\rho_P = \frac{1}{\lim_{q\to 0}\langle \hat{C}^+(q, \Omega)\rangle_{\Omega}}. \tag{7.10}$$

For hard spherocylinders with length L much larger than diameter D, the second-virial approximation is very accurate, and in fact becomes exact as $L/D \to \infty$ [5, 160]. The closure is then given by $\hat{C}^+(q, \Omega_{12}) = \hat{f}^+(q, \Omega_{12})$, where the Fourier transform of $\hat{f}$ is the connectedness Mayer function

$f^+(\mathbf{r},\Omega_{12}) = \exp(-\beta U^+(\mathbf{r},\Omega_{12}))$, with β the inverse thermal energy, and U^+ the connectedness pair potential [170, 173], which can be written as

$$\beta U^+(\mathbf{r},\Omega_{12}) = \begin{cases} 0, & 1 \text{ and } 2 \text{ are connected;} \\ \infty, & \text{otherwise,} \end{cases} \tag{7.11}$$

where we adopt the so-called core-shell model [174]. This consists of defining two particles as connected if their shortest surface-to-surface distance is less than connectedness criterion Δ, i.e., their shells of diameter $D+\Delta$ overlap, but an overlap of the hard cores of diameter D is forbidden ($\beta U^+ = \infty$). Note that a connected configuration has $f^+ = 1$ and disconnected one has $f^+ = 0$.

Here we also use the Parsons-Lee correction [175, 176], which effectively includes the higher order virial coefficients to make the second-virial theory more accurate for particles with smaller aspect ratios [163, 177]. This correction consists of using the closure $\hat{C}^+(q,\Omega_{12}) = G(\eta)\hat{f}^+(q,\Omega_{12})$, where $G(\eta) = (1-3\eta/4)/(1-\eta)^2$ [see Appendix C] with packing fraction $\eta = \rho\, v_0$ and v_0 the single particle volume. This closure has been shown to give good agreement with simulations for the percolation threshold of moderate aspect ratio hard spherocylinders ($L/D \gtrsim 10$) [177]. Now combining this closure with Eq. (7.10), we obtain for the percolation packing fraction [177]

$$\eta_P = \frac{2(1+2A-\sqrt{1+A})}{3+4A} \tag{7.12}$$

with

$$A = \frac{v_0}{\langle \hat{f}^+(0,\Omega)\rangle_\Omega}, \tag{7.13}$$

where $\hat{f}^+(0,\Omega) = \lim_{q\to 0}\hat{f}^+(q,\Omega)$.

Equation (7.13) together with the connectedness pair potential in Eq. (7.11) can be calculated for a fixed particle shape and connectedness criterion Δ. Our approach [29, 65], relies on Monte Carlo integration of the overlap volume using a large number of two-particle configurations. For all results presented here, we use ten independent runs of 10^9 Monte Carlo steps, which we found to provide high accuracy even for the largest aspect ratios ($L = 100D$) studied, with a typical relative standard error associated with the average overlap volume much smaller than 1%.

The first particle model we consider is a kinked spherocylinder, shown in Fig. 7.1(a), made up of two spherocylinders of lengths L_1 and L_2 and identical diameter D which are joined at an angle χ. The second particle, shown in Fig. 7.1(b), models a bent rod, which consists of a set of rigidly-connected, tangent beads along a circular arc, with end tangents given by angle χ and with contour length $L_c = N_s D$, where D is the diameter of the spheres and N_s the number of spheres.

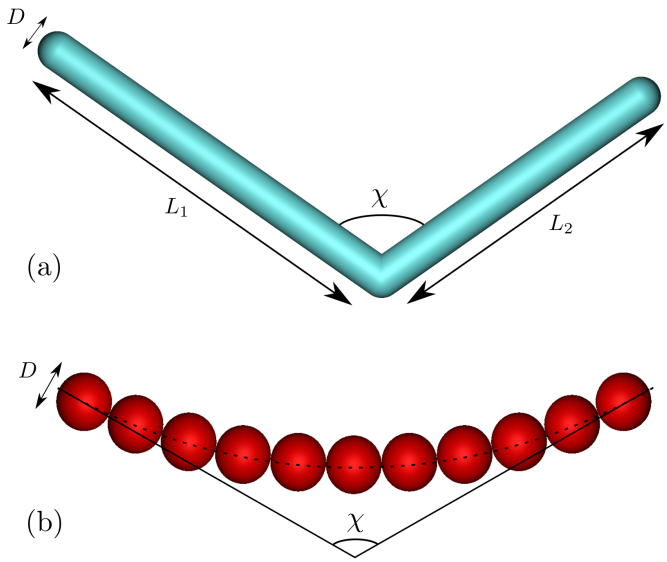

Figure 7.1.: (a) Our model of a kinked rod consisting of two spherocylinders joined at one end with an interarm angle of χ, arm lengths L_1 and L_2, and diameter D. (b) Our model of a bent particle, which consists of N_s connected spheres with diameter D positioned along a circular arc defined by the angle of the end tangents χ.

For the kinked rods, the single particle volume decreases slightly as χ becomes small but nonzero, as the two arms start to intersect. Therefore we have used Monte Carlo integration to determine the single particle volume, which is shown for various arm lengths L_1 and L_2 as a function of χ in Fig. 7.2.

In Sec. 7.3, we apply connectedness percolation theory to our models of kinked and bent rods, for various particle aspect ratios and deformations χ.

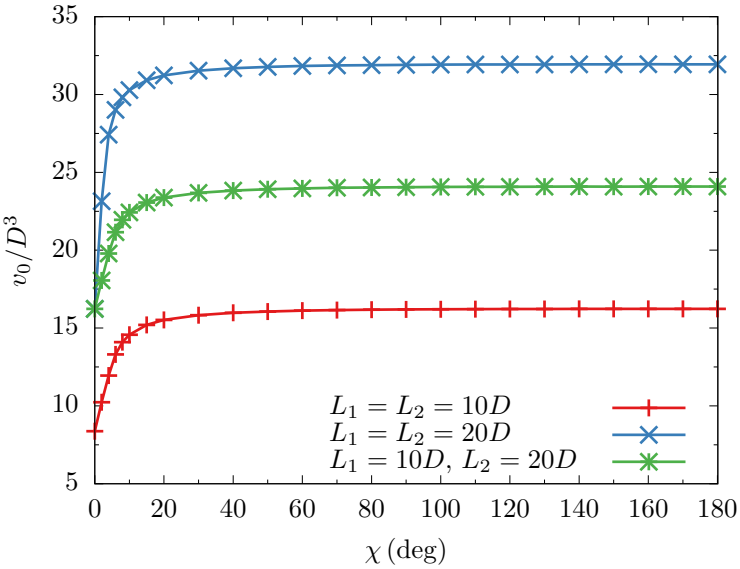

Figure 7.2.: Single particle volume v_0 (normalized by diameter D^3) of a kinked rod as a function of opening angle χ, with various arm lengths L_1 and L_2.

7.3. Results

We now show our results for the kinked rod model. Here we are interested in how the percolation packing fraction η_P depends on the kink location and kink angle, and if the long-rod scaling is affected. As is the case for straight rods, we expect the percolation packing fraction to also depend on aspect ratio and connectedness criterion Δ. For comparison, we use the analytical form of the percolation packing fraction for straight rods, that is, spherocylinders with length L and diameter D, which in the Parsons-Lee second-virial approximation is given by Eq. (7.12) with [5, 174]

$$A = v_0^{\mathrm{rod}} \left[\frac{\pi}{2} L^2 (D+\Delta) + 2\pi L (D+\Delta)^2 + \frac{4}{3}\pi (D+\Delta)^3 - \left(\frac{\pi}{2} L^2 D + 2\pi L D^2 + \frac{4}{3}\pi D^3 \right) \right]^{-1}, \tag{7.14}$$

with the single particle volume of a spherocylinder $v_0^{\mathrm{rod}} = \pi L D^2/4 + \pi D^3/6$.

In Fig. 7.3, we show the percolation packing fraction η_P as a function of the connectedness criterion (normalized by the rod diameter) Δ/D for

arm lengths $L_1 = L_2 = 20D$ and for various opening angles χ. Here we add the analytical results from Eq. (7.14) (dashed curves) for comparison in the two limiting cases of $\chi = 180°$, where the kinked rod reduces to a straight rod of length $L = 40D$ and $\chi = 0°$, where it reduces to a rod of length $L = 20D$. First we note that our numerical results are in good agreement with the analytical results from Eq. (7.14) in these limiting cases. As in the case of the straight rods, we see that the percolation threshold for kinked rods decreases monotonically with the connectedness criterion Δ.

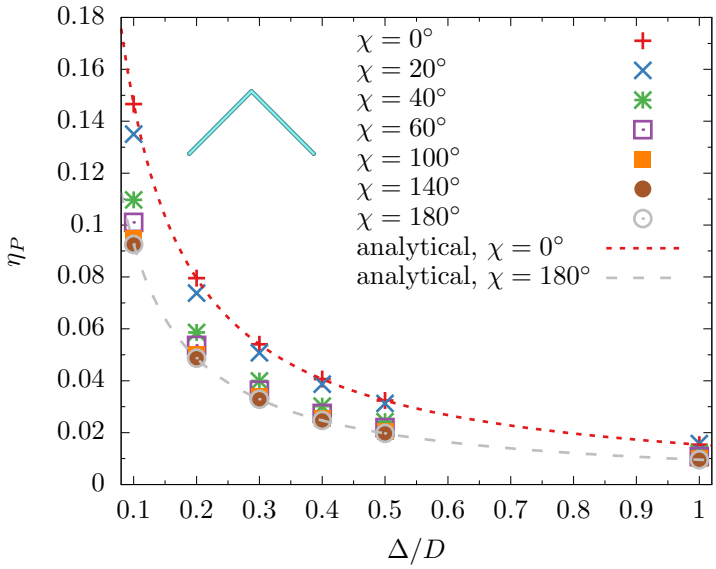

Figure 7.3.: Percolation packing fraction η_P of kinked rods as a function of connectedness criterion Δ/D for fixed arm lengths $L_1 = L_2 = 20D$ and for various opening angles χ. For comparison, the analytical results for straight spherocylinders are also plotted (dashed curves). Inset illustration shows the particle with $\chi = 90°$.

In order to more clearly see the angular dependence, in Fig. 7.4 we plot the percolation packing fraction as a function of angle χ for fixed values of the connectedness criterion Δ/D, again for $L_1 = L_2 = 20D$. Interestingly, we see that for small or even moderate deviations from straight rod shape ($\chi \geq 100°$) there is almost no change (less than a 5% increase) in the percolation threshold. Only at large deformations $\chi \sim 40°$ we see a visible increase in the percolation threshold, which becomes on the order of a 50% increase for $\chi = 20°$. We can explain this increase in the percolation threshold as due to a decrease in available connected volume, since the effective aspect

ratio of the particles is significantly decreased. Going from $\chi = 20°$ to $\chi = 0°$, there are two competing effects: first that the aspect ratio is further decreased and so η_P increases, and second that the single-particle volume decreases as the particle arms overlap (see Fig. 7.2), which decreases η_P.

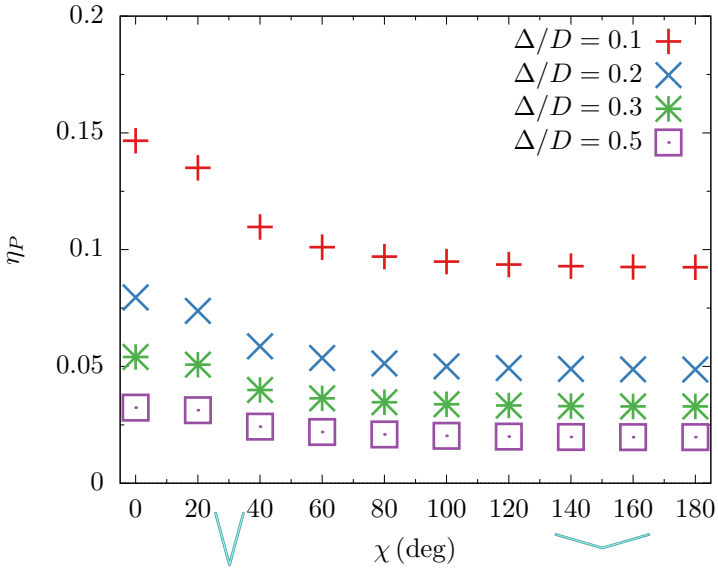

Figure 7.4.: Percolation packing fraction η_P of kinked rods as a function of opening angles χ for fixed arm lengths $L_1 = L_2 = 20D$ and for various connectedness criteria Δ/D. Illustrations along the horizontal axis show the particle shape for a given angle.

Next we study the dependence on kink location, for a fixed total rod length of $L_1 + L_2 = 40D$ and a fixed connectedness criterion $\Delta/D = 0.2$. In Fig. 7.5(a), we show the percolation packing fraction η_P vs. the kink location $L_1/(L_1 + L_2)$ for various angles χ. For kink location $L_1/(L_1 + L_2) \approx 0$, as expected, η_P cannot depend on angle χ. In fact, we see that the greatest deviation from straight rod behavior is for a central kink ($L_1/(L_1+L_2) = 0.5$). In Fig. 7.5(b), we plot the percolation threshold as a function of the kink angle χ for different values of the kink location $L_1/(L_1+L_2)$. This illustrates again that for small deformations $\chi \lesssim 180°$, there is very little effect on the percolation threshold η_P. The percolation threshold increases as the kink angle decreases towards $\chi \approx 20°$, which in the case of a central kink is about a 50% increase compared with $\chi = 180°$. The maximum in the percolation threshold for some kink locations in Fig. 7.5(b) is caused by the decrease in

the single-particle volume between $\chi = 20°$ and $\chi = 0°$ (see Fig. 7.2), which in turn decreases the percolation threshold.

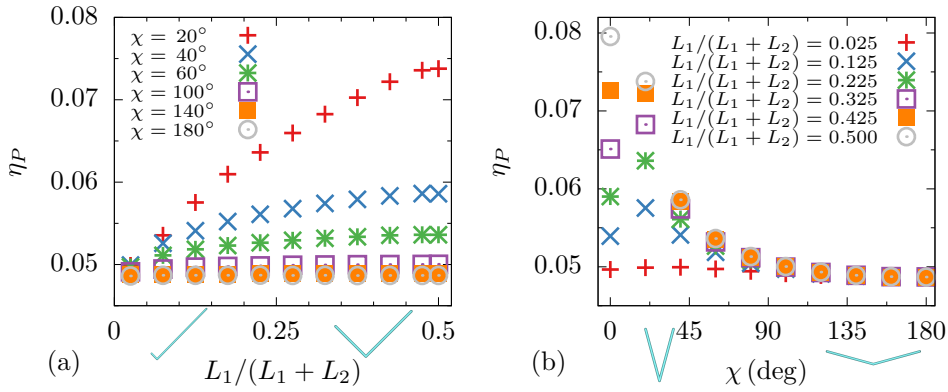

Figure 7.5.: Percolation packing fraction η_P of kinked rods with fixed total length $L_1 + L_2 = 40D$ and connectedness criterion $\Delta/D = 0.2$, (a) as a function of kink position ($L_1/(L_1 + L_2)$) for various kink angles χ and (b) as a function of kink angle for various kink positions. Illustrations along the horizontal axis show (a) the corresponding particle shape for $\chi = 90°$ and (b) the variation of the angle for $L_1/(L_1 + L_2) = 0.5$.

Finally, we want to examine the shape dependence of the large aspect ratio scaling behavior. As we can see from Eq. (7.14), for straight rods in the limit $L \gg D, \Delta$, we have that $\eta_P \to D^2/(2L\Delta)$. Therefore we multiply η_P by $2L\Delta/D^2$, such that for straight rods it approaches unity in the large aspect ratio limit. In Fig. 7.6, we show the scaled percolation thresholds as a function of the aspect ratio for many parameters in one plot. Here the kink angle dependence is shown by the colors: red ($\chi = 20°$), blue ($\chi = 60°$), and green ($\chi = 100°$). We also vary the connectedness criterion and the kink location, with $\Delta/D = 0.1$ given by the empty symbols and $\Delta/D = 1.0$ given by the filled symbols, and with the circles representing a central kink ($L_1 = L_2$) and the squares and triangles showing two asymmetric cases ($L_1 = 0.5L_2$ and $L_1 = 0.2L_2$ respectively). For comparison we plot the analytical results for straight rods of length $L_1 + L_2$ with $\Delta/D = 0.1$ (solid) and $\Delta/D = 1.0$ (dashed). Strikingly, we see that even for relatively large deformations of up to $\chi = 60°$, there is only a very small deviation from straight-rod asymptotic behavior, not exceeding 10% for $L_1 + L_2 \geq 80D$, which is true for any kink location or connectedness criteria. Only in the most extreme deformation considered here, $\chi = 20°$, do we see larger deviations, on the order of 35%

as $(L_1 + L_2)/D$ becomes large. For these small angles χ, some χ-dependent corrections to the straight-rod scaling must be important. Of course, this is to be expected since the relevant aspect ratio is no longer $(L_1 + L_2)/D$ when χ becomes small. We also note that this extreme case of $\chi = 20°$ is most likely not the most relevant case for real experimental systems.

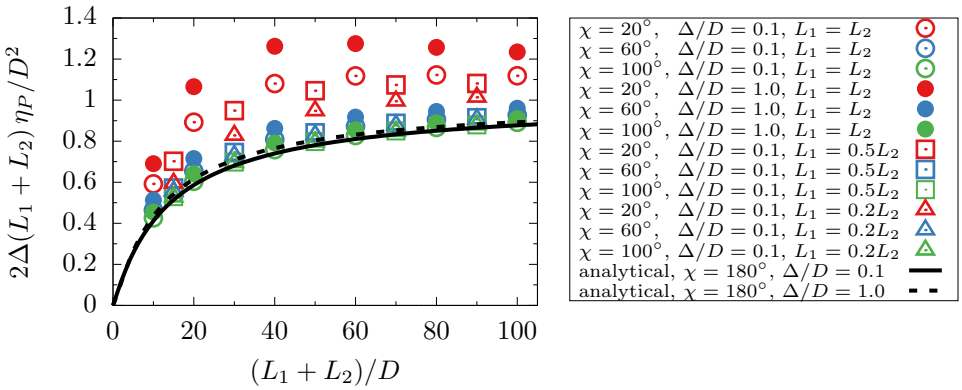

Figure 7.6.: Percolation packing fraction η_P [scaled by $2\Delta(L_1 + L_2)/D^2$] as a function of total length $(L_1 + L_2)/D$ for kinked rods with arms $L_1 = L_2$ (circles), $L_1 = 0.5L_2$ (squares), and $L_1 = 0.2L_2$ (triangles), with connectedness criterion $\Delta/D = 0.1$ (empty symbols) and $\Delta/D = 1.0$ (filled symbols), and for opening angles $\chi = 20°$ (red), $\chi = 60°$ (blue), and $\chi = 100°$ (green). The curves show analytical results for straight rods of length $L_1 + L_2$, with $\Delta/D = 0.1$ (solid) and $\Delta/D = 1.0$ (dashed).

Now we consider the second model described in Sec. 7.2, namely of a bent rod, modeled by a bead chain along a circular arc [see Fig. 7.1(b)]. As we have already discussed in detail the effect of varying the aspect ratio for the kinked rod model, here we restrict ourselves to varying χ for a bent rod consisting of $N_s = 11$ tangent spheres of diameter D, with contour length $L_c = 11D$. The bend angle χ [as illustrated in Fig. 7.1(b)] can vary from $\chi = 180°$ (straight rod) to $\chi = 0°$ (half circle).

As before, we first consider the percolation packing fraction η_P as a function of connectedness criterion Δ for various angles χ (Fig. 7.7). As for a straight rod, η_P decreases monotonically with increasing Δ, for all χ. We plot in Fig. 7.8 the percolation threshold as a function of the bend angle χ, for various Δ/D and see that deforming a straight rod ($\chi = 180°$) into a half circle ($\chi = 0°$) has no visible effect at all on the percolation threshold. This suggests that bending fluctuations also have a very small

effect on the percolation threshold [158]. This result is consistent with the behavior of the kinked rods as they vary from $\chi = 180°$ to $\chi = 90°$. We emphasize that the two particle shapes have different definitions of χ as shown in Fig. 7.1, with the bent particles being less deformed at $\chi = 0°$, where they are more comparable in shape to a kinked rods with $\chi = 90°$. In the following section we give a summary of our findings and an outlook on future research directions.

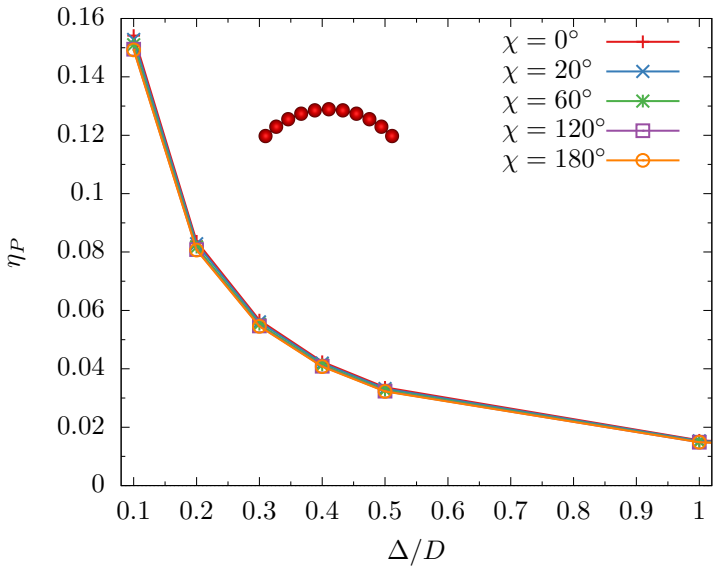

Figure 7.7.: Percolation packing fraction η_P of bent rods with fixed number of spheres $N_s = 11$ as a function of connectedness criterion Δ/D for various bend angles χ. Inset illustration shows the particle shape for $\chi = 90°$.

7.4. Discussion and conclusions

In this chapter, we have used connectedness percolation theory with the Parsons-Lee second-virial closure to study kinked and bent rodlike nanofillers. We calculated the percolation threshold, which is inversely proportional to an average overlap volume, using Monte Carlo integration. We have shown that the percolation threshold is only very weakly affected by small or even moderate rod shape deformations. For larger deformations, we saw a small increase in the percolation threshold. In addition, the universal scaling with

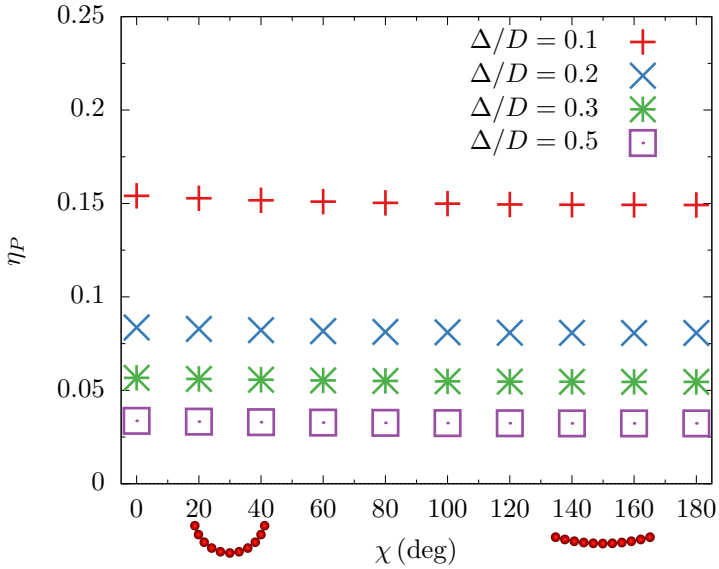

Figure 7.8.: Percolation packing fraction η_P of bent rods with fixed number of spheres $N_s = 11$ as a function of bend angle χ for various connectedness criteria Δ/D. Illustrations along the x-axis show the particle shape for a given angle.

particle aspect ratio and connectedness criterion was only affected for very deformed particles, which can be seen as due to an effective reduction in the aspect ratio.

Our approach of combining connectedness percolation theory with Monte Carlo integration is able to deal with any complicated particle shape provided that one has a two-particle overlap algorithm. It is exact in the large aspect ratio limit and since it uses the Parsons-Lee correction, we also expect it to be reasonably accurate for moderate aspect ratios, though more work is needed to understand this correction's applicability to non-rodlike particle shapes. We note that the only effect of the Parsons-Lee correction is to shift the percolation threshold to lower packing fractions. The qualitative behavior we find is completely unchanged by adding this correction.

Although previous works have not considered the explicit dependence on a kink or bend deformation, several studies have dealt with the effect of waviness on the percolation threshold of long rods. Based on the theory of fluids of flexible rods, it has been predicted that a finite bending flexibility weakly increases the percolation threshold since the bending effectively decreases the length [158]. There have been several results from simulations that

also find a weak increase in the percolation threshold due to flexibility or waviness [166, 178, 179]. Notably, in Ref. [178], randomly oriented wavy fibers with different curvatures were studied through both simulations and excluded volume calculations. Here it was found that in the large aspect ratio limit, the percolation threshold of wavy rods was comparable to but slightly larger than that of straight rods [178].

The fact that moderate kinks in long rods do not affect their percolation threshold can be understood qualitatively by an argument similar to the one given in Ref. [96] and also the basis for a common approximation used in, e.g., Refs. [79, 95]. Recall that in the long-rod limit $L \gg D$ and $L \gg \Delta$, the inverse percolation density, which is also the connectedness version of the average excluded volume, is $\rho_P^{-1} = \langle \hat{f}^+(0,\Omega)\rangle_\Omega = \pi L^2 \Delta/2$. Suppose that we consider each rod as consisting of two segments of length $L/2$, core diameter D, and shell diameter $D+\Delta$, then the average excluded volume can be written as the sum of the average segmentwise excluded volumes $\rho_P^{-1} = 4\pi(L/2)^2\Delta/2$. This yields the same result as for the original rods and is still exact in the long rod limit, since we ignore end effects. Now, consider that the two segments of the rods are joined at some angle χ. As before, we can write the excluded volume as a sum of the segmentwise excluded volumes, which implies that the percolation threshold is the same as for a straight rod. However, this is no longer exact, and in fact it becomes a worse approximation as the rods become more deformed. This is because it becomes more probable for two rods to have a simultaneous overlap of both pairs of segments and so the segmentwise excluded volume overestimates the true overlap volume [93]. Therefore this qualitative argument only applies to moderately deformed rods.

In the future, it would be interesting to examine the structures of the clusters of kinked and bent rods, as well as their percolation thresholds in the prolate, oblate, and biaxial nematic phases. Also, mixtures of deformed particles or polydisperse systems with defects would be an interesting future investigation.

Acknowledgments

First of all, we thank Paul van der Schoot for suggesting this project and for his collaboration on it. We also thank Simone Dussi for help on the Monte Carlo integration of the virial coefficients and Marjolein Dijkstra for helpful comments.

Chapter 8.

Connectedness percolation of polygonal rods and platelets

8.1. Introduction

Nanofillers dispersed in a polymeric medium can form in some sense connected networks above a critical density known as the percolation threshold. As a result, the physical properties of such composites relating to, e.g., elastic, electrical, and thermal response, change drastically if the filler fraction is increased to one or two times the percolation threshold. These types of composite materials have many interesting applications, possibly including the replacement for indium-tin oxide as a transparent electrode [156, 157]. To preserve transparency, however, it is desirable to have an extremely low percolation threshold, and so understanding what factors determine this is of practical as well as fundamental interest.

Using theory and simulations, studies have been performed on how the percolation threshold depends on particle aspect ratio [5, 168, 177, 180, 181], polydispersity [158–163, 182–185], attractive interactions [158], clustering [186, 187], and alignment [164, 165, 188–190]. In these studies, nanofiller particles are usually modeled as perfect rods, disks, or ellipsoids. In Chapter 7, we studied one type of shape deformation, namely rodlike nanofillers with kink or bend defects, and found very little effect on the percolation threshold up to moderate deformations. However, real nanofillers may have many other types of shape irregularities. For example, graphene sheets, while having very high aspect ratios with a diameter of 1μm and thickness of a few angstroms, also have quite irregular shapes, with sharp corners and high variability between flakes [191–193]. Cellulose nanocrystals, another example of a promising material, can be coated with a conductive polymer to form composites with a very low percolation threshold [194]. These

nanocrystals are not perfect cylinders, but rather have a rectangular cross section [195, 196].

In this chapter, we investigate how the percolation threshold depends on the precise particle cross section, for rodlike and platelike nanofiller particles. Using connectedness percolation theory in the second-virial approximation, we write the percolation threshold for convex particles in terms of three single particle measures, namely the volume, surface area, and mean half-width. We apply this formalism to systems of polygonal rods and platelets. We show that particle cross sections with fewer sides have lower percolation thresholds due to their increased surface area to volume ratio.

The remainder of the chapter continues as follows. In Sec. 8.2 we present our method for calculating the percolation threshold for convex particles in the isotropic phase. Particle models considered are shown in Fig. 8.1. In Sec. 8.3 we apply this method to systems of polygonal rods and platelets, and in Sec. 8.4 we conclude by summarizing and discussing our results.

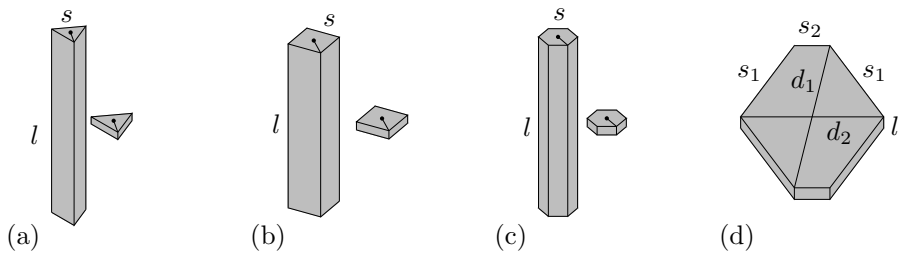

Figure 8.1.: Regular right polygonal prism models with n sides of length s, facial center-to-vertex length $d/2$, height l and with (a) $n = 3$, (b) $n = 4$, and (c) $n = 6$, with rodlike version ($l > d$) on left and platelike version ($l < d$) on the right. (d) Irregular equiangular right hexagonal platelet of height l, sides of s_1, s_2, and s_1, and with unique diameters d_1 and d_2.

8.2. Method

In this section, we calculate the percolation threshold using connectedness percolation theory [169, 170] within the second-virial approximation. The percolation packing fraction η_P is defined as the lowest packing fraction at which the average cluster size of connected particles diverges. We define two particles as connected if their surface-to-surface distance is less than a

certain connectedness criterion (or connectedness range) Δ. For electrical percolation, this connectedness criterion is related to the electron tunneling distance and depends on the nanofiller properties as well as the dielectric properties of the medium [158, 168].

We consider clusters composed of rigid, non-spherical particles with single-particle volume $\mathcal{V}$. The orientation of such a particle can be given by three Euler angles $\Omega = (\alpha, \beta, \gamma)$. Assuming a uniform spatial distribution of particles with number density ρ, the orientation distribution function $\psi(\Omega)$ is defined so that the probability to find a particle with an orientation Ω in the interval $d\Omega$ is given by $\psi(\Omega)d\Omega$, with the normalization constraint that $\int d\Omega\, \psi(\Omega) = \int_0^{2\pi} d\alpha \int_0^{\pi} d\beta \sin\beta \int_0^{2\pi} d\gamma\, \psi(\Omega) = 1$. The orientational average is denoted $\langle \ldots \rangle = \int d\Omega \ldots \psi(\Omega)$. In this chapter, we only consider percolation in the isotropic phase, where all orientations are equally probable and so $\psi(\Omega) = 1/(8\pi^2)$.

Within the second-virial closure, the percolation packing fraction is simply given by [158, 160, 170, 197]

$$\eta_P = \frac{\mathcal{V}}{\langle \hat{f}^+(0,\Omega) \rangle}, \tag{8.1}$$

with $\hat{f}^+(0,\Omega) = \lim_{q\to 0} \hat{f}^+(q,\Omega)$ where $\hat{f}^+(q,\Omega)$ is the Fourier transform of the connectedness Mayer function $f^+(\mathbf{r},\Omega)$. Here we denote the Fourier transform of an arbitrary function $g(\mathbf{r})$ by $\hat{g}(\mathbf{q}) = \int d\mathbf{r} g(\mathbf{r}) \exp(i\mathbf{q}\cdot\mathbf{r})$. For the derivation of Eq. (8.1) for arbitrarily shaped rigid particles, see Chapter 7, which follows the derivation for cylinders [158, 160]. Equation (8.1) is exact in the isotropic phase within the second-virial closure, and has a similar form to that of spherical nanofillers [170]. However, Eq. (8.1) is not exact in aligned phases unless the alignment is perfect. Interestingly, Eq. (8.1) can also be derived from a random geometric graph approach under the assumption that the node degrees (particle contact numbers) are Poisson distributed [198, 199].

The connectedness Mayer function is defined as [170, 173]

$$\begin{aligned} f^+(\mathbf{r},\Omega_{AB}) &= \begin{cases} 1, & \text{A and B are connected;} \\ 0, & \text{otherwise,} \end{cases} \\ &= f^{\text{shell}}(\mathbf{r},\Omega_{AB}) - f^{\text{core}}(\mathbf{r},\Omega_{AB}), \end{aligned} \tag{8.2}$$

where

$$f^{\text{shell}}(\mathbf{r}, \Omega_{AB}) = \begin{cases} 1, & \text{A and B have overlapping shells;} \\ 0, & \text{otherwise,} \end{cases}$$

and

$$f^{\text{core}}(\mathbf{r}, \Omega_{AB}) = \begin{cases} 1, & \text{A and B have overlapping cores;} \\ 0, & \text{otherwise.} \end{cases}$$

Here $\mathbf{r}$ is the vector connecting the centers of the two particles and Ω_{AB} is the relative orientation between particles A and B. This is the so-called core-shell model [174], where we define two particles as connected if their shortest surface-to-surface distance is less than the connectedness criterion Δ, i.e., their shells overlap, but an overlap of the hard cores is forbidden. The connectedness Mayer function is $f^{+} = 1$ for a connected configuration and $f^{+} = 0$ disconnected one. In addition, we will consider the less realistic but simpler model of "ghost" particles, which are ideal particles without a hard core. In this model, particles are defined by the shape and size of their shells, and are connected if their shells overlap.

We define the connectedness volume as the spatial integral of the connectedness Mayer function as $\mathcal{E}^{+}(\Omega_{AB}) = \hat{f}^{+}(0, \Omega_{AB})$. From integrating Eq. (8.2) over separation $\mathbf{r}$ and relative orientations Ω_{AB}, we obtain the average connectedness volume in the isotropic phase as

$$\langle \mathcal{E}^{+}_{AB} \rangle = \langle \mathcal{E}^{\text{shell}}_{AB} \rangle - \langle \mathcal{E}^{\text{core}}_{AB} \rangle, \tag{8.3}$$

where we dropped the Ω argument of the averaged $\mathcal{E}$ for simplicity.

We now invoke a striking result from integral geometry, which relates the orientationally-averaged excluded volume of two arbitrary convex bodies A and B to their three single-particle invariant measures as [200, 201]

$$\langle \mathcal{E}_{AB} \rangle = \mathcal{V}_A + \mathcal{S}_A \mathcal{M}_B + \mathcal{S}_B \mathcal{M}_A + \mathcal{V}_B, \tag{8.4}$$

where $\mathcal{V}_\alpha$ denotes the volume, $\mathcal{S}_\alpha$ the surface area, and $\mathcal{M}_\alpha$ the mean half-width of a *single* particle of species α. For a recent work on integral geometry applied to the excluded volume of hard bodies see Ref. [11]. The mean

half-width of a convex polyhedron C is given by [11]

$$\mathcal{M}_C = \frac{1}{8\pi} \sum_{E_i} |E_i| \phi_i, \tag{8.5}$$

where $|E_i|$ is the length of edge E_i and ϕ_i is the angle between the normals of the faces that meet at E_i.

So for a given convex body A, which consists of a core body A_{core} and a shell body A_{shell}, and similarly for B, we can calculate the connectedness excluded volume and thus the percolation threshold, given that we can calculate the volume, surface area, and mean half-width of the core and shells of A and B. Here we restrict ourselves to the monodisperse case, where $A = B$. In this case Eq. (8.4) reduces to

$$\langle \mathcal{E} \rangle = 2\mathcal{V} + 2\mathcal{S}\mathcal{M}, \tag{8.6}$$

where we drop the subscript A for convenience. Now a particle in the core-shell model is defined by the three geometric properties of its core ($\mathcal{V}_c$, $\mathcal{S}_c$, $\mathcal{M}_c$) and of its shell ($\mathcal{V}_s$, $\mathcal{S}_s$, $\mathcal{M}_s$), where the subscripts c and s denote core and shell, respectively. Using Eqs. (8.1), (8.3), and (8.6), this gives for the percolation threshold in the core-shell model

$$\eta_P = \frac{1}{2(\mathcal{V}_s/\mathcal{V}_c + \mathcal{S}_s\mathcal{M}_s/\mathcal{V}_c - 1 - \mathcal{S}_c\mathcal{M}_c/\mathcal{V}_c)}. \tag{8.7}$$

We will also consider ghost particles (with vanishing cores), where a particle is defined by the three geometric properties of its shell ($\mathcal{V}_s$, $\mathcal{S}_s$, $\mathcal{M}_s$). Within the ghost model, the percolation threshold has the even simpler form of

$$\eta_P^{\text{ghost}} = \frac{1}{2(1 + \mathcal{S}_s\mathcal{M}_s/\mathcal{V}_s)}, \tag{8.8}$$

which shows that the percolation threshold only depends on the dimensionless combination of single particle properties, namely $\mathcal{S}_s\mathcal{M}_s/\mathcal{V}_s$. Note that in the ghost model [Eq. (8.8)] the percolation packing fraction [Eq. (8.1)] is defined using the shell volume $\mathcal{V} = \mathcal{V}_s$, whereas in the core-shell model [Eq. (8.7)] the core volume $\mathcal{V} = \mathcal{V}_c$ is used.

The second-virial approximation is known to be very accurate for rodlike particles with high aspect ratios [5, 160]. For rodlike particles with a smaller aspect ratio, the Parsons-Lee correction can be used to effectively include

higher order virial coefficients [163, 175–177]. For moderate aspect ratio hard spherocylinders (with length L, diameter D, and $L/D \gtrsim 10$), this correction has been shown to give good results [177]. Although there is no rigorous argument for applying this correction to shapes besides spherocylinders, it has given good agreement with Monte Carlo results for the equation of state for the less symmetric hard "boomerang" (bent-core) particles [81]. However, as this factor is only a rescaling of the second virial results and does not change the qualitative behavior, for simplicity we will not use it here.

Far away form Onsager's needle limit, e.g., for short rodlike or for platelike particles, it would be desirable to include higher order virial terms, however, this is often computationally impractical. A method that is known to be highly accurate and that better captures angular correlations, is the so-called fundamental measure theory (FMT) [202]. Although it was originally developed for spheres [203, 204], it has recently been applied to many hard bodies systems including rod/sphere mixtures [205], rodlike particles with various cross-sections [117], as well as boardlike particles [119], however, in the latter two works the particles were not freely rotating. It would be desirable to use FMT to study percolation, however, such a theory has yet to be formulated.

Surprisingly, second-virial theory seems to have predictive power in systems of flat rather than elongated particles. For example, it gave the same phase diagram topology as FMT when applied to binary mixtures of disks [206]. The percolation threshold from second-virial theory was also in qualitative agreement with Monte Carlo calculations for spheres with a small hopping distance [207] as well as Monte Carlo calculations for very thin oblate ellipsoids [184]. In addition, it has been shown from random graph theory that hard spheres with a thin connectedness shell form connected networks with a tree-like structure, indicating third and higher virial terms can be neglected [208]. In light of these results, we here also apply second-virial theory to systems of platelets.

8.3. Results

In Sec. 8.3.1, we calculate the percolation thresholds for rodlike nanofillers with various cross-sections, the rectangular ones being potentially relevant to (coated) cellulose nanocrystals. Then, in Sec. 8.3.2, we consider platelike nanofillers, with an emphasis on regular and irregular hexagonal platelets which resemble graphene flakes.

8.3.1. Regular right polygonal prisms

First, we consider regular right polygonal prisms with n sides on their polygonal faces [see Fig. 8.1(a-c)]. We characterize these by the length of the prism l_n and the length of the polygonal side s. The facial diameter, which we define as twice the center-to-vertex distance of the polygon (or equivalently, the diameter of the circle circumscribing the face), is then given by $d_n = s/\sin(\pi/n)$. The single-particle core properties are simply given by

$$\mathcal{V}_c = \frac{1}{8} l_n d_n^2 n \sin\left(\frac{2\pi}{n}\right), \tag{8.9}$$

for the volume,

$$\mathcal{S}_c = \frac{1}{4} d_n^2 n \sin\left(\frac{2\pi}{n}\right) + l_n d_n n \sin\left(\frac{\pi}{n}\right), \tag{8.10}$$

for the surface area, and

$$\mathcal{M}_c = \frac{1}{8} d_n n \sin\left(\frac{\pi}{n}\right) + \frac{1}{4} l_n, \tag{8.11}$$

for the mean half-width. It can be easily checked that the limit $n \to \infty$ returns the correct properties for cylinders, i.e.,

$$\mathcal{V}_{c,\mathrm{cyl}} = \frac{\pi}{4} l d^2, \tag{8.12}$$

for the volume,

$$\mathcal{S}_{c,\mathrm{cyl}} = \frac{\pi}{2} d^2 + \pi l d, \tag{8.13}$$

for the surface area, and

$$\mathcal{M}_{c,\mathrm{cyl}} = \frac{\pi}{8} d + \frac{1}{4} l. \tag{8.14}$$

for the mean half-width. Similarly, we can write the shell properties by letting $d_n \to d_n + \Delta$ and $l_n \to l_n + \Delta$, where Δ is the connectedness criterion. Note that in the case of the ghost model, particles only have a shell and no core so we set $\Delta = 0$ in that case.

Now, we compare the percolation thresholds of the n-sided rods to that of cylinders. We choose to compare hard prisms of the same volume and same aspect ratio l_n/d_n. This amounts to setting $d_n = 2\mathcal{V}^{1/3}[l_n/d_n \cdot n \sin(2\pi/n)]^{-1/3}$ where we use $\mathcal{V} = \mathcal{V}_c$ as the unit of volume for the core-shell model and $\mathcal{V} = \mathcal{V}_s$ for the ghost model.

For cylinders in the ghost model, the needle-limit $l/d \to \infty$ leads to $\eta_P^{\text{ghost}} \to d/(2l)$. Similarly, in the core-shell-model, the asymptotic behavior of cylinders is $\eta_P \to d^2/(2l\Delta)$. By inspecting the formulas for polygonal rods, we can determine the long-rod ($l/d \to \infty$) limits of the percolation threshold for the polygonal rods, which we find to be

$$\eta_P^{\text{ghost}} \to \frac{d_n \cos(\pi/n)}{2l_n}, \tag{8.15}$$

for the ghost model, and

$$\eta_P \to \frac{d_n^2 \cos(\pi/n)}{2l_n\Delta}, \tag{8.16}$$

for the core-shell model, which return the correct results for cylinders ($n \to \infty$). Since $\cos(\pi/n)$ for $n \geq 3$ is a monotonically increasing function, in the asymptotic limit $l_n/d_n \to \infty$, clearly η_P increases with n.

In Fig. 8.2, we show the scaled percolation packing fraction as a function of aspect ratio l_n/d_n, for (a) the ghost model and (b) the core-shell model, scaled by the asymptotic η_P dependence of cylinders, i.e., (a) $2l_n/d_n$ and (b) $2l_n\Delta/d_n^2$. Here we can clearly see the n-dependence found in Eqs. (8.15)-(8.16). Figures 8.2(a) and (b) show that reshaping a cylinder (with fixed volume) into a triangular ($n = 3$), rectangular ($n = 4$), or hexagonal ($n = 6$) prism lowers the percolation threshold by a factor $\sec(\pi/n) = 2, \sqrt{2}, 2/\sqrt{3}$ respectively. This interesting effect is qualitatively similar within both models and can most easily be understood by considering the simpler expression found for the ghost model in Eq. (8.8). At fixed volume, the lowest percolation threshold is found by maximizing the surface area times the mean half-width. In fact, both the surface area and the mean half-width increase with decreasing n, with $n = 3$ (triangular prisms) yielding the minimal percolation threshold for the polygonal rods studied here.

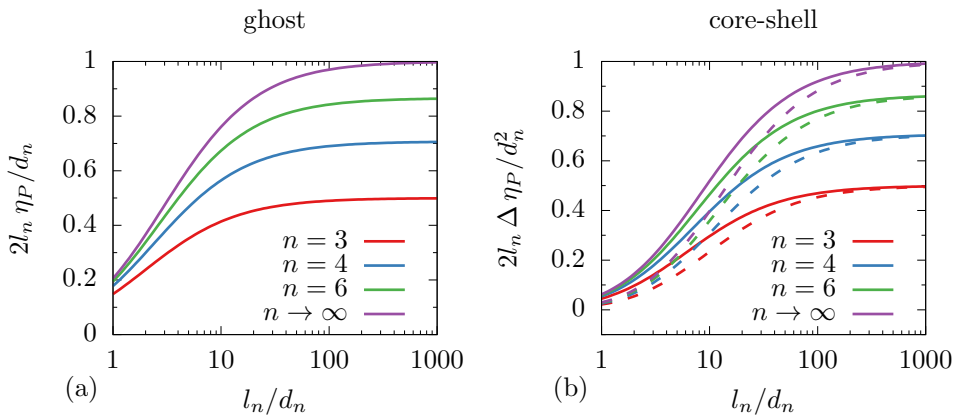

Figure 8.2.: Scaled percolation packing fraction η_P of polygonal rods as a function of the aspect ratio l_n/d_n for (a) the ghost model and (b) the core-shell model, for various numbers of polygonal sides n, where the case of $n \to \infty$ corresponds to cylinders. The asymptotic factor used to scale the percolation threshold is (a) $2l_n/d_n$ and (b) $2l_n\Delta/d_n^2$. In (b) the connectedness criterion is $\Delta/d_n = 0.1$ (solid curves) and $\Delta/d_n = 1.0$ (dashed curves).

8.3.2. Right polygonal platelets

We now turn our attention to platelets [see Fig. 8.1(a-d)]. We compare regular polygonal platelets and irregular hexagonal platelets to disks, in order to see the effect of shape on the percolation threshold. In the limit that $d_n \gg \Delta, l_n$, we find that for n-sided regular platelets

$$\eta_P^{\text{ghost}} \to \frac{2l_n}{d_n n \sin(\pi/n)}, \tag{8.17}$$

for the ghost model and

$$\eta_P \to \frac{2l_n g(n)}{\Delta}, \tag{8.18}$$

for the core-shell model and where for convenience we introduced $g(n) = (2n\tan(\pi/n) + 3n\sin(\pi/n) + 6)^{-1}$ on the right-hand side of Eq. (8.18). Strikingly, we see that in the core-shell model, the asymptotic percolation threshold is independent of the diameter d_n, which is in agreement with simulations of platelets [209]. In the cylindrical disk limit $n \to \infty$, $\eta_P^{\text{ghost}} \to 2l_n/(\pi d_n)$

and for the core-shell model $\eta_P \to 2l_n/(6\Delta + 5\pi\Delta)$, in agreement with other works [160]. Whereas the ghost model's asymptotic percolation threshold [Eq. (8.17)] decreases with increasing n, the core-shell model's n dependence in the scaling factor, $g(n)$, is a monotonically increasing function of n. However, the core-shell model only has a weak dependence on n, in contrast with the rodlike limit. Here we see that reshaping a disk (with fixed volume) into a triangular ($n = 3$), rectangular ($n = 4$), or hexagonal ($n = 6$) platelet lowers the percolation threshold by a relatively small factor $[g(n)(6 + 5\pi)]^{-1} \approx 1.11, 1.04, 1.01$ respectively. In contrast with the case of rods, for platelets the ghost model does not give qualitatively similar behavior to the more realistic core-shell model.

For a comparison to an irregular shape, we use a hexagonal platelet that is an equiangular right prism with height l and sides s_1, s_1, and s_2 [see Fig. 8.1(d)]. The three corner-to-corner diagonals are then $d_1 = \sqrt{3s_1^2 + s_2^2}$, d_1, and $d_2 = s_1 + s_2$. The single particle measures (in terms of the sides s_1 and s_2) are given by

$$\mathcal{V}_c = \frac{\sqrt{3}}{2} l \left(s_1^2 + 2s_1 s_2\right), \tag{8.19}$$

for the volume,

$$\mathcal{S}_c = \sqrt{3}\left(s_1^2 + 2s_1 s_2\right) + 4ls_1 + 2ls_2, \tag{8.20}$$

for the surface area, and

$$\mathcal{M}_c = \frac{1}{4}(2s_1 + s_2 + l) \tag{8.21}$$

for the mean half-width. In the limit that $d_1, d_2 \gg \Delta, l$, the hexagonal platelet percolation threshold is

$$\eta_P^{\text{ghost}} \to \frac{l\left(-4 + 10x^2 + 6x\sqrt{4 - 3x^2}\right)}{d_1\left[x + 8x^3 + \left(10x^2 - 1\right)\sqrt{4 - 3x^2}\right]}, \tag{8.22}$$

for the ghost model and

$$\eta_P \to \frac{2\sqrt{3}l\left[-2 + x(5x + 3\sqrt{4 - 3x^2})\right]}{\Delta\left[h_1(x) + h_2(x, y)\right]}, \tag{8.23}$$

for the core-shell model, and where for convenience we define $x = d_2/d_1$, $y = \Delta/d_1$. We note that while the ratio between the sides has the range $s_2/s_1 \in [0, \infty)$, the ratio between the diameters has the range $x = d_2/d_1 \in [1/\sqrt{3}, 2/\sqrt{3}]$ where in the subrange $x \in (1, 2/\sqrt{3})$ there are two values of s_2/s_1 for each x. For simplicity and clarity here we limit ourselves to the solution with $s_2/s_1 \leq 3$.

We also define

$$h_1(x) = 8 - 11\sqrt{3} + 2\sqrt{3}\left(x - \sqrt{4 - 3x^2}\right) + 2x\left[\left(22 + 27\sqrt{3}\right)x + \left(10 + 19\sqrt{3}\right)\sqrt{4 - 3x^2}\right], \tag{8.24}$$

and

$$h_2(x, y) = \frac{\sqrt{3}}{y}\left(1 - 10x^2\right)\left(\sqrt{4 - 3x^2} - \sqrt{4 + 8y - 6xy + y^2 - 2x^2}\right). \tag{8.25}$$

Notably, the core-shell model has an asymptotic dependence on not only l/Δ but also the ratio between the two diameters x and $y = \Delta/d_1 = \Delta/l \cdot l/d_1$. As before, we set the core (shell) volume as our unit of volume for the core-shell (ghost) model, by setting $d_1 = \mathcal{V}^{1/3}[\sqrt{3}/32 \times l/d_1(-4 + 10x^2 + 6x\sqrt{4 - 3x^2})]^{-1/3}$.

In Fig. 8.3(a), we show the asymptotically scaled percolation threshold as a function of aspect ratio l/d_1 for the ghost model. Here we vary the irregularity of the hexagonal platelets by varying the ratio $x = d_2/d_1$ where $x = 1$ is a regular hexagonal platelet. From studying the x dependence in the limit $l/d_1 \to 0$ [Eq. (8.22)], we see that the percolation threshold is non-monotonic in x with the minimal η_P found when $x = 5/\sqrt{21} \approx 1.09$ and the maximal when $x = 1/\sqrt{3} \approx 0.58$. Within the ghost model we find that cylindrical disks have the minimal percolation threshold, with hexagonal platelets having a slight increase in η_P for $x = 1.0, 1.09, 1.15$ and a more pronounced increase for $x = 0.58, 0.75$.

In Fig. 8.3(b), we show the asymptotically scaled percolation threshold as a function of aspect ratio l/d_1 for the core-shell model, with two connectedness criteria $\Delta/l = 0.1, 1.0$. We see the scaled percolation threshold for thin platelets $l/d_1 \ll 1$ is only very slightly lower for regular hexagonal platelets ($x = 1$) compared with disks, as noted before. However, the percolation threshold decreases more significantly for the irregular hexagonal platelets with $x \neq 1$, with once again the percolation threshold having a non-monotonic

dependence on x. The lowest percolation threshold out of the platelets studied here is found for $x = 1.15$ (an elongated platelet with $s_2 = 3s_1$). However, we caution that although the second-virial theory has had predictive power in describing platelets, we cannot be certain that the approximation gives accurate results in this limit.

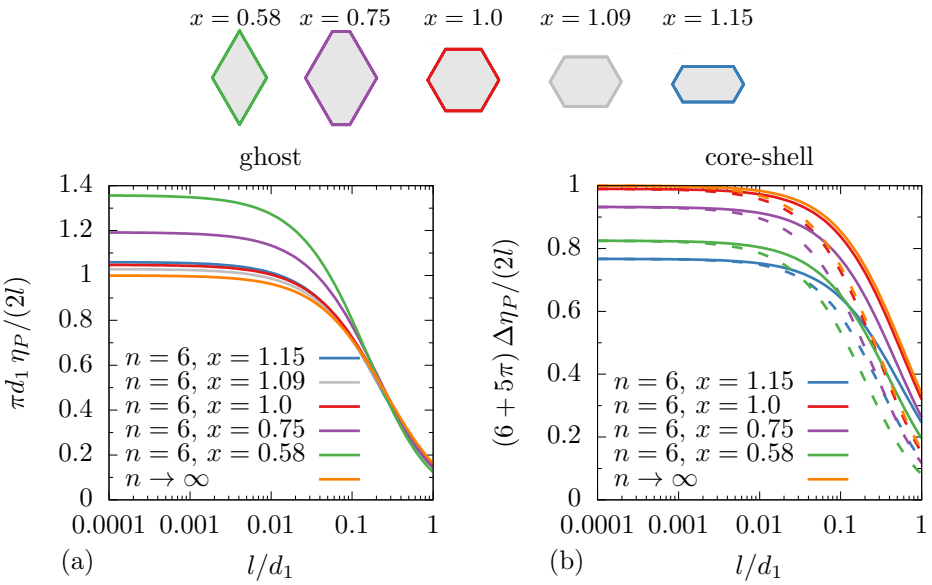

Figure 8.3.: Scaled percolation packing fraction η_P of hexagonal platelets ($n = 6$) with diameters d_1, d_2 and diameter ratio $x = d_2/d_1$ and disks ($n \to \infty$) with diameter d_1 as a function of the aspect ratio l/d_1 for (a) the ghost model and (b) the core-shell model for the connectedness criteria $\Delta/l = 0.1$ (solid curves) and $\Delta/l = 1.0$ (dashed curves). Illustration above figures shows the shape of the hexagonal face for various irregularities x.

8.4. Discussion and conclusions

In this chapter, we apply connectedness percolation theory within the second-virial approximation, together with a powerful result from integral geometry, to analytically calculate percolation thresholds of hard convex bodies in the isotropic phase. We find that at fixed single particle volume, the percolation threshold is minimized by maximizing the particle surface area (times the mean-half width).

We first apply this result to regular polyhedral rods, which may be relevant to, e.g., systems of cellulose nanocrystals which have a rectangular cross section. We find that the percolation threshold decreases with lowering the number of polygonal sides. The long-rod asymptotic scaling of the percolation threshold is lowered by a factor $\sec(\pi/n)$ with respect to cylinders of the same aspect ratio and volume, which for the case of rectangular prisms ($n = 4$) is a factor of $\sqrt{2} \approx 1.4$.

In addition, we compare regular and irregular hexagonal platelets to cylindrical disks, which are relevant to systems of graphene sheets. Within the core-shell model, we also find that the regular hexagonal platelets have a lower percolation threshold with respect to disks, although in the platelet limit the dependence on the number of sides is much weaker than in the rod limit. However, we find a larger effect on the percolation threshold for irregular hexagonal platelets which can have a significantly lowered percolation threshold due to their increased surface area. In the platelike limit, we emphasize that the ghost model no longer gives qualitatively similar behavior to the core-shell model.

Idealized cylindrical rod and disk models are often used to model real nanofillers, and the effect of the actual particle shape has largely been neglected. In Ref. [197], we recently studied the effect of kink and bend defects on systems of rodlike particles and found very little effect on the percolation threshold, up to moderate deformations. However, these deformations, unless extreme, did little to change the surface area of the particles. Therefore in light of the results presented here, this is not unexpected. In Ref. [210], the excluded volume was written using single-particle measures analogously to our "ghost" (ideal) model here, for various shapes such as rectangular prisms, cylinders, platonic solids, and spheroids. However, the authors' focus was on the scaling behavior of the percolation threshold as a function of the number of dimensions [210, 211] and not on the effect of the precise nanofiller cross section in three dimensions, as we examine here.

Although we restricted ourselves to fairly simple particle types, any hard convex body (in the isotropic phase) can be considered using this approach. In addition, this formalism is readily applicable to binary mixtures or polydisperse systems, as Eq. (8.4) gives the excluded volume between two arbitrarily shaped convex bodies. Furthermore, the form for the percolation threshold in the second-virial closure is known for bidisperse and polydisperse systems [159, 160]. This would be an interesting future step, as polydispersity is known to be very important in describing percolation [158–163, 182–185].

Acknowledgments

We thank Paul van der Schoot for suggesting this topic and for his collaboration on it. We also thank Bela Mulder, Simonas Grubinskas, Avik Chatterjee, and Claudio Grimaldi for helpful discussions.

Appendix A.

Rotations

In this appendix, we define the basic concepts of rotations and Euler angles, following Ref. [212]. A rotation transformation of a vector in $\mathbb{R}^3$ is defined by a rotation angle δ and a rotation axis $\hat{u}$. For a positive angle, the rotation is performed counterclockwise around the axis (following the right hand rule). There are two types of possible rotations: active and passive rotations. An active rotation $\mathcal{R}_{\hat{u}}^{(a)}(\delta)$ is the rotation of a vector in a fixed coordinate frame, whereas a passive rotation $\mathcal{R}_{\hat{u}}^{(p)}(\delta)$ is the rotation of the coordinate frame. The active rotation $\mathcal{R}_{\hat{u}}^{(a)}(\delta)$ is equivalent to the passive rotation $\mathcal{R}_{\hat{u}}^{(p)}(-\delta)$.

The rotation transformation can be written as a matrix equation

$$\mathbf{r}_2 = \mathbf{R}_{\hat{u}}(\delta)\,\mathbf{r}_1, \tag{A.1}$$

where $\mathbf{r}_1$ is the vector before the rotation and $\mathbf{r}_2$ is the vector after the rotation. The 3×3 rotation matrix $\mathbf{R}_{\hat{u}}(\delta)$ is orthogonal and has a unit determinant, and so $\mathbf{R} \in SO(3)$.

For $\hat{u} = \hat{z}$, the rotation matrix is given by

$$\mathbf{R}_{\hat{z}}(\delta) = \begin{pmatrix} \cos\delta & -\sin\delta & 0 \\ \sin\delta & \cos\delta & 0 \\ 0 & 0 & 1 \end{pmatrix}. \tag{A.2}$$

Similarly, for $\hat{u} = \hat{y}$ we get

$$\mathbf{R}_{\hat{y}}(\delta) = \begin{pmatrix} \cos\delta & 0 & \sin\delta \\ 0 & 1 & 0 \\ -\sin\delta & 0 & \cos\delta \end{pmatrix}, \tag{A.3}$$

and for $\hat{u} = \hat{x}$

$$\mathbf{R}_{\hat{x}}(\delta) = \begin{pmatrix} 1 & 0 & 0 \\ 0 & \cos\delta & -\sin\delta \\ 0 & \sin\delta & \cos\delta \end{pmatrix}. \tag{A.4}$$

An arbitrary rotation of a rigid body can be written as the product of three rotations. The three angles (α, β, γ) that parametrize such a rotation are referred to as Euler angles. Often, we abbreviate $(\alpha, \beta, \gamma) = \Omega$. There are 12 possible conventions for choosing the set of three rotation axes (the only restriction being that the same axis cannot be used twice in a row).

Here we use the active point of view and the "proper" Euler angles (same first and third rotation axis) with the zyz convention, where $\hat{x}$, $\hat{y}$, $\hat{z}$ define the fixed coordinate frame. The rotation transformation is then

$$\mathcal{R}^{(a)}(\alpha, \beta, \gamma) = \mathcal{R}^{(a)}_{\hat{z}}(\alpha)\, \mathcal{R}^{(a)}_{\hat{y}}(\beta)\, \mathcal{R}^{(a)}_{\hat{z}}(\gamma), \tag{A.5}$$

This amounts to the three steps:

1. Rotate around $\hat{z}$ by an angle $\gamma \in [0, 2\pi)$,
2. Rotate around $\hat{y}$ by an angle $\beta \in [0, \pi)$,
3. Rotate around $\hat{z}$ by an angle $\alpha \in [0, 2\pi)$.

This sequence of rotations is illustrated in Fig. A.1 for a rigid body whose orientation is given by particle axes $\hat{x}'$, $\hat{y}'$, and $\hat{z}'$.

The matrix corresponding to the transformation $\mathcal{R}^{(a)}(\alpha, \beta, \gamma)$ is

$$\mathbf{R}(\alpha, \beta, \gamma) = \mathbf{R}_{\hat{z}}(\alpha)\, \mathbf{R}_{\hat{y}}(\beta)\, \mathbf{R}_{\hat{z}}(\gamma) \tag{A.6}$$

$$= \begin{pmatrix} c_\alpha c_\beta c_\gamma - s_\alpha s_\gamma & -c_\gamma s_\alpha - c_\alpha c_\beta s_\gamma & c_\alpha s_\beta \\ c_\beta c_\gamma s_\alpha + c_\alpha s_\gamma & c_\alpha c_\gamma - c_\beta s_\alpha s_\gamma & s_\alpha s_\beta \\ -c_\gamma s_\beta & s_\beta s_\gamma & c_\beta \end{pmatrix}, \tag{A.7}$$

where we abbreviated $\cos\delta = c_\delta$ and $\sin\delta = s_\delta$. The angles α, β, γ are sometimes called the angle of precession, nutation, and proper rotation, respectively. Another common convention, the zxz convention is related to the zyz convention by $\alpha_x = \alpha_y + \pi/2$ and $\gamma_x = \gamma_y - \pi/2$ [94].

We note that if we are studying a rigid body with symmetry under rotations around its $\hat{z}'$ axis, i.e., a uniaxial particle (since only $\hat{z}'$ is needed

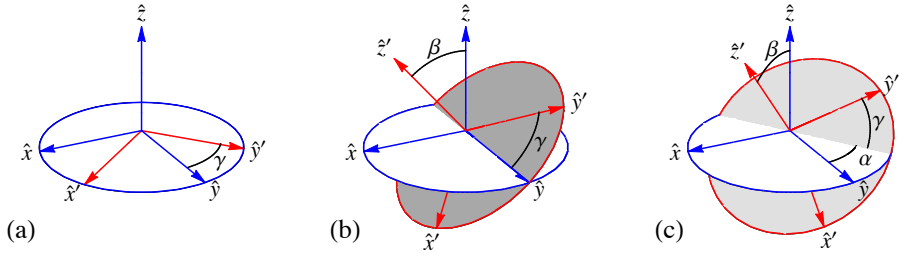

Figure A.1.: Illustration of the proper Euler angles in the zyz convention. The fixed coordinate frame is denoted $\hat{x}$, $\hat{y}$, $\hat{z}$ and the particle axes are $\hat{x}'$, $\hat{y}'$, $\hat{z}'$. In (a), a rotation of γ is performed around $\hat{z}$. Subsequently, in (b), a rotation of β is performed around $\hat{y}$. Finally, in (c) a rotation of α is performed around $\hat{z}$.

to specify its orientation), then the "internal" angle γ is undefined, and the angles α, β correspond to the azimuthal and polar angles of the unit vector $\hat{z}'$, respectively.

Appendix B.

Properties of Wigner matrices

Here we list the properties of the Wigner rotation matrices (also known as Wigner D-matrices) that we use in our calculations. A classical text on the subject is e.g. Ref. [213], but here we follow Ref. [212], which summarizes the relevant information concisely. It is important to use a consistent notation and be wary of the notoriously many variations in the notation used in literature (see Ref. [212] for a summary of some of these).

As discussed in Appendix A, the orientation of an arbitrarily shaped rigid body can be written in terms of three Euler angles $\Omega = (\alpha, \beta, \gamma)$. Wigner rotation matrices are representations of the rotation operator in a spherical basis. The Wigner matrix elements are elements of the rotation operator, here using the zyz convention (see Appendix A)

$$\begin{aligned}
\mathcal{D}^l_{mn}(\alpha,\beta,\gamma) &= \langle l\,m|\,\mathcal{R}^{(a)}(\alpha,\beta,\gamma)\,|l\,n\rangle && \text{(B.1)}\\
&= \langle l\,m|\,e^{-i\alpha J_z}e^{-i\beta J_y}e^{-i\gamma J_z}\,|l\,n\rangle && \text{(B.2)}\\
&= e^{-im\alpha}\langle l\,m|\,e^{-i\beta J_y}\,|l\,n\rangle e^{-in\gamma} && \text{(B.3)}\\
&= e^{-im\alpha}\,d^l_{mn}(\beta)\,e^{-in\gamma}, && \text{(B.4)}
\end{aligned}$$

where J_i is the angular momentum operator in the ith direction.[1] The reduced d^l_{mn} matrices are real, and can be written in terms of hypergeometric functions or Jacobi polynomials.

A Wigner matrix is a unitary matrix in an irreducible representation of $SO(3)$. This makes them a natural basis for expanding functions of Euler angles (which have a correspondence with the elements of $SO(3)$), similar to spherical harmonics being the natural basis for functions on the sphere. The

[1] For $SU(2)$: $l = 0, 1/2, 1, 3/2, \ldots$ and for $SO(3)$: $l = 0, 1, 2, \ldots$ and in both cases: $m, n = -l, -l+1, \ldots, l-1, l$. Thus a Wigner matrix of rank l has $(2l+1)^2$ elements.

elements of the Wigner rotation matrices are orthogonal, i.e.,

$$\int d\Omega\, \mathcal{D}^{l'*}_{m'n'}(\Omega)\, \mathcal{D}^{l}_{mn}(\Omega) = \frac{8\pi^2}{2l+1}\, \delta_{ll'}\, \delta_{mm'}\, \delta_{nn'}, \tag{B.5}$$

where the integrals over the Euler angles are

$$\int d\Omega = \int_0^{2\pi} d\alpha \int_0^{\pi} d\beta\, \sin\beta \int_0^{2\pi} d\gamma = 8\pi^2. \tag{B.6}$$

Additionally, it can be shown that the $\mathcal{D}^{l}_{mn}(\Omega)$ form a complete set [214].

The Wigner rotation matrices are unitary

$$\sum_{p=-l}^{l} \mathcal{D}^{l*}_{pm}(\Omega)\, \mathcal{D}^{l}_{pn}(\Omega) = \delta_{mn}, \tag{B.7}$$

$$\sum_{p=-l}^{l} \mathcal{D}^{l}_{mp}(\Omega)\, \mathcal{D}^{l*}_{np}(\Omega) = \delta_{mn}, \tag{B.8}$$

and they satisfy the following relations

$$\mathcal{D}^{l*}_{mn}(\Omega) = \mathcal{D}^{l}_{nm}(\Omega^{-1}) = (-1)^{m-n}\, \mathcal{D}^{l}_{-m-n}(\Omega), \tag{B.9}$$

where we use the abbreviated notation $\Omega^{-1} = (-\gamma, -\beta, -\alpha)$ for the Euler angles corresponding to the inverse rotation.

Since the product of two rotations is a rotation, there is a closure property of the Wigner matrices

$$\mathcal{D}^{l}_{mn}(\Omega_{12}) = \sum_{p=-l}^{l} \mathcal{D}^{l}_{mp}(\Omega_2^{-1})\, \mathcal{D}^{l}_{pn}(\Omega_1) \tag{B.10}$$

$$= \sum_{p=-l}^{l} \mathcal{D}^{l}_{pm}(\Omega_2)^*\, \mathcal{D}^{l}_{pn}(\Omega_1), \tag{B.11}$$

where Ω_{12} denotes the relative orientation between orientations Ω_1 and Ω_2.

Wigner matrices are related to the Legendre polynomials

$$\mathcal{D}^{l}_{mn}(0, \beta, 0) = d^{l}_{mn}(\beta) = \delta_{m,0}\, \delta_{n,0}\, P_l(\cos\beta), \tag{B.12}$$

and to the spherical harmonics [212]

$$\mathcal{D}^{l}_{m0}(\alpha,\beta,\gamma) = \left(\frac{4\pi}{2l+1}\right)^{1/2} Y^{*}_{lm}(\beta,\alpha), \tag{B.13}$$

$$\mathcal{D}^{l}_{0m}(\alpha,\beta,\gamma) = \left(\frac{4\pi}{2l+1}\right)^{1/2} Y^{*}_{l-m}(\beta,\gamma), \tag{B.14}$$

where we used the phase convention of Condon and Shortley.

Clebsch-Gordon coefficients C arise from integrals over three Wigner matrices

$$\int d\Omega\, \mathcal{D}^{l_3\,*}_{m_3 n_3}(\Omega)\, \mathcal{D}^{l_2}_{m_2 n_2}(\Omega)\, \mathcal{D}^{l_1}_{m_1 n_1}(\Omega) = \frac{8\pi^2}{2l_3+1} C(l_1,m_1;l_2,m_2;l_3,m_3) \times C(l_1,n_1;l_2,n_2;l_3,n_3), \tag{B.15}$$

where this integral is zero unless $m_1 + m_2 = m_3$, $n_1 + n_2 = n_3$, and the triangle rule for l_1, l_2, and l_3 is satisfied.

Appendix C.

Resumming the virial series

For infinite aspect ratio rods ($L/D \to \infty$), second-virial theory is thought to be exact. For the aspect ratio of $L/D = 100$, Ref. [8, 9] has shown that (in the isotropic phase) the ratio of the higher order virial coefficients to the second-virial coefficient B_n/B_2^{n-1} is less than 0.07 for $n = 3, 4, 5$. Even for the smaller aspect ratio of $L/D = 10$, Ref. [8, 9] finds that $B_3/B_2^2 \approx 0.3$ and $B_4/B_2^3 \approx -0.02$. Therefore, we expect second-virial theory to be quantitatively accurate for aspect ratios on the order of 100, and still qualitatively useful for smaller aspect ratios. For these smaller aspect ratios, it would be desirable to calculate the third-virial term, but this is often computationally impractical. One simpler method to correct for the inaccuracies in applying second-virial theory to smaller aspect ratio rods, is the Parsons-Lee correction. This consists of adding the higher order virial terms, by approximating these by a hard sphere system at the same density. That is, we take the excess free energy to be [175, 176]

$$\frac{\beta F_{\rm ex}[\rho, \psi(\Omega))]}{N} = \rho B_2[\psi(\Omega)] + \frac{B_2[\psi(\Omega)]}{B_2^{\rm HS}} \left[\frac{\beta F_{ex}^{\rm HS}}{N} - \rho B_2^{\rm HS}\right] \quad \text{(C.1)}$$

$$= \rho B_2[\psi(\Omega)] G(\eta), \quad \text{(C.2)}$$

where the second-virial coefficient for hard spheres is $B_2^{\rm HS} = 4v_0$ with v_0 the single-particle volume and where the excess free energy for a system of hard spheres $F_{ex}^{\rm HS}$ is given very accurately by the Carnahan-Starling expression

$$\frac{\beta F_{ex}^{\rm HS}}{N} = \frac{(4 - 3\eta)\eta}{(1 - \eta)^2}, \quad \text{(C.3)}$$

which gives the standard Parsons-Lee correction [175, 176]

$$G(\eta) = \frac{1 - 3\eta/4}{(1-\eta)^2}. \tag{C.4}$$

We emphasize that this is only an approximate resumming of the virial series, which neglects the angular correlations in the higher order virial terms. For arbitrarily shaped particles, there is no rigorous argument to adding this correction, however, second-virial Parsons-Lee theory has given good agreement with simulations for the equation of state of hard boomerangs [81].

Alternatively, given that we know the second- and third-virial terms analytically or numerically, we may wish to apply the rescaling to the second term as

$$\begin{aligned} \frac{\beta F_{\rm ex}[\rho, \psi(\Omega))]}{N} &= \rho B_2[\psi(\Omega)] + \frac{1}{2}\rho^2 B_3[\psi(\Omega)] \\ &\quad + \frac{B_2[\psi(\Omega)]}{B_2^{\rm HS}}\left[\frac{\beta F_{ex}^{\rm HS}}{N} - \rho B_2^{\rm HS} - \frac{1}{2}\rho^2 B_3^{\rm HS}\right] \qquad \text{(C.5)} \\ &= \rho B_2[\psi(\Omega)]\tilde{G}_2(\eta) + \frac{1}{2}\rho^2 B_3[\psi(\Omega)]. \qquad \text{(C.6)} \end{aligned}$$

where the third-virial coefficient for hard spheres is $B_3^{\rm HS} = 10v_0^2$, which gives

$$\tilde{G}_2(\eta) = \frac{1 - 2\eta + 5\eta^2/2 - 5\eta^3/4}{(1-\eta)^2}. \tag{C.7}$$

Or, we can choose to apply the rescaling to the third term as [215]

$$\begin{aligned} \frac{\beta F_{\rm ex}[\rho, \psi(\Omega))]}{N} &= \rho B_2[\psi(\Omega)] + \frac{1}{2}\rho^2 B_3[\psi(\Omega)] \\ &\quad + \frac{B_3[\psi(\Omega)]}{B_3^{\rm HS}}\left[\frac{\beta F_{ex}^{\rm HS}}{N} - \rho B_2^{\rm HS} - \frac{1}{2}\rho^2 B_3^{\rm HS}\right] \qquad \text{(C.8)} \\ &= \rho B_2[\psi(\Omega)] + \frac{1}{2}\rho^2 B_3[\psi(\Omega)]\tilde{G}_3(\eta), \qquad \text{(C.9)} \end{aligned}$$

with

$$\tilde{G}_3(\eta) = \frac{1 - 4\eta/5}{(1-\eta)^2}. \tag{C.10}$$

For a comparison of these different rescaling factors, see Fig. C.1. If the equation of state for the isotropic phase of the particles being studied is known, e.g. from Monte Carlo simulations, another approach is to use this as the reference system instead of hard spheres. This was studied at the second and third-virial level for hard platelets in Ref. [215].

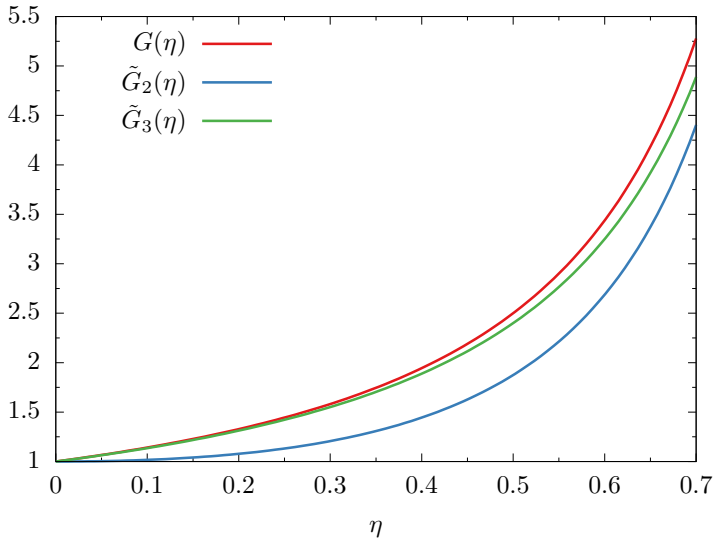

Figure C.1.: The three different rescaling factors described in this appendix, as a function of packing fraction η.

Bibliography

[1] P. de Gennes and J. Prost, *The Physics of Liquid Crystals* (Oxford University Press, New York, 1993).

[2] Z. Dogic and S. Fraden, Curr. Opin. Colloid In. **11**, 47 (2006).

[3] A. Kuijk, D. V. Byelov, A. V. Petukhov, A. van Blaaderen, and A. Imhof, Faraday discuss. **159**, 181 (2012).

[4] P. Bolhuis and D. Frenkel, J. Chem. Phys. **106**, 666 (1997).

[5] L. Onsager, Ann. N. Y. Acad. Sci. **51**, 627 (1949).

[6] R. Evans, Adv. Phys. **28**, 143 (1979).

[7] J. P. Straley, Mol. Cryst. Liq. Cryst. **24**, 7 (1973).

[8] D. Frenkel, J. Phys. Chem. **91**, 4912 (1987).

[9] D. Frenkel, J. Phys. Chem. **92**, 5314 (1988).

[10] G. J. Vroege and H. N. W. Lekkerkerker, Rep. Prog. Phys. **55**, 1241 (1992).

[11] B. M. Mulder, Mol. Phys. **103**, 1411 (2005).

[12] B. M. Mulder, e-print arXiv:1806.11018 (2018).

[13] R. F. Kayser and H. J. Raveché, Phys. Rev. A **17**, 2067 (1978).

[14] B. Mulder, Phys. Rev. A **35**, 3095 (1987).

[15] A. Poniewierski, Phys. Rev. A **45**, 5605 (1992).

[16] R. van Roij, P. Bolhuis, B. Mulder, and D. Frenkel, Phys. Rev. E **52**, R1277 (1995).

[17] M. J. Perrin, *Brownian Movement and Molecular Reality: Translated from the Annales de Chimie Et de Physique, 8 Series, September 1909,*

by F. Soddy (Taylor & Francis, 1910).

[18] T. Biben, J.-P. Hansen, and J.-L. Barrat, J. Chem. Phys. **98**, 7330 (1993).

[19] R. Piazza, T. Bellini, and V. Degiorgio, Phys. Rev. Lett. **71**, 4267 (1993).

[20] M. Rutgers, J. Dunsmuir, J.-Z. Xue, W. Russel, and P. Chaikin, Phys. Rev. B **53**, 5043 (1996).

[21] S. Savenko and M. Dijkstra, Phys. Rev. E **70**, 051401 (2004).

[22] A. B. Harris, R. D. Kamien, and T. C. Lubensky, Rev. Mod. Phys. **71**, 1745 (1999).

[23] E. Grelet and S. Fraden, Phys. Rev. Lett. **90**, 198302 (2003).

[24] S. Fraden and Z. Dogic, Langmuir **16**, 7820 (2000).

[25] Z. Zhang and E. Grelet, Soft Matter **9**, 1015 (2013).

[26] F. Tombolato, A. Ferrarini, and E. Grelet, Phys. Rev. Lett. **96**, 258302 (2006).

[27] H. H. Wensink and L. Morales-Anda, J. Chem. Phys. **143**, 144907 (2015).

[28] C. Greco and A. Ferrarini, Phys. Rev. Lett. **115**, 147801 (2015).

[29] S. Dussi, S. Belli, R. van Roij, and M. Dijkstra, J. Chem. Phys. **142**, 074905 (2015).

[30] H. H. Wensink and G. Jackson, J. Chem. Phys. **130**, 234911 (2009).

[31] H. H. Wensink and G. Jackson, J. Phys. Condens. Matter **23**, 194107 (2011).

[32] J. Lapointe and D. A. Marvin, Mol. Cryst. Liq. Cryst. **19**, 269 (1973).

[33] J. Tang and S. Fraden, Liq. Cryst. **19**, 459 (1995).

[34] A. Suzuki, T. Maeda, and T. Ito, Biophys. J. **59**, 25 (1991).

[35] C. M. Coppin and P. C. Leavis, Biophys. J. **63**, 794 (1992).

[36] R. Furukawa, R. Kundra, and M. Fechheimer, Biochemistry **32**, 12346 (1993).

[37] R. S. Werbowyj and D. G. Gray, Mol. Cryst. Liq. Cryst. **34**, 97 (1976).

[38] R. S. Werbowyj and D. G. Gray, Macromolecules **13**, 69 (1980).

[39] V. A. Davis, L. M. Ericson, A. N. G. Parra-Vasquez, H. Fan, Y. Wang, V. Prieto, J. A. Longoria, S. Ramesh, R. K. Saini, C. Kittrell, W. E. Billups, W. W. Adams, R. H. Hauge, R. E. Smalley, and M. Pasquali, Macromolecules **37**, 154 (2004).

[40] P. K. Rai, R. A. Pinnick, A. N. G. Parra-Vasquez, V. A. Davis, H. K. Schmidt, R. H. Hauge, R. E. Smalley, and M. Pasquali, J. Am. Chem. Soc. **128**, 591 (2006).

[41] A. Stroobants, H. N. W. Lekkerkerker, and T. Odijk, Macromolecules **19**, 2232 (1986).

[42] A. Semenov and A. R. Khokhlov, Sov. Phys. Usp. **31**, 988 (1988).

[43] I. A. Nyrkova, N. P. Shusharina, and A. R. Khokhlov, Macromol. Theory Simul. **6**, 965 (1997).

[44] S. B. Chen and D. L. Koch, J. Chem. Phys. **104**, 359 (1996).

[45] I. I. Potemkin, R. E. Limberger, A. N. Kudlay, and A. R. Khokhlov, Phys. Rev. E **66**, 011802 (2002).

[46] I. I. Potemkin, N. N. Oskolkov, A. R. Khokhlov, and P. Reineker, Phys. Rev. E **72**, 021804 (2005).

[47] D. McQuarrie, *Statistical mechanics* (University Science Books, Sausalito, CA, 2000).

[48] M. Fixman and J. Skolnick, Macromolecules **11**, 863 (1978).

[49] S. L. Brenner and V. A. Parsegian, Biophys. J. **14**, 327 (1974).

[50] D. Stigter, Biopolymers **16**, 1435 (1977).

[51] B. Mulder, Phys. Rev. A **39**, 360 (1989).

[52] J. Herzfeld, A. E. Berger, and J. W. Wingate, Macromolecules **17**, 1718 (1984).

[53] R. van Roij, Eur. J. Phys. **26**, S57 (2005).

[54] E. Grelet, Phys. Rev. X **4**, 021053 (2014).

[55] K. R. Purdy and S. Fraden, Phys. Rev. E **70**, 061703 (2004).

[56] R. B. Scheele and M. A. Lauffer, Biochemistry **6**, 3076 (1967).

[57] S. Fraden, G. Maret, D. L. D. Caspar, and R. B. Meyer, Phys. Rev. Lett. **63**, 2068 (1989).

[58] A. Kuijk, A. Imhof, M. H. W. Verkuijlen, T. H. Besseling, E. R. H. van Eck, and A. van Blaaderen, Part. Part. Syst. Charact. **31**, 706 (2014).

[59] B. Liu, T. H. Besseling, M. Hermes, A. F. Demirörs, A. Imhof, and A. van Blaaderen, Nat. Commun. **5**, 3092 (2014).

[60] Z. Zhang, J. Buitenhuis, A. Cukkemane, M. Brocker, M. Bott, and J. K. Dhont, Langmuir **26**, 10593 (2010).

[61] A. B. Fall, S. B. Lindström, O. Sundman, L. Ödberg, and L. Wågberg, Langmuir **27**, 11332 (2011).

[62] J. P. Straley, Phys. Rev. A **8**, 2181 (1973).

[63] G. J. Vroege and T. Odijk, J. Chem. Phys. **87**, 4223 (1987).

[64] T. Odijk, Liq. Cryst. **1**, 553 (1986).

[65] S. Belli, S. Dussi, M. Dijkstra, and R. van Roij, Phys. Rev. E **90**, 020503(R) (2014).

[66] E. Eggen, M. Dijkstra, and R. van Roij, Phys. Rev. E **79**, 041401 (2009).

[67] G. R. Luckhurst and T. J. Sluckin, *Biaxial Nematic Liquid Crystals: Theory, Simulation and Experiment* (John Wiley & Sons, Chichester, 2015).

[68] M. J. Freiser, Phys. Rev. Lett. **24**, 1041 (1970).

[69] J. P. Straley, Phys. Rev. A **10**, 1881 (1974).

[70] M. P. Allen, Liq. Cryst. **8**, 499 (1990).

[71] P. J. Camp and M. Allen, J. Chem. Phys. **106**, 6681 (1997).

[72] S. D. Peroukidis and A. G. Vanakaras, Soft Matter **9**, 7419 (2013).

[73] S. D. Peroukidis, A. G. Vanakaras, and D. J. Photinos, Phys. Rev. E **88**, 062508 (2013).

[74] S. Dussi, N. Tasios, T. Drwenski, R. van Roij, and M. Dijkstra, Phys. Rev. Lett. **120**, 177801 (2018).

[75] T. Lubensky and L. Radzihovsky, Phys. Rev. E **66**, 031704 (2002).

[76] H. Takezoe and Y. Takanishi, Jpn. J. Appl. Phys. **45**, 597 (2006).

[77] I. Dozov, EPL **56**, 247 (2001).

[78] C. Greco and A. Ferrarini, Phys. Rev. Lett. **115**, 147801 (2015).

[79] P. I. C. Teixeira, A. Masters, and B. Mulder, Mol. Cryst. Liq. Cryst. **323**, 167 (1998).

[80] G. Luckhurst, Thin Solid Films **393**, 40 (2001).

[81] P. J. Camp, M. P. Allen, and A. J. Masters, J. Chem. Phys. **111**, 9871 (1999).

[82] Y. Lansac, P. K. Maiti, N. A. Clark, and M. A. Glaser, Phys. Rev. E **67**, 011703 (2003).

[83] A. Dewar and P. J. Camp, Phys. Rev. E **70**, 011704 (2004).

[84] A. Dewar and P. J. Camp, J. Chem. Phys. **123**, 174907 (2005).

[85] Y. Yang, G. Chen, L. J. Martinez-Miranda, H. Yu, K. Liu, and Z. Nie, J. Am. Chem. Soc. **138**, 68 (2016), pMID: 26700616.

[86] Y. Yang, H. Pei, G. Chen, K. T. Webb, L. J. Martinez-Miranda, I. K. Lloyd, Z. Lu, K. Liu, and Z. Nie, Sci. Adv. **4**, eaas8829 (2018).

[87] K. R. Purdy, S. Varga, A. Galindo, G. Jackson, and S. Fraden, Phys. Rev. Lett. **94**, 057801 (2005).

[88] M. Dennison, M. Dijkstra, and R. van Roij, Phys. Rev. Lett. **106**, 208302 (2011).

[89] M. Dennison, M. Dijkstra, and R. van Roij, J. Chem. Phys. **135**, 144106 (2011).

[90] P. P. Wessels and B. M. Mulder, Soft Mater. **1**, 313 (2003).

[91] P. P. Wessels and B. M. Mulder, J. Phys. Condens. Matter **18**, 9335 (2006).

[92] A. Vaghela, P. I. Teixeira, and E. M. Terentjev, Phys. Rev. E **96**, 042703 (2017).

[93] F. Bisi, R. Rosso, E. G. Virga, and G. E. Durand, Phys. Rev. E **78**, 011705 (2008).

[94] R. Rosso, Liq. Cryst. **34**, 737 (2007).

[95] R. Blaak and B. M. Mulder, Phys. Rev. E **58**, 5873 (1998).

[96] A. Khokhlov and A. Semenov, Physica A **108**, 546 (1981).

[97] A. Khokhlov and A. Semenov, Physica A **112**, 605 (1982).

[98] M. Dijkstra and D. Frenkel, Phys. Rev. E **51**, 5891 (1995).

[99] Z. Dogic, J. Zhang, A. W. C. Lau, H. Aranda-Espinoza, P. Dalhaimer, D. E. Discher, P. A. Janmey, R. D. Kamien, T. C. Lubensky, and A. G. Yodh, Phys. Rev. Lett. **92**, 125503 (2004).

[100] H. N. W. Lekkerkerker, P. Coulon, and v. d. R. Haegen, J. Chem. Phys. **80**, 3427 (1984).

[101] F. Hagemans, *Sculpting at the Nanoscale: Colloidal Rods with Graded Chemistry*, Ph.D. thesis, Utrecht University (2018).

[102] L. J. Yu and A. Saupe, Phys. Rev. Lett. **45**, 1000 (1980).

[103] G. R. Luckhurst, Nature **430**, 413 (2004).

[104] K. Severing and K. Saalwächter, Phys. Rev. Lett. **92**, 125501 (2004).

[105] L. A. Madsen, T. J. Dingemans, M. Nakata, and E. T. Samulski, Phys. Rev. Lett. **92**, 145505 (2004).

[106] B. R. Acharya, A. Primak, and S. Kumar, Phys. Rev. Lett. **92**, 145506 (2004).

[107] R. Berardi and C. Zannoni, J. Chem. Phys. **113**, 5971 (2000).

[108] R. Berardi, L. Muccioli, S. Orlandi, M. Ricci, and C. Zannoni, J. Phys. Condens. Matter **20**, 463101 (2008).

[109] E. van den Pol, A. V. Petukhov, D. M. E. Thies-Weesie, D. V. Byelov, and G. J. Vroege, Phys. Rev. Lett. **103**, 258301 (2009).

[110] S. Belli, A. Patti, M. Dijkstra, and R. van Roij, Phys. Rev. Lett. **107**, 148303 (2011).

[111] D. Frenkel, B. M. Mulder, and J. P. McTague, Phys. Rev. Lett. **52**, 287 (1984).

[112] A. Cuetos, M. Dennison, A. Masters, and A. Patti, Soft Matter **13**, 4720 (2017).

[113] M. P. Taylor and J. Herzfeld, Phys. Rev. A **44**, 3742 (1991).

[114] L. Longa and G. Pająk, Liq. Cryst. **32**, 1409 (2005).

[115] D. Allender and L. Longa, Phys. Rev. E **78**, 011704 (2008).

[116] P. K. Mukherjee and K. Sen, J. Chem. Phys. **130**, 141101 (2009).

[117] Y. Martínez-Ratón, S. Varga, and E. Velasco, Phys. Rev. E **78**, 031705 (2008).

[118] M. Marechal, S. Dussi, and M. Dijkstra, J. Chem. Phys. **146**, 24905 (2017).

[119] Y. Martínez-Ratón, S. Varga, and E. Velasco, Phys. Chem. Chem. Phys. **13**, 13247 (2011).

[120] B. Tjipto-Margo and G. T. Evans, J. Chem. Phys. **93**, 4254 (1990).

[121] C. McBride and E. Lomba, Fluid Ph. Equilibria **225**, 37 (2007).

[122] R. Eppenga and D. Frenkel, Mol. Phys. **52**, 1303 (1984).

[123] K. Shundyak and R. van Roij, Phys. Rev. E **69**, 041703 (2004).

[124] T. Svedberg, K. Pedersen, and J. Bauer, *The ultracentrifuge*, International series of monographs on physics (The Clarendon Press, 1940).

[125] M. Raşa and A. P. Philipse, Nature **429**, 857 (2004).

[126] K. L. Planken and H. Cölfen, Nanoscale **2**, 1849 (2010).

[127] R. van Roij, J. Phys. Condens. Matter **15**, S3569 (2003).

[128] M. Rasa, B. H. Erné, B. Zoetekouw, R. van Roij, and A. P. Philipse, J. Phys. Condens. Matter **17**, 2293 (2005).

[129] J. Zwanikken and R. van Roij, Europhys. Lett. **71**, 480 (2005).

[130] R. Piazza, S. Buzzaccaro, E. Secchi, and A. Parola, Soft Matter **8**, 7112 (2012).

[131] R. Piazza, S. Buzzaccaro, E. Secchi, and A. Parola, Phys. Biol. **10**, 45005 (2013).

[132] M. Schmidt, M. Dijkstra, and J.-P. Hansen, Phys. Rev. Lett. **93**, 088303 (2004).

[133] D. de las Heras, N. Doshi, T. Cosgrove, J. Phipps, D. I. Gittins, J. S. van Duijneveldt, and M. Schmidt, Sci. Rep. **2**, 789 (2012).

[134] R. Piazza, Rep. Prog. Phys. **77**, 056602 (2014).

[135] D. de las Heras and M. Schmidt, Soft Matter **9**, 8636 (2013).

[136] D. de las Heras and M. Schmidt, J. Phys. Condens. Matter **27**, 194115 (2015).

[137] D. de las Heras, L. L. Treffenstädt, and M. Schmidt, Phys. Rev. E **93**, 030601 (2016).

[138] P. J. Flory and A. Abe, Macromolecules **11**, 1119 (1978).

[139] T. Odijk and H. N. Lekkerkerker, J. Phys. Chem. **89**, 2090 (1985).

[140] T. Birshtein, B. Kolegov, and V. Pryamitsyn, Polym. Sci. USS **30**, 316 (1988).

[141] G. J. Vroege and H. N. W. Lekkerkerker, J. Phys. Chem. **97**, 3601 (1993).

[142] R. van Roij and B. Mulder, J. Chem. Phys. **105**, 11237 (1996).

[143] P. C. Hemmer, Mol. Phys. **96**, 1153 (1999).

[144] S. Varga and I. Szalai, Phys. Chem. Chem. Phys. **2**, 1955 (2000).

[145] A. Speranza and P. Sollich, J. Chem. Phys. **117**, 5421 (2002).

[146] R. P. Sear and G. Jackson, J. Chem. Phys. **103**, 8684 (1995).

[147] R. van Roij and B. Mulder, Phys. Rev. E **54**, 6430 (1996).

[148] R. van Roij, B. Mulder, and M. Dijkstra, Physica A **261**, 374 (1998).

[149] P. Hemmer, Journal of Statistical Physics **100**, 3 (2000).

[150] S. Varga, A. Galindo, and G. Jackson, Mol. Phys. **101**, 817 (2003).

[151] S. Varga, K. Purdy, A. Galindo, S. Fraden, and G. Jackson, Phys. Rev. E **72**, 051704 (2005).

[152] J.-P. Hansen and I. R. McDonald, *Theory of Simple Liquids*, 3rd ed. (Academic Press, Burlington, 2006).

[153] T. Besseling, *Self-assembly of colloidal spheres and rods in external fields*, Ph.D. thesis, Utrecht University (2014).

[154] H. E. Bakker, S. Dussi, B. L. Droste, T. H. Besseling, C. L. Kennedy, E. I. Wiegant, B. Liu, A. Imhof, M. Dijkstra, and A. van Blaaderen, Soft Matter **12**, 9238 (2016).

[155] G. Cinacchi, Y. Martínez-Ratón, L. Mederos, and E. Velasco, J. Chem. Phys. **124**, 234904 (2006).

[156] D. S. Hecht, L. Hu, and G. Irvin, Adv. Mater. **23**, 1482 (2011).

[157] R. M. Mutiso and K. I. Winey, Prog. Polym. Sci. **40**, 63 (2015).

[158] A. V. Kyrylyuk and P. van der Schoot, Proc. Natl. Acad. Sci. U.S.A. **105**, 8221 (2008).

[159] R. H. Otten and P. van der Schoot, Phys. Rev. Lett. **103**, 225704 (2009).

[160] R. H. Otten and P. van der Schoot, J. Chem. Phys. **134**, 094902 (2011).

[161] R. M. Mutiso, M. C. Sherrott, J. Li, and K. I. Winey, Phys. Rev. B **86**, 214306 (2012).

[162] B. Nigro, C. Grimaldi, P. Ryser, A. P. Chatterjee, and P. van der Schoot, Phys. Rev. Lett. **110**, 015701 (2013).

[163] H. Meyer, P. van der Schoot, and T. Schilling, J. Chem. Phys. **143**, 044901 (2015).

[164] S. I. White, B. A. DiDonna, M. Mu, T. C. Lubensky, and K. I. Winey, Phys. Rev. B **79**, 024301 (2009).

[165] R. H. Otten and P. van der Schoot, Phys. Rev. Lett. **108**, 088301 (2012).

[166] F. Dalmas, R. Dendievel, L. Chazeau, J.-Y. Cavaillé, and C. Gauthier, Acta Mater. **54**, 2923 (2006).

[167] A. Lucas, C. Zakri, M. Maugey, M. Pasquali, P. van der Schoot, and P. Poulin, J. Phys. Chem. C **113**, 20599 (2009).

[168] G. Ambrosetti, C. Grimaldi, I. Balberg, T. Maeder, A. Danani, and P. Ryser, Phys. Rev. B **81**, 155434 (2010).

[169] T. L. Hill, J. Chem. Phys. **23**, 617 (1955).

[170] A. Coniglio, U. De Angelis, and A. Forlani, J. Phys. A **10**, 1123 (1977).

[171] S. Torquato, *Random heterogeneous materials: microstructure and macroscopic properties* (Springer-Verlag New York, 2002).

[172] B. Vigolo, C. Coulon, M. Maugey, C. Zakri, and P. Poulin, Science **309**, 920 (2005).

[173] A. Bug, S. Safran, and I. Webman, Phys. Rev. B **33**, 4716 (1986).

[174] L. Berhan and A. Sastry, Phys. Rev. E **75**, 041120 (2007).

[175] J. D. Parsons, Phys. Rev. A **19**, 1225 (1979).

[176] S.-D. Lee, J. Chem. Phys. **87**, 4972 (1987).

[177] T. Schilling, M. A. Miller, and P. van der Schoot, EPL **111**, 56004 (2015).

[178] L. Berhan and A. Sastry, Phys. Rev. E **75**, 041121 (2007).

[179] C. Li, E. T. Thostenson, and T.-W. Chou, Compos. Sci. Technol. **68**, 1445 (2008).

[180] I. Balberg, C. H. Anderson, S. Alexander, and N. Wagner, Phys. Rev. B **30**, 3933 (1984).

[181] G. Ambrosetti, N. Johner, C. Grimaldi, A. Danani, and P. Ryser, Phys. Rev. E **78**, 061126 (2008).

[182] A. P. Chatterjee, J. Phys. Condens. Matter **20**, 255250 (2008).

[183] A. P. Chatterjee, J. Chem. Phys. **132**, 224905 (2010).

[184] S. Kale, F. A. Sabet, I. Jasiuk, and M. Ostoja-Starzewski, J. Appl. Phys. **118**, 154306 (2015).

[185] A. P. Chatterjee, J. Chem. Phys. **141**, 034903 (2014).

[186] A. P. Chatterjee, J. Phys. Condens. Matter **23**, 375101 (2011).

[187] A. P. Chatterjee, J. Chem. Phys. **137**, 134903 (2012).

[188] F. Du, J. E. Fischer, and K. I. Winey, Phys. Rev. B **72**, 121404 (2005).

[189] S. P. Finner, M. I. Kotsev, M. A. Miller, and P. van der Schoot, J. Chem. Phys. **148**, 034903 (2018).

[190] A. P. Chatterjee, J. Chem. Phys. **140**, 204911 (2014).

[191] K. S. Novoselov, A. K. Geim, S. V. Morozov, D. Jiang, Y. Zhang, S. V. Dubonos, I. V. Grigorieva, and A. A. Firsov, Science **306**, 666 (2004).

[192] S. Stankovich, D. A. Dikin, G. H. Dommett, K. M. Kohlhaas, E. J. Zimney, E. A. Stach, R. D. Piner, S. T. Nguyen, and R. S. Ruoff, Nature **442**, 282 (2006).

[193] E. Tkalya, M. Ghislandi, R. Otten, M. Lotya, A. Alekseev, P. van der Schoot, J. Coleman, G. de With, and C. Koning, ACS Appl. Mater. Interfaces **6**, 15113 (2014).

[194] E. Tkalya, M. Ghislandi, W. Thielemans, P. van der Schoot, G. de With, and C. Koning, ACS Macro Lett. **2**, 157 (2013).

[195] C. Schütz, M. Agthe, A. B. Fall, K. Gordeyeva, V. Guccini, M. Salajková, T. S. Plivelic, J. P. F. Lagerwall, G. Salazar-Alvarez, and L. Bergström, Langmuir **31**, 6507 (2015).

[196] S. Elazzouzi-Hafraoui, Y. Nishiyama, J.-L. Putaux, L. Heux, F. Dubreuil, and C. Rochas, Biomacromolecules **9**, 57 (2008).

[197] T. Drwenski, S. Dussi, M. Dijkstra, R. van Roij, and P. van der Schoot, J. Chem. Phys. **147**, 224904 (2017).

[198] A. P. Chatterjee and C. Grimaldi, Phys. Rev. E **92**, 032121 (2015).

[199] A. P. Chatterjee, private communication (2018).

[200] A. Isihara, J. Chem. Phys. **18**, 1446 (1950).

[201] T. Kihara, Rev. Mod. Phys. **25**, 831 (1953).

[202] L. Mederos, E. Velasco, and Y. Martinez-Raton, J. Phys. Condens. Matter **26**, 463101 (2014).

[203] Y. Rosenfeld, J. Chem. Phys. **89**, 4272 (1988).

[204] Y. Rosenfeld, Phys. Rev. Lett. **63**, 980 (1989).

[205] M. Schmidt, Phys. Rev. E **63**, 050201 (2001).

[206] J. Phillips and M. Schmidt, Phys. Rev. E **81**, 041401 (2010).

[207] T. DeSimone, S. Demoulini, and R. M. Stratt, J. Chem. Phys. **85**, 391 (1986).

[208] C. Grimaldi, J. Chem. Phys. **147**, 074502 (2017).

[209] M. Mathew, T. Schilling, and M. Oettel, Phys. Rev. E **85**, 061407 (2012).

[210] S. Torquato and Y. Jiao, Phys. Rev. E **87**, 022111 (2013).

[211] S. Torquato, J. Chem. Phys. **136**, 054106 (2012).

[212] M. A. Morrison and G. A. Parker, Aust. J. Phys. **40**, 465 (1987).

[213] D. M. Brink and G. R. Satchler, *Angular momentum* (Clarendon Press, 1968).

[214] F. Peter and H. Weyl, Math. Ann. **97**, 737 (1927).

[215] G. Cinacchi and A. Tani, J. Phys. Chem. B **119**, 5671 (2015).

Summary

In this thesis, we study the liquid crystal phases of anisotropic colloids such as rods, boomerangs, and cuboids. Liquid crystal phases are more ordered than liquids but less ordered than crystals. For example, the nematic phase has long-range orientational order but no positional order and the smectic phase has positional order in one direction in addition to orientational order. Our calculations are based on Onsager's second-virial theory, which is exact for hard needle-like rods, and can be extended to study many other types of colloidal particles.

In Chapter 2, we study weakly and strongly charged uniaxial rods using second-virial theory. We show that the so-called "twisting" effect due to electrostatic repulsion can lead to coexistence between a weakly and a strongly aligned nematic phase. In addition, we investigate the stability of the nematic with respect to twist deformations to see if a chiral nematic phase could spontaneously form due to the electrostatic twisting effect. We find that although the twisting effect reduces the twist elastic constant, it always remains positive and so there is no evidence of a spontaneous symmetry breaking transition.

In Chapter 3, we apply second-virial theory to colloidal particles with a less symmetric shape, namely flexible boomerangs, consisting of two rodlike segments that can fluctuate around a certain preferred interarm angle. Here we find that stiff boomerangs can form prolate, oblate, and biaxial nematic phases depending on the preferred interarm angle and the density. The more flexible boomerangs have reduced regions of stability for the oblate and biaxial nematic phases, preferring to deform into straight rods and form prolate nematics. We then consider rigid boomerangs in Chapter 4. We find similar phase behavior as in the case of stiff boomerangs, but since we use Monte Carlo integration for the excluded volume, we can also consider boomerangs with small interarm angles. In addition, we investigate the stability of the nematic phases with respect to smectic perturbations. We find that these may considerably limit the density regime of the nematic phases for bent particles, and that this may be the case even for boomerangs with higher aspect ratios.

In Chapter 5, we consider cuboidal colloids within second- and third-virial theory. These can also form prolate, oblate, and biaxial nematic phases depending on the particle shape and the density. The so-called dual shape is predicted to be the ideal shape for cuboids to form biaxial nematic phases. We find that in contrast with previous predictions, there is no direct isotropic-biaxial nematic transition for dual-shaped cuboids, due to an intervening uniaxial nematic phase. Within second-virial theory, there is perfect symmetry between oblate and prolate at the dual shape, and so the free energies of these two phases are identical in this case. Within third-virial theory, this symmetry is broken. For a simplified model where the cuboids can only have six discrete orientations, we find that the intervening uniaxial phase is prolate at the dual shape. However, a more realistic continuous orientation model shows that the oblate nematic is preferred at the dual-shape, in agreement with recent simulations.

We study the sedimentation of a binary mixture of thick and thin hard rods in Chapter 6. Here we find that gravity can cause a large number of phase sequences as a function of height in a "test tube." We map out all possible stacking sequences for three diameter ratios, and find some surprising sequences like an isotropic phase sandwiched between two nematic phases. In the most complex phase diagram considered here, we find sixteen distinct stacking sequences, including several with five sedimented layers. We also calculate density and composition profiles as a function of height.

Finally, we study the percolation threshold of various hard particles using connectedness percolation theory within the second-virial approximation. In Chapter 7, we consider rodlike particles with kink or bend deformations, which are relevant for, for example, systems of carbon nanotubes which are not idealized rods but often modeled as such. We find that while the percolation threshold depends strongly on the aspect ratios of the rods, small or moderate shape deformations have very little effect. In Chapter 8, we consider other types of shape irregularities, namely, polygonal rods and platelets with various numbers of sides. Here we analytically calculate the percolation threshold in terms of three single-particle measures. We find that changing the cross section of a rod or platelet from a disk to a polygon decreases the percolation threshold, in some cases significantly. We explain this in terms of an increase in the single-particle surface area to volume ratio for particles that have cross sections with fewer sides.

Samenvatting

In dit proefschrift bestuderen we de vloeibare kristalfasen van anisotrope colloïden, zoals staven, boemerangen en balken. Vloeibare kristalfasen zijn meer geordend dan vloeistoffen, maar minder geordend dan kristallen. De nematische fase heeft bijvoorbeeld een oriëntatieordening op lange afstand maar geen positionele ordening en de smectische fase heeft een positionele ordening in één richting naast de oriëntatieordening. Onze berekeningen zijn gebaseerd op de tweede viriaaltheorie van Onsager, die exact is voor harde naaldachtige staven, en kan worden uitgebreid om vele andere soorten colloïdale deeltjes te bestuderen.

In Hoofdstuk 2, bestuderen we zwak en sterk geladen uniaxiale staven met behulp van de tweede viriaaltheorie. We laten zien dat het zogenaamde "twist-effect" als gevolg van elektrostatische afstoting kan leiden tot co-existentie tussen een zwak en een sterk uitgelijnde nematische fase. Daarnaast onderzoeken we de stabiliteit van de nematische fase met betrekking tot twistvervormingen om te zien of er een chirale nematische fase spontaan zou kunnen ontstaan als gevolg van het elektrostatische twisteffect. We vinden dat, hoewel het twisteffect de twist-elastische constante vermindert, deze altijd positief blijft en er dus geen tekenen zijn van een spontane symmetriebrekende overgang.

In Hoofdstuk 3, passen we de tweede viriaaltheorie toe op colloïdale deeltjes met een minder symmetrische vorm, namelijk flexibele boemerangs. Deze deeltjes bestaan uit twee staafachtige segmenten die zijn gekoppeld aan hun uiteinden, onder een interarmhoek die kan fluctueren rondom een bepaalde voorkeurshoek. Hier vinden we dat stijve boemerangen prolate, oblate en biaxiale nematische fasen kunnen vormen, afhankelijk van de voorkeurshoek en de dichtheid. De meer flexibele boemerangs hebben verminderde stabiliteitsgebieden voor de oblate en biaxiale nematische fasen, ze gaven de voorkeur aan het vervormen in rechte staven en het vormen van een prolate nematische fase. Vervolgens bestuderen we in Hoofdstuk 4 starre boemerangs. We vinden een vergelijkbaar fasegedrag als in het geval van stijve boemerangs, maar gebruiken Monte Carlo-integratie voor het bepalen van het uitgesloten volume, waardoor we ook boemerangs met kleine interarmhoeken kunnen

bestuderen. Daarnaast onderzoeken we de stabiliteit van de nematische fasen met betrekking tot smectische verstoringen. We vinden dat deze het dichtheidsregime van de nematische fasen voor gebogen deeltjes aanzienlijk kunnen verkleinen, en dat dit zelfs het geval kan zijn voor boemerangs met hogere aspectverhoudingen.

In Hoofdstuk 5, beschouwen we kubusvormige colloïden met tweede en derde viriaaltheorie. Deze kunnen ook prolate, oblate en biaxiale nematische fasen vormen, afhankelijk van de deeltjesvorm en de dichtheid. Het is voorspeld dat de zogenaamde duale vorm de ideale vorm is voor cuboïden om biaxiale nematische fasen te vormen. We vinden dat, in tegenstelling tot eerdere voorspellingen, er geen directe isotrope biaxiale nematische faseovergang is voor cuboïden met duale vorm, als gevolg van een tussenliggende uniaxiale nematische fase. Binnen de tweede viriaaltheorie is er een perfecte symmetrie tussen oblaten en prolaten in de duale vorm, en dus is de vrije energie van deze twee fasen in dit geval identiek. In de derde viriaaltheorie is deze symmetrie gebroken. In een versimpeld model waarin de deeltjes slechts zes discrete oriëntaties kunnen hebben vinden we dat de tussenliggende uniaxiale fase prolaat is voor cuboïden met duale vorm. Een meer realistisch model, waarin deeltjes een willekeurige oriëntatie kunnen hebben, laat echter zien dat de oblate nematische fase de voorkeur heeft bij de duale vorm, in overeenstemming met recente simulaties.

We bestuderen de sedimentatie van een binair mengsel van dikke en dunne harde staven in Hoofdstuk 6. Hier vinden we dat de zwaartekracht een groot aantal fase-sequenties kan veroorzaken als een functie van de hoogte in een "reageerbuis." We brengen alle mogelijke stapelsequenties voor drie diameterverhoudingen in kaart en vinden enkele verrassende sequenties zoals een isotrope fase ingeklemd tussen twee nematische fasen. In het meest complexe fasendiagram dat hier wordt beschouwd, vinden we zestien verschillende stapelvolgorden, waaronder verscheidene met vijf gesedimenteerde lagen. We berekenen ook dichtheid- en compositieprofielen als functie van de hoogte.

Ten slotte bestuderen we de percolatiedrempel van verschillende harde deeltjes met behulp van de "verbindingspercolatietheorie" binnen de tweede viriale benadering. In Hoofdstuk 7, beschouwen we staafvormige deeltjes met knik- of buigvervormingen. Met dit model kunnen we systemen van koolstofnanobuisjes met defecten beschrijven, dit soort deeltjes worden normaalgesproken beschreven als geïdealiseerde staafjes. We vinden dat, hoewel de percolatiedrempel sterk afhangt van de aspectverhouding van de staven, kleine of matige vormvervormingen zeer weinig effect hebben. In Hoofdstuk 8, bekijken we andere vormen van onregelmatigheden in vorm, namelijk veel-

hoekige staven en platen met een verschillend aantal zijden. Hier berekenen we analytisch de percolatiedrempel in termen van drie verschillende maten van een enkel deeltje. We vinden dat het veranderen van de dwarsdoorsnede van een staaf of plaat van een cirkel naar een polygoon de percolatiedrempel verlaagt, in sommige gevallen zelfs aanzienlijk. Dit is een consequentie van de toename van de verhouding tussen oppervlakte en volume voor deeltjes met een dwarsdoorsnede met minder zijden.

Acknowledgments

First of all I would like to thank René for giving me the opportunity to do this PhD. Your positive and enthusiastic attitude always made it a great pleasure to work with you. Your physical intuition and knowledge of liquid crystals and physics in general made our discussions very helpful. I learned a lot working with you, thanks for everything!

I would like to thank all the members of the T+S group for the many interesting meetings and the pleasant atmosphere. In particular, I'm grateful that I got the opportunity to collaborate with Marjolein and her group. Thanks, Marjolein for the interesting conversations and for your many helpful suggestions. Also, several of the projects in this thesis would not have been possible without Simone's help, code, and collaboration. Thanks Simone! Massi, thanks for the many discussions about boomerangs. In addition, it was a pleasure to get to work with Paul on the percolation projects. Paul, thanks for suggesting these projects and for your guidance and collaboration on them.

To my office mates Drian and Jiansen and to my nearest neighbor Andy– thanks for all the nice coffee breaks! Jiansen, thanks for all the nice conversations about neural networks and programming. Thanks also to all the people who participated in our informal machine learning club meetings, which were always a highlight of my week. Thanks to Wanda and Olga for everything they do behind the scenes as well as for the great Thursday afternoon snacks.

Tatjana, Luka, Simonas, and Ieva (plus associated cats), thanks for all the fun D&D and game nights! Thanks also to many other friends who made the last four years a lot of fun.

To the Veldhoen's– thanks for all the help in the garden, for the nice hikes, and for the yearly Thanksgiving dinners together. You guys always make me feel like a part of the family!

To the Drwenski's– thanks for all the fun vacations and for being willing to travel ~ 5000 miles to come visit me. Mom and Dad– thanks for teaching me to always keep learning and for always being up for anything.

Misha, thanks for the (uncountably) many things you've done for me in the last years, including but not limited to: watching Star Trek with me,

planning road trips, making me breakfast, fixing my bike, playing computer games with me, proofreading my papers, mijn Nederlands corrigeren, en in alle opzichten het (Misha: de) beste partner in alles zijn.

Finally, I would like to thank my cat Spinor, who always believed in me.

List of publications

This thesis is partially based on the following publications:

Chapter 2:

T. Drwenski, S. Dussi, M. Hermes, M. Dijkstra, and R. van Roij, *Phase diagrams of charged colloidal rods: can a uniaxial charge distribution break chiral symmetry?*, J. Chem. Phys., **144**, 094901 (2016)

Chapter 3:

T. Drwenski and R. van Roij, *The effect of flexibility and bend angle on the phase diagram of hard colloidal boomerangs*, Mol. Phys., accepted, (2018)

Chapter 5:

S. Dussi*, N. Tasios*, T. Drwenski,* R. van Roij, and M. Dijkstra, *Hard competition: stabilizing the elusive biaxial nematic phase in suspensions of colloidal particles with extreme lengths*, Phys. Rev. Lett., **120**, 177801 (2018) [* These authors contributed equally.]

Chapter 6:

T. Drwenski, P. Hooijer, and R. van Roij, *Sedimentation stacking diagrams of binary mixtures of thick and thin hard rods*, Soft Matter, **12**, 5684 (2016)

Chapter 7:

T. Drwenski, S. Dussi, M. Dijkstra, R. van Roij, and P. van der Schoot, *Connectedness percolation of hard deformed rods*, J. Chem. Phys., **147**, 224904 (2017)

Chapter 8:

T. Drwenski, R. van Roij, and P. van der Schoot, *Connectedness percolation of hard convex polygonal rods and platelets*, J. Chem. Phys., **149**, 054902 (2018)

Other publications by the author:

- T. Drwenski, U. Gürsoy , and I. Iatrakis, *Thermodynamics and CP-odd transport in Holographic QCD with Finite Magnetic Field*, J. High Energy Phys., **2016**, 49 (2016)
- S.Y. Liu, S. Liu, D. Li, T. Drwenski, W. Xue, and H. Dang, and S. Wang, *Oxidation mechanism of the intermetallic compound Ti_3Al from ab initio thermodynamics*, Phys. Chem. Chem. Phys., **14**, 11160 (2012)

Curriculum vitae

Tara Drwenski was born on March 6, 1990 in Rockwall, Texas. She obtained her bachelor's degree in Physics and Mathematics from the University of Tulsa in 2012. In 2014, she completed her master's degree in Theoretical Physics at Utrecht University. Her master thesis research project, supervised by Dr. Umut Gürsoy, was on holographic QCD. In 2014, she began her PhD research under the supervision of Prof. Dr. René van Roij. The results of this research are described in this thesis.